

**FOURIER TRANSFORM FLUORESCENCE RECOVERY  
AFTER PHOTOBLEACHING WITH PATTERNED  
ILLUMINATION**

by

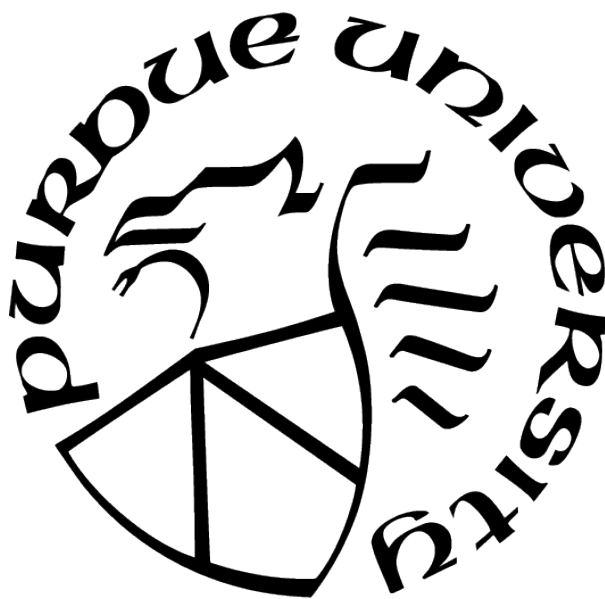
**Andreas Crispin Geiger**

**A Dissertation**

*Submitted to the Faculty of Purdue University*

*In Partial Fulfillment of the Requirements for the degree of*

**Doctor of Philosophy**



Department of Chemistry

West Lafayette, Indiana

May 2021

**THE PURDUE UNIVERSITY GRADUATE SCHOOL  
STATEMENT OF COMMITTEE APPROVAL**

**Dr. Garth J. Simpson, Chair**

Department of Chemistry

**Dr. Chi Zhang**

Department of Chemistry

**Dr. Mary J. Wirth**

Department of Chemistry

**Dr. Pavlos P. Vlachos**

School of Mechanical Engineering

**Approved by:**

Dr. Christine A. Hrycyna



To my beautiful wife and cherished companion, Yta

## ACKNOWLEDGMENTS

This document would not be possible were it not for the support of countless individuals. I have listed here only a few of those who have contributed to my doctoral work. Should I take the time to list everyone, I am sure it would be even longer than this thesis.

God, my creator and sustainer, for the physical and mental faculties he gave me, without which I would not be able to live and move much less undertake the advanced studies required to complete this dissertation. May my endeavor to search out a small corner of the created order bring glory to Him who made heaven and earth, the sea, and all that is in them.

My wife, Ytai, who has worked tirelessly to care for our boys, cook for our family, and manage our home on a very tight budget. She has a job that is more difficult and of greater consequence than mine. However, her job receives much less recognition than is due. Beyond her excellent work in the home, I thank Ytai for her companionship and encouragement that have often refreshed me when I needed it most.

My parents, Phil and Su, who devoted so much of their lives to raising me and my siblings. My mother was particularly invested in my education. She checked my homework at the kitchen table every night when I was young and equipped me to become an independent learner. My mother has always had a strong personal interest in science and I am sure that she will be one of the few to read my thesis cover to cover.

My advisor, Garth, an incredibly intelligent scholar and yet a humble leader. I have learned so much over the course of my Ph.D. just by watching the way Garth does his job. After spending five years working with him I have found myself talking, writing, and thinking the same way about science as Garth! I am especially thankful for the incredible amount of trust that Garth has in his students. He has given my coworkers and I the opportunity to assist in authoring grants, organizing a short-course with attendees from around the world, and authoring review articles and book chapters. I do not know many other research groups with opportunities like these and for that I am thankful. Furthermore, Garth has a management style that facilitates a cooperative rather than a competitive work environment. As a consequence, much of what I learned in graduate school was from other students in our

research group. It’s no surprise that so many group members mention that the Simpson Lab feels like a family.

My coworkers in the Simpson Lab for Nonlinear Optics: Azhad Chowdhury ’16, Nicole Scarborough ’17, Janny Dinh ’17, Max Deng ’18, Shijie Zhang ’18, Jerald Martin ’18, Changqin Ding ’19, Zhengtian Song ’19, Sreya Sarkar ’19, James Ulcickas ’20, Chen Li ’20, Casey Smith ’20, Scott Griffin ’20, Hilary Florian ’20, Youlin Liu, Alex Sherman, Ziyi Cao, Minghe Li, Jiayue Rong, Nita Takanti, Randy Akrofi, Dustin Harmon, Aleksandr Razumtcev, and Xiating Li. I am so thankful that I had the opportunity to work with such a talented and kind group. The Simpson Lab is known not only for great science, but more than that, for great people. In particular, I am thankful for Casey Smith, a trustworthy team member and a friend who I can count on.

Coauthors who have contributed to the work presented in this thesis, including Casey J. Smith, Nita Takanti, Dustin M. Harmon, Ziyi Cao, Zhengtian Song, James R. W. Ulcickas, Randy Akrofi, Alex M. Sherman, Mark S. Carlsen, Lynne S. Taylor, Jeremy Hinds, Paul A. Stroud, and Garth J. Simpson

Finally, those who have provided financial support through fellowships and assistantships during my time at Purdue, including the Purdue Graduate School, the Purdue Department of Chemistry, Eli Lilly and Company, and the taxpayers of the United States of America through the National Science Foundation.

Portions of this thesis have been previously published by Cell Press, the American Chemical Society, and the Royal Society of Chemistry. Full citations of these publications can be found in the **Selected Publications** appendix.

# TABLE OF CONTENTS

LIST OF TABLES . . . . .	9
LIST OF FIGURES . . . . .	10
LIST OF SYMBOLS . . . . .	14
ABBREVIATIONS . . . . .	15
GLOSSARY . . . . .	17
ABSTRACT . . . . .	18
1 BACKGROUND . . . . .	19
1.1 Optimization of biopharmaceuticals motivates improved diffusion measurements	19
1.2 Common methods for diffusion measurements . . . . .	20
1.3 Fluorescence recovery after photobleaching (FRAP) . . . . .	22
1.4 Limitations of conventional FRAP & review of previous FRAP innovations .	23
1.5 Fourier transform fluorescence recovery after photobleaching (FT-FRAP) . .	26
1.6 Comparison of FT-FRAP to previous work . . . . .	28
2 THEORY . . . . .	31
2.1 Fourier analysis of the diffusion equation . . . . .	31
2.2 Conventional FRAP . . . . .	32
2.3 Comb-photobleach FT-FRAP . . . . .	33
2.4 Dot-array-photobleach FT-FRAP . . . . .	35
2.5 Anomalous diffusion . . . . .	35
2.6 Signal power . . . . .	37
2.7 Phasor analysis of flow in FT-FRAP . . . . .	40
2.8 Patterned versus point photobleaching . . . . .	42
2.9 Diffusion imaging . . . . .	42
3 MATERIALS AND METHODS . . . . .	46

3.1	Two-photon excited fluorescence (TPEF) microscopy . . . . .	46
3.2	Comb-photobleach FT-FRAP . . . . .	47
3.3	Dot matrix photobleach FT-FRAP . . . . .	48
3.4	Sample preparation . . . . .	48
3.5	Data analysis . . . . .	49
4	NORMAL DIFFUSION CHARACTERIZATION . . . . .	51
4.1	Polymer diffusion analysis by comb-photobleach FT-FRAP . . . . .	51
4.2	Protein diffusion analysis by comb photobleach FT-FRAP . . . . .	51
4.3	Antibody diffusion analysis by dot-array-photobleach FT-FRAP . . . . .	53
5	FLOW CHARACTERIZATION . . . . .	56
6	ANOMALOUS DIFFUSION CHARACTERIZATION . . . . .	58
7	DIFFUSION IMAGING . . . . .	61
8	CONCLUSION . . . . .	64
9	STOCHASTIC DSC BY NONLINEAR OPTICAL MICROSCOPY . . . . .	65
9.1	Abstract . . . . .	65
9.2	Background . . . . .	65
9.3	Methods . . . . .	68
9.3.1	SHG microscopy . . . . .	68
9.3.2	DSC measurements . . . . .	69
9.3.3	Data analysis . . . . .	69
9.3.4	Sample preparation . . . . .	70
9.4	Results and Discussion . . . . .	70
9.4.1	SDSC of urea crystals . . . . .	70
9.4.2	IRF determination with SDSC . . . . .	74
9.4.3	SDSC of trehalose dihydrate crystals . . . . .	75
9.5	Conclusions . . . . .	82

REFERENCES . . . . .	83
DATA ANALYSIS SCRIPTS . . . . .	98
VITA . . . . .	121
SELECTED PUBLICATIONS . . . . .	122

## LIST OF TABLES

1.1	Figures of merit for FRAP methods . . . . .	27
-----	---	----

# LIST OF FIGURES

1.1	Schematic depicting A) conventional point-bleach FRAP illumination, B) patterned illumination with comb excitation, and C) spatial FT of the patterned illumination in (B). Conventional point-bleach FRAP produces a sharp point in real space. FT-FRAP with patterned illumination produces sharp puncta in the spatial Fourier domain. . . . .	26
1.2	Schematic depicting patterned illumination with A) a dot array pattern, which Fourier transforms to B) a two-dimensional set of equally spaced puncta. . . . .	28
1.3	Graphical depiction of diffusion imaging by FT-FRAP. Two-dimensional Fourier transformation of fluorescence recovery images after comb photobleaching produces a series of peaks in the spatial frequency domain. Excising one peak and shifting it to the center of the spatial frequency domain enables diffusion imaging through inverse Fourier transformation and least-squares fitting at each pixel or superpixel. . . . .	29
2.1	Decay of FRAP signal over time for point-bleach FRAP and FT-FRAP with 32-line patterned illumination. Signal rapidly degrades for point-bleach relative to comb-illumination even when normalized for total bleach power. In principle, the signal of FT-FRAP increases as the distance between photobleached lines increases. . . . .	39
3.1	Instrument schematic of a nonlinear-optical beam-scanning microscope used for multi-photon FT-FRAP. A HWP on a flip mount was used to modulate from low power ( 50 mW) to high power ( 500 mW) for the photobleach. Beam scanning was performed with galvanometer (slow axis) and resonant (fast axis) mirrors. DCM = dichroic mirror, HWP = half-wave plate, PMT = photomultiplier tube, SPF = short-pass filter, TPEF = two-photon excited fluorescence. . . . .	47
3.2	Instrument schematic of a commercial FRAP microscope that was modified for dot array photobleach FT-FRAP. Modifications are indicated by red dashed boxes. A more powerful laser replaced the original photobleach laser and a DOE was added to the excitation light path to produce a dot array photobleach pattern. DCM = dichroic mirror, DOE = diffractive optical element, CCD = charge-coupled device camera, LED = broadband green light emitting diode. . . . .	49
4.1	Multiphoton excited FT-FRAP with comb photobleach of FITC-polydextran (2 MDa) dissolved in 50/50 glycerol/water. A) Image of the solution immediately after a 32-line comb bleach. B) 2D-FT of (A) with the circled peaks corresponding to the first and second spatial frequency harmonics of the 32-line comb bleach. C) Fluorescence recovery of the first and second harmonic peaks with best-fit curves recovering a diffusion coefficient, $D = 3.70 \pm 0.02 \mu\text{m}^2/\text{s}$ . The reported uncertainty is the standard deviation of the fit. . . . .	52



4.2	FT-FRAP with comb bleach of FITC-BSA dissolved in a 2:1 solution of glycerol/water. A) Image of the solution immediately subsequent to a 16-line comb bleach. B) 2D-FT of (A). C) Fluorescence recovery measured at the 1st harmonic of the 2D-FT. D) Fluorescence recovery measured at the 2 <sup>nd</sup> harmonic of the 2D-FT. . . . .	54
4.3	FT-FRAP with dot array bleach of TMR-IgG dissolved in PBS. A) Image of the solution immediately after dot array bleach. B) 2D-FT of (A). Blue and red circles indicate peaks that are equidistant from the origin C) Fluorescence recovery of pooled peaks with best-fit curves. The best-fit value for the diffusion coefficient was $1.92 \pm 0.03 \mu\text{m}^2/\text{s}$ . The reported uncertainty is the standard deviation of the fit. . . . .	55
5.1	Bulk flow measured by FT-FRAP of FITC-polydextran (2 MDa) in 50/50 glycerol/water. A) Real and imaginary amplitudes of the 2D-FT fundamental and 2 <sup>nd</sup> harmonic peaks upon sample translation during diffusion. B) Phase calculated from real and imaginary amplitudes of 2D-FT peaks. The non-translated sample has minimal bulk flow. The velocities calculated from the fundamental and 2 <sup>nd</sup> harmonic peaks of the translated sample are within one standard deviation of each other and close to the translation rate of the sample stage ( $4.0 \pm 0.4 \mu\text{m}/\text{s}$ ) after correcting for bulk flow from convection. The reported uncertainties are the standard deviation of the fit. . . . .	57
6.1	Harmonic analysis of anomalous diffusion with FITC-polydextran (2 MDa) in 22 mg/mL hyaluronic acid. Fluorescence recovery of the first, second, and third harmonics are fit to a modified Mittag-Leffler function to recover the anomalous diffusion coefficient, $D = 1.124 \pm 0.008 \mu\text{m}^\mu/\text{s}^{2\alpha/\mu}$ , the subdiffusion parameter, $\alpha = 0.571 \pm 0.003$ , and the Lévy flight parameter, $\mu = 1.173 \pm 0.006$ . The recovered parameters reveal subdiffusive and Lévy flight behavior in the sample. The reported uncertainties are the standard deviations in the fit. . . . .	59
7.1	Diffusion imaging by FT-FRAP of two droplets containing FITC-dextran (2 MDa) and varying concentration of HA. A) Fluorescence image of the droplets after photobleaching. B) Segmented image defining the boundaries of regions I (18 mg/mL HA) and II (9 mg/mL HA). C) Decay curves of the first, second, and third spatial frequency harmonics in region I. D) Decay curves of the first, second, and third spatial frequency harmonics in region II. Regions I and II exhibit significantly different diffusion coefficients $D$ and anomalous diffusion parameters $\alpha$ and $\mu$ . . . . .	61

7.2	Diffusion imaging by FT-FRAP of FITC-dextran (2 MDa) diffusing in a sphere of methacrylated HA (MeHA) surrounded by collagen in PBS. A) Fluorescence image of the MeHA sphere before photobleaching. B) Segmented image defining the boundaries of regions I (MeHA sphere) and II (collagen). C) Decay curves of the first and second spatial frequency harmonics in region I, exhibiting anomalous diffusion. D) Decay curves of the first spatial frequency harmonics in region II, exhibiting normal diffusion. Regions I and II exhibit significantly different diffusion behavior. . . . .	63
9.1	Schematic of the integrated SHG-DSC microscope. A pulsed laser beam (800 nm, 80 MHz) was scanned with a galvo-resonant scan pair, which was $4f$ coupled to the back of an objective and focused onto a DSC sample pan. The SHG signal was collected in the epi direction, isolated with a dichroic mirror and detected with a photomultiplier tube. . . . .	68
9.2	A) SDSC analysis of urea by combined SHG microscopy and DSC. The solid black line is the DSC trace of the melting of urea with endothermic direction being down (left-axis). The vertical colored lines show the temperatures in which the normalized SHG intensity of individual urea particles (acquired concurrently with DSC measurements) drops below a value of 0.1. DSC and SHG measurements both indicate a structural transformation in the same temperature range. The inset shows a zoom-in of the temperature range 135.5–136.5 °C where the color lines correspond to the normalized SHG intensity of individual urea particles. B) SHG microscope images of urea crystals during SDSC analysis. SHG microscopy reveals the stochastic nature of the melting transition and enables analysis on a per-particle basis. . . . .	71
9.3	SDSC analysis of urea by combined SHG microscopy and DSC. The solid black line is the DSC trace of the melting of urea with endothermic direction being down (left-axis). The thin colored lines show the normalized SHG intensity of individual urea particles (right-axis), acquired concurrently with DSC measurements. DSC and SHG measurements both indicate a structural transformation in the same temperature range. . . . .	72
9.4	Distribution of urea crystal volumes. The estimated volume of the crystals was calculated from the crystal cross-sectional area (assuming rod-like shape). A total mass of 0.39 $\mu\text{g}$ was calculated from the sum of these volumes multiplied by the density of urea (1.32 g/cm <sup>3</sup> ). The mass combined with the observed nucleation rate of 6.13 nuclei/s yields the nucleation rate of $1.6 \pm 0.2 \times 10^4$ nuclei per second per milligram. . . . .	73

9.5	Comparison of the experimental DSC trace and the DSC trace generated from melting events. The best-fit double-exponential IRF (yellow) is convolved with impulsive melting events (blue) of single-particles observed in SHG images to generate the purple trace, which is in good agreement with the experimental DSC data (red). The time constant and offset of double-exponential IRF were optimized to minimize difference between experimental and generated DSC traces. Best-fit values of $1.161 \pm 0.019$ s, $0.435 \pm 0.013$ s, and $3.088 \pm 0.013$ s were computed for the double-exponential time constants and the offset respectively.	74
9.6	SDSC analysis of trehalose by SHG microscopy. The colored lines show the percentage of pixels in a trehalose particle above an SHG intensity threshold overlaid with the black line of the DSC trace with the endothermic direction being down. SDSC images were summed for the temperature range of 140–220 °C and the logarithm of the summed image was cropped to the measured region of each particle (each cropped image points to the representative SHG trace).	76
9.7	IRF analysis of trehalose dihydrate. The final DSC peak in the trehalose dihydrate experiment was analyzed using the IRF recovered from the urea experiment (see Fig. 9.5). The “cold phase transformation” events and the melting events of the four particles were convolved with the best-fit, double-exponential IRF determined from analysis of SDSC data for urea. The results of the convolution are shown as colored curves. Neither the cold phase transformation events nor the melting events produced curves that matched well with the DSC peak. This perhaps indicates that the four particles observed using SHG microscopy are not representative of the full population of particles in the sample. A more complete set of phase transformation events would possibly produce a curve that would better match the DSC peak.	81

## LIST OF SYMBOLS

$A$	amplitude
$C$	concentration
$D$	diffusion coefficient
$f$	frequency
$h$	horizontal spatial frequency
$k$	vertical spatial frequency
$K_d$	equilibrium dissociation constant
$n$	harmonic
$P$	power
$t$	time
$\alpha$	subdiffusion parameter
$\Delta$	phase shift
$\mu$	Lévy-flight parameter
$\bar{\nu}$	spatial frequency
$\rho$	position
$\sigma$	standard deviation
$\tau$	time constant

## ABBREVIATIONS

AOM	Acousto-optical modulator
AOTF	Acousto-optical tunable filter
AUC	Analytical ultracentrifugation
BSA	Bovine serum albumin
CCD	Charge-coupled device
CW	Continuous wave
DCM	Dichroic mirror
DLS	Dynamic light scattering
DOE	Diffraction optical element
DSC	Differential scanning calorimetry
ECM	Extracellular matrix
FITC	Fluorescein isothiocyanate
FOV	Field of view
FT	Fourier transform
FT-FRAP	Fourier transform fluorescence recovery after photobleaching
FRAP	Fluorescence recovery after photobleaching
HA	Hyaluronic acid
HWP	Half wave plate
IFT	Inverse Fourier transform
IRF	Impulse response function
IgG	Immunoglobulin G
LED	Light emitting diode
mAb	Monoclonal antibody
MeHA	Methacrylated hyaluronic acid
MSD	Mean squared displacement
MST	Microscale thermophoresis
PAM	Programmable array microscope
PBS	Phosphate buffered saline

PMT	Photomultiplier tube
PSF	Point spread function
SDSC	Stochastic differential scanning calorimetry
SC	Subcutaneous
SFA	Spatial Fourier analysis
SHG	Second harmonic generation
SNR	Signal-to-noise ratio
SPF	Short pass filter
$T_{am}$	amorphous trehalose
$T_h$	trehalose dihydrate
$T_\alpha$	unstable anhydrous trehalose
$T_\beta$	crystalline anhydrous trehalose
$T_\gamma$	partially amorphous trehalose
TASC	Thermal analysis by structural characterization
TGA	Thermal gravimetric analysis
TMR	Trimethyl rhodamine
TPEF	Two photon excited fluorescence

## GLOSSARY

anomalous	inconsistent with or deviating from what is usual, normal, or expected
diffusion	the process whereby particles of liquids, gases, or solids intermingle as the result of their spontaneous movement caused by thermal agitation and in dissolved substances move from a region of higher to one of lower concentration
DSC	a thermoanalytical technique in which the difference in the amount of heat required to increase the temperature of a sample and a reference is measured as a function of temperature
fluorescence	luminescence that is caused by the absorption of radiation at one wavelength followed by nearly immediate reradiation usually at a different wavelength and that ceases almost at once when the incident radiation stops
FRAP	a microscopy-based method for measuring molecular diffusion by focusing a laser beam to a region of a sample with a fluorescent probe to induce photobleaching, and observing the fluorescence intensity of the sample after photobleaching as a function of time
FT	a mathematical transform that decomposes a function into its constituent frequencies, such as the expression of a musical chord in terms of the volumes and frequencies of its constituent notes
photobleach	to lose color or whiten by the action of light; for example, the use of a laser to bleach a fluorescent dye covalently linked to a macromolecule
segmentation	the process of partitioning a digital image into multiple segments (sets of pixels) with the goal of simplifying and/or changing the image into something that is more meaningful and easier to analyze
SHG	a nonlinear optical process in which two photons with the same frequency interact with a nonlinear material, and generate a new photon with twice the energy of the initial photons and conserved coherence of the excitation

## ABSTRACT

Fourier transform fluorescence recovery after photobleaching (FT-FRAP) with patterned illumination is demonstrated for quantitatively evaluating normal and anomalous diffusion. Diffusion characterization is routinely performed to assess mobility in cell biology, pharmacology, and food science. Conventional FRAP is noninvasive, has low sample volume requirements, and can rapidly measure diffusion over distances of a few micrometers. However, conventional point-bleach measurements are complicated by signal-to-noise limitations, the need for precise knowledge of the photobleach beam profile, potential for bias due to sample heterogeneity, and poor compatibility with multi-photon excitation due to local heating. In FT-FRAP with patterned illumination, the time-dependent fluorescence recovery signal is concentrated to puncta in the spatial Fourier domain through patterned photobleaching, with substantial improvements in signal-to-noise, mathematical simplicity, representative sampling, and multiphoton compatibility. A custom nonlinear-optical beam-scanning microscope enabled patterned illumination for photobleaching through two-photon excitation. Measurements in the spatial Fourier domain removed dependence on the photobleach profile, suppressing bias from imprecise knowledge of the point spread function and enabled flow analysis through the spatial phase shift. Simultaneous measurement of diffusion at multiple length scales was enabled through analysis of multiple spatial harmonics of the photobleaching pattern. Anomalous diffusion was characterized by FT-FRAP through a nonlinear fit to multiple spatial harmonics of the fluorescence recovery.

Furthermore, FT-FRAP with patterned illumination enabled simultaneous diffusion measurements at every position throughout the field of view for normal and anomalous diffusion. Inverse Fourier transformation of peaks shifted to the origin in the spatial frequency domain produced fluorescence recovery maps in real space based on the spatial-frequency peak shape. Diffusion contrast across the field of view was determined through image segmentation and fitting the integrated fluorescence recoveries to a diffusion model.



## 1. BACKGROUND

Therapeutic macromolecules, including monoclonal antibody (mAb) drug conjugates, have enabled treatments of conditions ranging from asthma[1] to rheumatoid arthritis[2], now representing approximately half the total global market for new chemical entities.[3] Subcutaneous (SC) delivery of therapeutic macromolecules greatly increases patient compliance and access by minimizing the skill level required for administration.[4] However, SC injection, when compared to the established intravenous route, has many issues regarding incomplete bioavailability. SC tissue and the lymphatic system act as barriers, meaning that SC bioavailability can be negatively impacted by transport within the SC space. Even in a fully optimized formulation, SC bioavailability of mAbs is typically 52-80%, meaning that as much as half of the delivered dose in an SC injection routinely never reaches the bloodstream for systemic availability.[5] Following SC injection, mAb drug conjugates generally enter into the bloodstream through the lymphatic system, as the lymphatic system provides a direct route to the lymph nodes and limits exposure of the antibody to antigens in blood and normal tissues.[6] Losses limiting the dose delivered to the bloodstream ultimately arise from enzymatic proteolysis in the SC space and/or within the lymphatic system.[5] For the non-denatured mAbs delivered subcutaneously, high protein mobility to the lymphatic system can reduce the timescales over which mAbs are susceptible to enzymatic degradation within the SC space.[5]

### 1.1 Optimization of biopharmaceuticals motivates improved diffusion measurements

Diffusion measurements in well-characterized matrices highly representative of those anticipated within SC environments may provide early-stage *in vitro* assessments of anticipated *in vivo* bioavailability for SC injection of potential therapeutic mAb candidates. This goal is challenging to realize in practice. The SC environment is chemically and structurally diverse, and a host of interactions may happen as the biopharmaceutical minutes to hours after injection.[7] One problem includes regulating temperature of the injection site as some sites closer to the body’s core have different temperatures than sites in the extremities. In addition, up-

take of the biopharmaceuticals is dependent on the biopolymers within the extracellular matrix (ECM); hyaluronic acid, collagen, elastin, and adipocytes may exhibit non-specific and specific interactions with protein. Another potential issue is the impact of the pH transition from the biopharmaceutical formulation to the SC injection site on the bioavailability, as changes in pH can alter the non-uniform surface charge of the protein leading to various complexities.[8] Other possible induced stressful events include transition through the isoelectric point and slower diffusion of the biopharmaceutical protein through SC injection site due to interactions with the ECM.[7] As the SC bioavailability is dependent on the ability of the biopharmaceutical to be absorbed, challenges arise as uptake into systemic circulation are dictated on physico-chemical properties of the molecules – the biophysical status of the SC injected protein or peptide and interactions with the ECM are not easily monitored.[7] Heterogeneity and complexity greatly complicate *in vitro* assay development for two reasons: i) no single set of conditions in an assay is likely to adequately capture the inherent diversity associated with the suite of local *in vivo* environments encountered by therapeutic proteins within the SC space that dictate bioavailability, and ii) increasing the inherent complexity within such a multi-component multi-phase mixture often coincides with a decrease in experimental reproducibility. Source-specific and/or lot-to-lot differences in additives used in multi-component *in vitro* assays scale additively to degrade reproducibility. Decreases in experimental reproducibility compromise the information accessible about the system required to make a meaningful assessment. From a measurement-science standpoint, it is therefore significantly more advantageous to assess complexity through combining many highly reproducible measurements across a panel of diverse compositions. Such measurements can serve two roles: i) to quantify variability within the matrices used to assess therapeutic protein mobility, and ii) to inform on new protein mobility for well-characterized matrices.

## 1.2 Common methods for diffusion measurements

Several strategies have been developed for precise diffusion measurements of proteins that are compatible with mAb analyses in *in vitro* assays, with many of them being label-free. The elucidation of the diffusion coefficient is often done through methods that characterize

molecular interactions, which can be quantified by the equilibrium dissociation coefficient,  $K_d$ .<sup>[9]</sup> One method of measuring diffusion is analytical ultracentrifugation (AUC). In AUC, each protein of unique molecular mass and shape forms a boundary during ultracentrifugation and sediments at a characteristic speed.<sup>[10], [11]</sup>  $K_d$  can be determined through analysis of the velocity of the boundary using a genetic algorithm.<sup>[10], [12]</sup> However, AUC can be time and cost prohibitive due to low throughput, computationally expensive genetic algorithms, and the careful attention required in experimental design and surface treatment.<sup>[9]–[11], [13]</sup> Other established benchtop methods have similar disadvantages - isothermal titration calorimetry and nuclear magnetic resonance have significant time and sample demands, while surface plasmon resonance requires substantial experimental design and surface treatment considerations.<sup>[9]</sup>

Another method, dynamic light scattering (DLS) has been used as a characterization tool for protein diffusion, and as a complementary method to both high pressure liquid chromatography and AUC.<sup>[14]</sup> DLS is based on the concept that light passing through a solution containing molecules will scatter, and the fluctuations of the scattering intensity due to the Brownian motion of molecules in solution allow for the determination of diffusion properties.<sup>[5], [14], [15]</sup> DLS is an ideal method for calculating the individual contributions of monomers and dimers to the light scattering.<sup>[14]</sup> DLS, however, is sensitive to the presence of large aggregates, and the signal from a small number sub-visible particles can saturate the scattering signal needed to measure diffusion.<sup>[15], [16]</sup> In addition, the resolution between peaks in DLS can be quite low, which at times makes it difficult to distinguish the monomer peak from dimer peaks in studies with mAbs.<sup>[15]</sup> Although the throughput of this method is efficient, the presence of multiple peaks and wide peak distributions makes it difficult to analyze DLS data.<sup>[15]</sup>

Microscale thermophoresis (MST) is another method for measuring mobility that measures the direct motion of molecules induced by a temperature gradient.<sup>[9]</sup> MST only requires a few microliters of sample solution and is compatible with label-free samples.<sup>[17]</sup> However, thermophoresis can be unpredictably affected by the presence of high protein concentration and MCT experiments usually neglect the potential effects of association and dissociation ki-

netics. Additionally, commercial MST instruments and the corresponding analytical software do not report accurate confidence limits (although there have been corrections reported).[9]

The high signal-to-noise ratio (SNR) demanded to inform predictive modeling provides a strong impetus to consider fluorescently labeled proteins in mobility assessments. Trace fluorescence labeling can increase sensitivity to the tagged proteins and greatly suppress the background, providing a large SNR enhancement. However, these advantages must be weighed against possible perturbations to the protein upon functional group modification by labeling with a fluorophore. Dye induced perturbations can substantially impact electrostatic behaviors, as charge-sites in the protein often serve as labile locations for dye attachment. Even if only a small fraction of the total protein content is labeled, the fluorescence measurements report only on the mobility of the labeled fraction, which may not be representative of the unlabeled protein.

### 1.3 Fluorescence recovery after photobleaching (FRAP)

Fluorescence recovery after photobleaching (FRAP) is a well-established and widely accessible method for probing diffusion of fluorescently-labeled analytes.[18], [19] In FRAP, a region of a fluorescently-labeled sample is permanently photobleached using a short, high-intensity burst of light. After the photobleach, mobile fluorescent molecules diffuse into the region and mobile photobleached molecules diffuse out of the region. This combined mobility results in a time-dependent recovery of fluorescence intensity in the photobleached region. Diffusion information can be obtained by fitting the fluorescence recovery to a mathematical model.

The first FRAP experiment was performed by Peters et. al. in 1974 to measure the mobility of membrane proteins in red blood cell ghosts.[20] More recently, FRAP has been used to probe epidermal growth factor receptor clustering in Chinese hamster ovary cell membranes,[21] intercellular communication via septal junctions in multicellular cyanobacteria,[22] and the dynamics of intermediate filament-like protein in the hyphae of *Streptomyces venezuelae*. [23] FRAP has also been used to study protein aggregation in the context of liquid-liquid phase separation,[24] to characterize the effect of structure on solute diffusivity

in microporous tissue engineering scaffolds,[25] to compare the mobility of 45 proteins involved in synaptic transmission, and to measure diffusion anisotropy in porcine ligaments.[26] Additionally, FRAP has been applied broadly in the pharmaceutical community to understand molecular transport in hydrogels[27]–[30] and in extracellular matrices[31], [32] in an effort to improve drug delivery outcomes. Recent efforts have also been made to utilize FRAP as a pre-screening assay for in meso crystallization of membrane proteins in lipid cubic phase.[33]–[36]

#### 1.4 Limitations of conventional FRAP & review of previous FRAP innovations

Despite the advantages of FRAP, quantitative diffusion analysis is typically complicated by the requirement for precise knowledge of the photobleaching profile.[37], [38] To support rapid diffusion measurements, FRAP is generally optimized for fast recovery by using a small photobleach spot. To compensate for low signal from a small photobleach spot, high photobleach depth is used to increase the SNR. However, increasing the photobleach depth runs the risk of complicating reproducibility in the spatial photobleach profile by introducing nonlinearities from optical saturation and perturbations to diffusion from local heating.[39] To address this issue, alternative photobleach patterns have been explored, most notably disc,[40] line,[41] and fringe pattern[42]–[44] illumination. Disc illumination has the advantage of increasing the overall number of molecules photobleached, but largely negates the  $1/f$  noise reductions from highly localized photobleaching and correspondingly fast recoveries. Line illumination is a reasonable compromise, supporting fast recovery in the direction orthogonal to the photobleach line and SNR averaging along the length of the line. With the possible exception of disc and fringe illumination, in which the contiguous photobleach spot is large relative to the optical point-spread function, the point and line photobleach patterns with the greatest reduction in  $1/f$  noise are most prone to artifacts from ambiguities in the photobleach point spread function (PSF).

Alternative photobleaching patterns have also been employed in FRAP to measure diffusion in multiple regions or over a broader region. While FRAP is typically performed by photobleaching one point to ensure a fast fluorescence recovery, measurements of diffu-

sion across broad regions of a sample require alternative photobleaching patterns. Multiple, single point FRAP measurements have been performed in parallel to measure diffusion in 2-3 regions of a sample.[24], [45] This can be achieved with a confocal beam-scanning microscope by programming an acousto-optical modulator (AOM) or acousto-optical tunable filter (AOTF) to rapidly modulate laser power while scanning, producing multiple photobleached regions in the field of view (FOV).[46] However, this strategy only informs on diffusion in a few discrete regions of the sample. Alternative photobleaching patterns have also allowed FRAP measurements of larger areas, but these strategies integrate over the total FRAP signal, rather than inform on differences in local diffusion throughout a FOV.[47]–[51]

Several studies have successfully used FRAP to measure differences in diffusion over broad regions of a sample. Hagen and coworkers developed a FRAP technique that simultaneously performs an arbitrary number of single-point FRAP experiments across a FOV using structured illumination in a programmable array microscope (PAM).[52] The PAM uses a spatial light modulator as a photobleaching mask to produce multiple photobleached spots at the sample plane. The authors used this technique to measure local variation in diffusion for erbB3 (HER3) receptor tyrosine kinase in cells. In another study, Superfine and coworkers leveraged selective plane illumination to photobleach an entire two-dimensional plane of a sample and generate a fluorescence recovery image of NLS-GFP and 53BP1-mCherry in live cells.[53] The authors used a combination of a cylindrical lens and an annulus to produce a Line Bessel Sheet for photobleaching the YZ plane. Horizontal imaging of the fluorescence recovery was achieved using a right-angle reflective prism.[54] A simple closed-form solution to the diffusion equation was not possible in this case due to the complexity of the illumination profile. Instead, the investigators used a numerical diffusion simulation to convert from fluorescence recovery time to diffusion coefficient.

Spatial Fourier analysis (SFA) is one of the more successful strategies used to date for addressing ambiguities in the PSF for point-excitation.[40], [55]–[57] In summary, diffusion in FRAP can be modeled as the convolution of the photobleach PSF with a time-varying Gaussian function. This convolution produces a function describing the real-space fluorescence recovery that is dependent on both time and the photobleach PSF. Moreover, this convolution generally produces a real-space recovery with no simple closed-form analytical

solution, with a few notable exceptions for the photobleach PSF (e.g., Gaussian). However, in the Fourier transform domain, the convolution corresponds to a simple multiplication, disentangling the time-dependent decay from the photobleach profile. The decay curves for each spatial frequency in SFA can be used individually or collectively for recovering the diffusion coefficient. In this manner, the detailed functional form for the initial PSF becomes less critical in the analysis, as the fluorescence recovery is only dependent on time and not on the initial photobleach PSF for a single spatial frequency.[58] For point-excitation, SFA suffers by distributing the signal power from sharp features in the real-space image out over many low-amplitude frequencies in the SFA image, but the intrinsic SNR can be recovered through simultaneous, collective analysis at multiple spatial frequencies. When one or a small number of frequencies are used, this distribution of power can result in a reduction in SNR, the cost of which represents a trade-off for the benefits in reducing ambiguities related to the PSF.

Furthermore, point-bleach FRAP lacks sensitivity for characterizing anomalous diffusion. Diffusion is categorized as anomalous when it deviates from normal Brownian diffusion. Whereas the mean squared displacement (MSD) in normal diffusion evolves with a linear dependence on time, the MSD in anomalous diffusion exhibits a nonlinear dependence on time, resulting in a time-varying/distance-dependent diffusion coefficient.[59], [60] Anomalous diffusion has been observed in a variety of systems, such as the cell and polymeric networks.[61]–[64] Anomalous diffusion in point-bleach FRAP can be identified through a nonlinear fit of the fluorescence recovery to an anomalous diffusion model.[65] However, the relatively subtle differences in the point-bleach recovery curves between normal and anomalous diffusion can complicate identification and quantification of deviations from normal diffusion. Further complications in accurately characterizing anomalous diffusion with point-bleach FRAP arise from the requirement for precise knowledge of the photobleaching PSF. In addition, significant covariance between fitting parameters can result in relatively large uncertainties in the recovered coefficients (e.g., the diffusion coefficient and an anomalous exponent).

Finally, point excitation poses particularly problematic practical challenges from local heating effects in multi-photon excited FRAP measurements.[66] Because of the general inefficiency of multi-photon excitation, a large flux of light is typically introduced, only a small

fraction of which contributes to excitation and fluorescence. Weak but nonzero absorption of the incident light and Stokes Raman transitions leading to local heat deposition both compete with multi-photon excitation. When the excitation beam is fixed at a single location, local temperatures can quickly escalate until the rate of heat dissipation matches the rate of deposition. Depending on the steady-state temperature differential, this transient temperature gradient can potentially bias subsequent diffusion measurements based on isothermal assumptions.

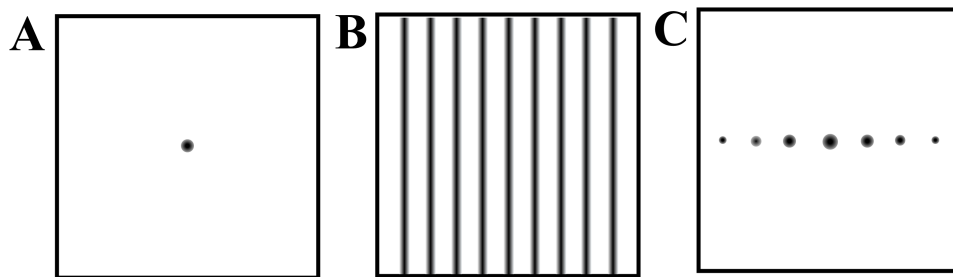


**Figure 1.1.** Schematic depicting A) conventional point-bleach FRAP illumination, B) patterned illumination with comb excitation, and C) spatial FT of the patterned illumination in (B). Conventional point-bleach FRAP produces a sharp point in real space. FT-FRAP with patterned illumination produces sharp puncta in the spatial Fourier domain.

### 1.5 Fourier transform fluorescence recovery after photobleaching (FT-FRAP)

In this work, comb patterns for illumination during photobleaching were demonstrated to support high SNR measurements of normal and anomalous diffusion in Fourier transform analysis of fluorescence recovery with multi-photon excitation. In brief, photobleach patterns were selected to concentrate signal to puncta in the spatial FT domain, rather than a point in the real-space image, as shown in Figure 1.1. Patterned illumination using rapid line-scanning distributed the power from the photobleach over much larger regions in the field



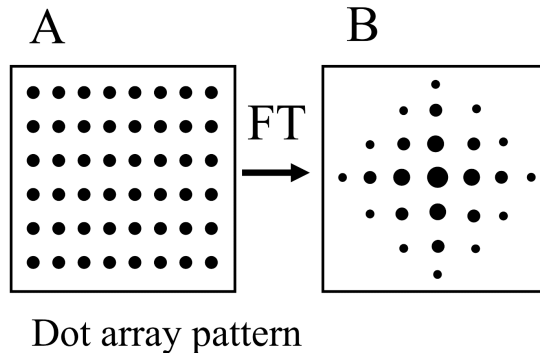
of view, removing many of the potential nonlinearities and biases associated with highly localized excitation while enabling multi-photon excitation with negligible artifacts from local heating. Probing diffusion at multiple length scales by interrogating multiple harmonics in the spatial frequency domain was shown to increase confidence in recovered fitting parameters in analysis of anomalous diffusion. A comparison between FT-FRAP and conventional, point-bleach FRAP is shown in Table 1.1.

**Table 1.1.** Figures of merit for FRAP methods

<b>Conventional FRAP</b>	<b>Fourier Transform FRAP</b>
Knowledge of PSF required	Knowledge of PSF not required
Incompatible with multiphoton excitation	Compatible with multiphoton excitation
Samples one point	Samples the entire field of view
Probes average diffusion over all lengths	Probes diffusion at multiple lengths

We also present FT-FRAP with dot array illumination patterns which were designed to concentrate signal to an array of puncta in the spatial frequency domain through Fourier transformation, as shown in Figure 1.2. Performing the diffusion analysis in the spatial frequency domain following this patterned illumination substantially increased signal, reduced bias from heterogeneity, simplified the mathematical model by removing dependence on the photobleach profile, and has the potential to characterize anisotropic diffusion.

Lastly, we present diffusion imaging using FT-FRAP with patterned illumination. In FT-FRAP, a fluorescent sample is photobleached using patterned illumination to produce a periodic fluorescent pattern. As shown in Figure 1.3, FRAP signal is concentrated to a set of peaks in the spatial frequency domain through Fourier transformation, with each peak representing the spatial frequency harmonics of the photobleach pattern. By excising a peak, translating the peak to the origin of the spatial frequency domain, and performing an inverse Fourier transform (IFT), a stack of fluorescence recovery images is produced. A diffusion image is generated by fitting each pixel (or superpixel) of the fluorescence recovery



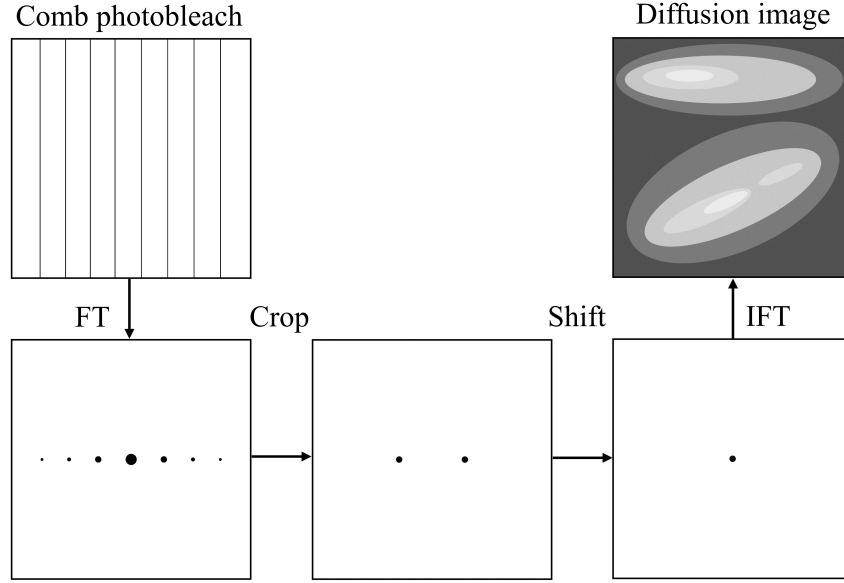
**Figure 1.2.** Schematic depicting patterned illumination with A) a dot array pattern, which Fourier transforms to B) a two-dimensional set of equally spaced puncta.

image stack to a simple exponential decay for normal diffusion or a Mittag-Leffler function for anomalous diffusion.

The theoretical foundation for Fourier-transform fluorescence recovery after photobleaching (FT-FRAP) with patterned illumination is evaluated in proof-of-concept studies of model systems for characterizing normal and anomalous diffusion.

## 1.6 Comparison of FT-FRAP to previous work

The illumination patterns investigated in this work were specifically designed for spatial Fourier transform analysis and as such differ significantly from a host of previous FRAP studies using patterned illumination. Previous work investigated the use of arbitrary photobleach patterns to select objects or regions of interest within the field of view.[38], [67], [68] Alternatively, several investigators have explored measurements with line-excitation.[41], [69] However, none of these previous patterned illumination studies incorporated intentional periodicity within the photobleach patterns that could subsequently integrate into FT-FRAP analysis. Control over the number of lines within the comb provides the advantage of matching the distances over which diffusion is measured, and correspondingly the timeframe for recovery. Under high magnification, the field of view is reduced, which can be compensated by reducing the number of lines within the patterned photobleach. Conversely, measurement



**Figure 1.3.** Graphical depiction of diffusion imaging by FT-FRAP. Two-dimensional Fourier transformation of fluorescence recovery images after comb photobleaching produces a series of peaks in the spatial frequency domain. Excising one peak and shifting it to the center of the spatial frequency domain enables diffusion imaging through inverse Fourier transformation and least-squares fitting at each pixel or superpixel.

time can be reduced to improve throughput by increasing the number of lines in the photobleach pattern to reduce the diffusion distances in the comb. The closest work to the present study is arguably in early studies by Lanni and Ware, in which sinusoidal modulation of a photobleach pattern was performed by passing the excitation beam through a grating.<sup>[70]</sup> The apparatus was designed so that the image of the grating was at the focus of the sample, creating a photobleaching mask at high laser power. The subsequent fluorescence recovery was probed by translating the grating, producing a phase shift in the illumination pattern at the sample, which generated a periodic signal in the integrated fluorescence intensity over time as the grating was shifted. The integrated fluorescence signal was recorded on a single-channel detector and the Fourier components were analyzed to recover the diffusion coefficient. The conceptual foundation for the studies by Lanni and Ware is aligned with the principles undergirding the work presented herein. The difference lies in the tools that were used to realize the FT-FRAP measurement. Laser-scanning microscopy makes FT-FRAP a

faster, higher SNR, measurement than similar techniques with different tools from decades ago.

## 2. THEORY

Prior to discussion of FT-FRAP with patterned illumination, it is useful to review conventional FRAP as a comparator within the FT framework.

### 2.1 Fourier analysis of the diffusion equation

Fick's Law of Diffusion is given by the following general expression.

$$\frac{\partial}{\partial t} C(\boldsymbol{\rho}, t) = \Delta \mathbf{D} \Delta C(\boldsymbol{\rho}, t) \quad (2.1)$$

In which  $C(\boldsymbol{\rho}, t)$  is the concentration of the analyte of interest as a function of position  $\boldsymbol{\rho}$  and time  $t$ , and  $\mathbf{D}$  is the three-dimensional diffusion tensor.

This differential equation is arguably simpler to evaluate by first performing the spatial Fourier transform to generate  $\tilde{C}(\bar{\boldsymbol{\nu}}, t)$ , in which  $\tilde{C}$  is the spatial Fourier transform of  $C$  and  $\bar{\boldsymbol{\nu}}$  is the 3D spatial wavevector. Upon Fourier transformation of the diffusion equation given in Eq. 2.1, each derivative transforms as multiplication by the “diagonal” function  $i2\pi\bar{\boldsymbol{\nu}}$ .

$$\frac{\partial}{\partial t} \tilde{C}(\bar{\boldsymbol{\nu}}, t) = -4\pi^2 \bar{\boldsymbol{\nu}}^T \mathbf{D} \bar{\boldsymbol{\nu}} \tilde{C}(\bar{\boldsymbol{\nu}}, t) \quad (2.2)$$

Evaluation of  $\bar{\boldsymbol{\nu}}^T \mathbf{D} \bar{\boldsymbol{\nu}}$  considering diffusion just within the  $(x, y)$  plane yields the nonzero scalar products  $\bar{\nu}_x^2 D_{xx} + 2\bar{\nu}_x \bar{\nu}_y D_{xy} + \bar{\nu}_y^2 D_{yy}$ . For a choice of  $(x, y)$  coordinates defined along the principal moments of the diffusion tensor  $\mathbf{D}$  (including the case of constant diffusion in all  $(x, y)$  directions),  $D_{xy} = 0$ . In this case, the diffusion equation can be independently evaluated in each of the  $(x, y)$  directions. The expression for the  $x$ -direction is given below, with an analogous expression present for the  $y$ -direction.

$$\frac{\partial}{\partial t} \tilde{C}(\bar{\nu}_x, t) = -4\pi^2 \bar{\nu}_x^2 D_{xx} \tilde{C}(\bar{\nu}_x, t) \quad (2.3)$$

Since only  $\tilde{C}(\bar{\nu}_x, t)$  in Eq. 2.3 depends on time, the expression in Eq. 2.3 is of the form  $f'(t) = kf(t)$ , for which one general solution, subject to the constraint of a decay, is given by an exponential function of the form  $f(t) = f(0)e^{kt}$ , with  $k < 0$ .

$$\tilde{C}(\bar{\nu}_x, t) = \tilde{C}(\bar{\nu}_x, 0) e^{-4\pi^2 \bar{\nu}_x^2 D_{xx} t} \quad (2.4)$$

This solution to the differential equation along the  $x$  direction is a Gaussian function in  $\bar{\nu}_x$ . Multiplication by a Gaussian in the spatial Fourier domain corresponds to convolution with a Gaussian in real space.

$$C(x, t) = C(x, 0) \otimes \frac{1}{\sqrt{2\pi\sigma_t^2}} e^{-\frac{x^2}{2\sigma_t^2}}; \sigma_t^2 = 2D_{xx}t \quad (2.5)$$

The standard deviation of the spatial Gaussian distribution  $\sigma_t$  increases with the square root of time, corresponding to convolution with an ever-broadening Gaussian as diffusion proceeds.

## 2.2 Conventional FRAP

In the limit of a thin sample, diffusion in the  $z$ -direction can be neglected, with diffusion expressed with respect to both  $x$  and  $y$ . Under these conditions in conventional FRAP (depicted in Figure 1.1A), the photobleach pattern for a symmetric Gaussian illumination pattern on the back of an objective is also Gaussian within the field of view.

$$C(x, t, 0) = A \left(2\pi\sigma_b^2\right)^{-1} e^{-\frac{x^2+y^2}{2\sigma_b^2}} \quad (2.6)$$

In isotropic media, diffusion is identical in both the  $x$  and  $y$  coordinates, such that the diffusion tensor can be replaced by a single scalar diffusion coefficient  $D$ . In this limit, the convolution of two 2D Gaussian functions (one from the initial photobleach and one from diffusion) has the convenient property of producing yet another Gaussian function, the width of which evolves in time.

$$C(x, y, t) = A \left(2\pi\sigma_b^2\right)^{-1} e^{-\frac{x^2+y^2}{2\sigma_b^2}} \otimes (4\pi Dt)^{-1} e^{-\frac{x^2+y^2}{4Dt}} \quad (2.7)$$

Evaluation of the convolution results in the following expression for the time-dependence.

$$C(x, y, t) = A \left( 2\pi\sigma_b^2 + 4\pi Dt \right)^{-1} e^{-\frac{x^2+y^2}{2\sigma_b^2+4Dt}} \quad (2.8)$$

If the system is anisotropic, selection of the principal spatial coordinates that diagonalize the diffusion matrix allows the diffusion equation to incorporate differences in diffusivity along different spatial dimensions.

$$C(x, y, t) = A \left( 2\pi\sigma_b^2 \right)^{-1} e^{-\frac{x^2+y^2}{2\sigma_b^2}} \otimes \left[ (4\pi D_{xx}t)^{-\frac{1}{2}} e^{-\frac{x^2}{4D_{xx}t}} (4\pi D_{yy}t)^{-\frac{1}{2}} e^{-\frac{y^2}{4D_{yy}t}} \right] \quad (2.9)$$

$$C(x, y, t) = A \left[ \left( 2\pi\sigma_b^2 + 4\pi D_{xx}t \right) \left( 2\pi\sigma_b^2 + 4\pi D_{yy}t \right) \right]^{-\frac{1}{2}} e^{-\frac{x^2}{2\sigma_b^2+4D_{xx}t}} e^{-\frac{y^2}{2\sigma_b^2+4D_{yy}t}} \quad (2.10)$$

In the more general case of a non-Gaussian function describing the photobleach pattern  $C(x, y, 0)$ , the situation is significantly more complex. In general, no simple analytical forms are expected for the convolution of a Gaussian with non-Gaussian functions, requiring numerical methods for approximations. Unfortunately, non-Gaussian photobleach patterns are commonplace. Even when Gaussian patterns are intended, photobleaching can often approach saturating conditions when the peak photobleach depth approaches unity, resulting in “top-hat” initial photobleach peak shapes. In such cases, the shape of the recovered region can be complicated to integrate analytically into the diffusion analysis for recovery of the diffusion coefficient.<sup>[39]</sup>

### 2.3 Comb-photobleach FT-FRAP

In FT-FRAP, the initial photobleach pattern is selected to produce sharp puncta in the spatial frequency domain, rather than in real-space. One such pattern is a comb, or a periodic series of lines. For mathematical purposes, we will define the comb pattern to proceed along the  $x$ -axis in the laboratory frame with constant illumination along the  $y$ -axis, producing

a series of photobleached stripes (depicted in Figure 1.1B). The initial photobleach pattern  $C(x, 0)$  is constant in the  $y$ -axis and given below, in which  $\delta_{x, \pm n/2\pi\bar{\nu}_x^0}$  is a delta function at the positions  $\pm n\bar{\nu}_x^0$  and  $n \in 0, 1, 2, \dots$ ,  $C_0$  is the initial concentration of the analyte of interest, and  $A$  is the photobleach depth.

$$C(x, 0) = C_0 \left[ 1 - A \sum_{n=0,1,2,\dots} \left( \delta_{x, \pm n/2\pi\bar{\nu}_x^0} \otimes PSF(x) \right) \right] \quad (2.11)$$

By taking the spatial Fourier transform of this equation, the convolution of the photobleach  $PSF(x)$  with the comb pattern  $\delta_{x, \pm n/2\pi\bar{\nu}_x^0}$  is replaced by a multiplication operation, simplifying the analysis. The initial ( $t = 0$ ) spatial Fourier transform of  $C(x, 0)$  along the  $x$ -direction is then given by the following expression, in which  $\Phi_{PSF}(\bar{\nu}_x)$  is the spatial Fourier transform of  $PSF(x)$ .

$$\tilde{C}(\bar{\nu}_x, 0) = C_0 \left[ \delta_{\bar{\nu}_x, 0} - A \sum_{n=0,1,2,\dots} \delta_{\bar{\nu}_x, \pm n\bar{\nu}_x^0} \Phi_{PSF}(\bar{\nu}_x) \right] \quad (2.12)$$

$$\tilde{C}(\bar{\nu}_x, 0) = C_0 \delta_{\bar{\nu}_x, 0} - C_0 A \sum_{n=0,1,2,\dots} \delta_{\bar{\nu}_x, \pm n\bar{\nu}_x^0} \Phi_{PSF}(\pm n\bar{\nu}_x^0) \quad (2.13)$$

In brief, the initial photobleach corresponds to a series of puncta in the spatial Fourier domain positioned at  $(\bar{\nu}_x, \bar{\nu}_y) = (\pm n\bar{\nu}_x^0, 0)$ , each of which is scaled in initial amplitude by the spatial Fourier transform of  $PSF(x)$ , with additional amplitude at the origin  $(\bar{\nu}_x, \bar{\nu}_y) = (0, 0)$  from the overall average fluorescence intensity.

The time-dependent behavior of each point in the FT can be evaluated by an approach analogous to that illustrated in Eq. 2.4 for the  $n$ th harmonic ( $n > 0$ ).

$$\tilde{C}(\bar{\nu}_x, t) = \tilde{C}(\pm n\bar{\nu}_x^0, 0) e^{-(2\pi n\bar{\nu}_x^0)^2 D_{xx} t}; \tilde{C}_n(\pm n\bar{\nu}_x^0, 0) = -C_0 A \Phi_{PSF, x}(\pm n\bar{\nu}_x^0), x \quad (2.14)$$

For a given impulse in the FT image, a single-exponential decay is expected; irrespective of the functional form for  $PSF(x)$ , the time-constant is given by  $\tau = \left[ (2\pi n\bar{\nu}_x^0)^2 D_{xx} \right]^{-1}$ . This single-exponential recovery is in stark contrast to conventional FRAP analysis based



on measurements performed in real-space, for which the time scale for recovery depends sensitively on precise foreknowledge of  $PSF(x)$  for recovery of the diffusion coefficient. The time-constant of the fluorescence recovery in FT-FRAP is independent of  $PSF(x)$ , which allows for simplified mathematical recovery of  $D_{xx}$  while circumventing error associated with imprecise estimates of  $PSF(x)$ .

Through this analysis, comb photobleaching has the additional practical advantage of simultaneously enabling diffusion analysis over multiple length scales. For example, the fourth harmonic will probe diffusion over a length 4-fold shorter than the first harmonic, and by nature of the quadratic dependence on spatial frequency, the fourth harmonic will recover 16-fold faster than the first harmonic for normal diffusion. This disparity enables analyses of both normal and anomalous diffusion without the need for changing instrument settings.

## 2.4 Dot-array-photobleach FT-FRAP

It is interesting to consider instances in which mobility is not isotropic (e.g., within lamellar structures or along microtubules). In such cases, dot array illumination in principle provides single-shot access to the full 2D  $2 \times 2$  diffusion tensor. Generalization of Eq. 2.4 for normal but anisotropic diffusion yields the expression below, in which is the reciprocal of the spatial lattice constant for the periodic illumination.

$$\tilde{C}(\bar{\nu}_0, t)_{hk} = \tilde{C}(\bar{\nu}_0, 0) e^{-(2\pi\bar{\nu})^2 [h^2 D_{xx} + 2hk D_{xy} + k^2 D_{yy}] t} \quad (2.15)$$

Analysis of the decay constant measured for different combinations of  $h$  and  $k$  indices should, in principle, allow for recovery of all three unique elements describing diffusive motion.

## 2.5 Anomalous diffusion

The capability of FT-FRAP to simultaneously measure diffusion over multiple length scales enables quantitative analysis of anomalous diffusion. While normal diffusion is charac-

terized by fluorescence recovery with a quadratic dependence on spatial frequency, anomalous diffusion will produce fluorescence recovery that deviates from a quadratic dependence. The ability to simultaneously interrogate diffusion over several discrete, well-defined distances by FT-FRAP with comb illumination provides a convenient route for quantifying anomalous diffusion, if present.

Numerous mathematical models for anomalous diffusion can be found for trends anticipated under a diverse suite of conditions.[60], [71]–[75] A model based on continuous-time random walk and fractional diffusion is considered in this work because of its general applicability to systems with both time-varying and distance-dependent diffusion.[59] In a continuous-time random walk model, diffusion is approximated as a series of random steps. Normal diffusion is characterized by a Gaussian pdf in step lengths (variance =  $2\sigma^2$ ) and a Poisson pdf in wait times between steps (characteristic wait time =  $\tau$ ). Deviation from normal Brownian diffusion can arise from various sources, two of which we will consider in the anomalous diffusion model used in this work. First, anomalous diffusion can arise when the characteristic wait time,  $\tau$  diverges. When  $\tau$  is finite, as in normal diffusion, the MSD exhibits a linear time dependence. When the distribution of wait times diverges due to binding or association, the time dependence of the MSD deviates from linear and scales with time to the power  $\alpha$ .

$$\langle x^2 \rangle \propto t^\alpha \quad (2.16)$$

Normal diffusion corresponds to  $\alpha = 1$ , subdiffusion corresponds to  $0 < \alpha < 1$ , and superdiffusion corresponds to  $\alpha > 1$ . The fluorescence recovery in this class of anomalous diffusion is modeled as a one-parameter Mittag-Leffler function  $E_\alpha$ .

$$\tilde{C}_n(\bar{\nu}_x, t) = \tilde{C}(\pm n\bar{\nu}_x^0, 0) E_\alpha \left[ - \left( 2\pi n\bar{\nu}_x^0 \right)^2 D_{xx} t^\alpha, \alpha \right] \quad (2.17)$$

The Mittag-Leffler function is a fractional generalization of an exponential function. The one-parameter Mittag-Leffler,  $E_\alpha(z, a)$  converges to an exponential  $E_1(z, 1) = e^z$  for  $\alpha = 1$ , and  $E_0(z, 0) = \frac{1}{1-z}$  for  $\alpha = 0$ . A second source of anomalous diffusion is a deviation in the step-length distribution. Normal diffusion exhibits a Gaussian step-length pdf with a

variance of  $2\sigma^2$ , leading to a quadratic dependence of the diffusion coefficient on spatial frequency. However, in cases where the variance in the step-length distribution diverges, Lévy-flight behavior is observed, and the anomalous diffusion coefficient will adopt a dependence on  $\sigma^\mu$  instead of  $\sigma^2$  for normal diffusion.

$$D_{xx} \equiv \frac{\sigma^\mu}{\tau} \quad (2.18)$$

Lévy-flight diffusion produces a stretched exponential decay in the spatial frequency domain, where the spatial frequency is raised to the power  $\mu$  rather than 2 for normal diffusion.

$$\tilde{C}_n(\bar{\nu}_x, t) = \tilde{C}(\pm n\bar{\nu}_x^0, 0) e^{-(2\pi n\bar{\nu}_x^0)^\mu D_{xx} t} \quad (2.19)$$

A system can exhibit both subdiffusive and Lévy-flight behavior when both  $\tau$  and  $\sigma$  diverge. An equation describing such a system results from modification of the Mittag-Leffler function shown in Eq. 2.17 by replacing the quadratic dependence on the spatial frequency term with the exponent  $\mu$  and by scaling the exponent of  $t$  by  $2/\mu$ .

$$\tilde{C}_n(\bar{\nu}_x, t) = \tilde{C}(\pm n\bar{\nu}_x^0, 0) E_\alpha \left[ - (2\pi n\bar{\nu}_x^0)^\mu D_{xx} t^{2\alpha/\mu}, \alpha \right] \quad (2.20)$$

FT-FRAP is capable of sensitively characterizing anomalous diffusion because it can measure diffusion on multiple length scales. A fit to Eq. 2.20 involves parameters that are likely to have high covariance if the fit is performed with only one recovery curve. By performing a global fit with multiple recovery curves at multiple length scales, the fit can be constrained to recover more accurate values for the parameters describing anomalous diffusion.

## 2.6 Signal power

In comparison to analysis in real space, the Fourier domain analysis with patterned illumination provides a substantial advantage in terms of the available power of the detected signal. Power is conserved upon Fourier transformation, allowing direct comparisons across

both representations. For a Gaussian photobleach spot with a width parameter  $\sigma$ , and peak photobleach depth  $A_p$ , the power is generated by integration over the 2D Gaussian.

$$P_{Gaussian} = \int_0^{512} \int_0^{512} \left[ C_0 A_p e^{-\frac{(x-x_0)^2 + (y-y_0)^2}{2\sigma^2}} \right]^2 dx dy \quad (2.21)$$

In a typical experiment, the Gaussian width is much smaller than the field of view in order to reduce measurement times by minimizing the diffusion length. In the limit that  $\sigma \ll 512$  pixels (assuming a field of view of  $512 \times 512$  pixels), the discrete limits of integration can be safely evaluated as  $\pm\infty$ . The integrals can be further simplified by substituting  $x' = x - x_0$  and noting that  $dx = dx'$  (with analogous substitutions for  $y$ ).

$$P_{Gaussian} \approx (C_0 A_p)^2 \int_{-\infty}^{\infty} e^{-\frac{x'^2}{\sigma^2}} dx' \int_{-\infty}^{\infty} e^{-\frac{y'^2}{\sigma^2}} dy' \approx \pi \sigma^2 (C_0 A_p)^2 \quad (2.22)$$

The power in the impulse in the FT image produced by comb illumination can be similarly calculated by evaluating the same power through integration of the real-space photobleach pattern. For a photobleach depth  $A_p$ , the power in a comb with  $N$  lines is given by the following expression.

$$\begin{aligned} P_{comb} &= \int_0^{512} \int_0^{512} \left[ \sum_{n=1}^N \left( C_0 A_p \delta_{x, \pm n x_0} \otimes PSF(x) \right) \right]^2 dx dy \\ &\approx (C_0 A_p)^2 (512) \sum_{n=1}^N \int_{-\infty}^{\infty} |PSF(x)|^2 dx \approx (C_0 A_p)^2 (512) N \sqrt{\pi \sigma^2} = P_{Gaussian} \times \frac{512 N}{\sqrt{\pi \sigma^2}} \end{aligned} \quad (2.23)$$

The power advantage for comb excitation with a beam PSF with a characteristic width of 2 pixels relative to point excitation is 2,300-fold greater than that in the Gaussian photobleach spot with an identical photobleach depth and 32 lines in the comb. This potential for signal-to-noise enhancement is particularly noteworthy since the peak photobleach amplitude  $A_p$  is bounded to be less than unity and is typically much less than 0.5 to reduce nonlinear effects from saturation and local heating. It is worth emphasizing that this signal increase represents the theoretical upper limit corresponding to a 2,300-fold increase in the total power used for illuminating the sample. In practice, local heating and/or the availabil-

ity of laser power may limit the practical advantages accessible experimentally. Fortunately, distribution of the power over the entire field of view should reduce perturbations associated with heating effects. Furthermore, advances in laser technology are increasing the availability of high-power CW lasers compatible with many photobleaching experiments.

In addition to the power advantage, FT-FRAP with a comb photobleach pattern provides an anticipated intrinsic signal-to-noise advantage through Fourier-domain analysis. White noise is uniformly distributed in both space and spatial frequency. Localized detection in the Fourier domain that changes in amplitude but not shape maintains fixed noise contributions in spatial frequency. In contrast, the spread in the photobleach over time increases the noise contributions over which the signal is integrated.

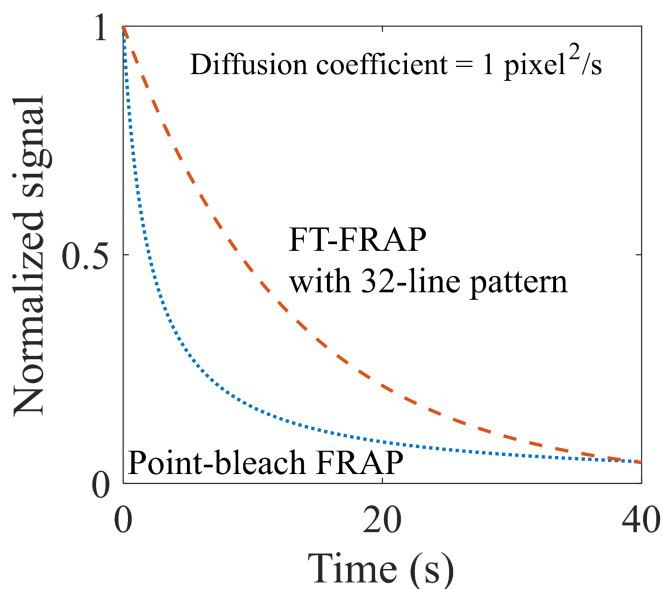


**Figure 2.1.** Decay of FRAP signal over time for point-bleach FRAP and FT-FRAP with 32-line patterned illumination. Signal rapidly degrades for point-bleach relative to comb-illumination even when normalized for total bleach power. In principle, the signal of FT-FRAP increases as the distance between photobleached lines increases.

Direct comparisons between point-bleach and FT-FRAP measurements can be made by considering the SNR of the measurements during recovery. Major increases in signal are po-

tentially accessible in FT-FRAP by distributing greater photobleach excitation power over the entire field of view. For the purposes of direct comparison, we will assume a constant integrated bleach power for both comb-illumination FT-FRAP and point-bleach FRAP. For point-bleach analysis in the spatial domain, the illumination point-spread function (assumed for simplicity to be Gaussian) is convolved with a 2D time-varying Gaussian function, the standard deviation of which is dependent on the diffusion coefficient and time through Eq. 2.8. As the photobleach profile expands, the peak signal  $S$  measured at the center of the photobleach profile is reduced in time scaling as  $S(t) = S_0\sigma_b^2/(\sigma_b^2 + 2Dt)$ , generated by normalizing Eq. 2.8 for an initial peak amplitude of  $S_0$ . An identical scaling arises for the SNR measured in a given pixel when fixing the integrated area of the photobleach peak and considering the increase in number of pixels over which the signal is distributed. For comparison, the integrated cross-section of the peak in the FT domain is independent of time, with a corresponding fixed noise power. The signal (and correspondingly the SNR) in a given harmonic decays exponentially with time with a time-constant given by  $\tau = \left[(2\pi n\bar{\nu}_x^0)^2 D_{xx}\right]^{-1}$ . For a spatial period of 16 pixels between lines consistent with the experimental implementation of FT-FRAP and an initial photobleach width with a standard deviation of 2 pixels, calculations are shown in Figure 2.1 for the anticipated time-dependence of the SNR for point vs. patterned illumination. As can be seen from Figure 2.1, even when normalized for total bleach power, the SNR rapidly degrades for point-bleach relative to comb-illumination. In principle, the integrated SNR of comb illumination can be further increased by increasing the distance between lines, thereby slowing the loss in the spatial harmonic. In practice, implementation may introduce additional  $1/f$  noise contributions not explicitly considered herein.

## 2.7 Phasor analysis of flow in FT-FRAP

The preceding description is based on the assumption of even functions for the comb photobleach pattern relative to the origin of the image (typically, the center). Even assuming the initial photobleach pattern is symmetric about the origin, directional flow within the sample could result in displacements along the flow direction (assumed to be  $x$  for simplicity)

over time. Displacements in real space correspond to shifts in phase in the Fourier domain, such that phase analysis in the FT domain has the potential to inform on flow. Considering comb excitation, a shift of  $\Delta x$  in the initial photobleach pattern will produce shifts in the  $\delta$ -functions associated with the comb.

$$C(x, 0) = C_0 \left[ 1 - A \sum_{n=0,1,2,\dots} (\delta(\Delta x) \otimes PSF(x)) \right] \quad (2.24)$$

In which  $\delta(\Delta x) = \delta_{x, \pm n(x+\Delta x)\bar{\nu}_x^0}$ . The influence of displacement is easily integrated into the FT analysis using the shift theorem, in which displacement by an offset from the origin of  $\Delta x$  is accounted for in the spatial FT through multiplication by  $e^{i2\pi\bar{\nu}\Delta x}$  for a given value of  $n$ .<sup>[76]</sup>

$$\tilde{C}(\bar{\nu}_x, t) = \tilde{C}(\pm n\bar{\nu}_x^0, 0) e^{-(2\pi n\bar{\nu}_x^0)^2 D_{xx}t} e^{i2\pi(n\bar{\nu}_x^0)\Delta x} \quad (2.25)$$

At  $t = 0$ , the initial phase angle of the  $n$ th reflection is related to the argument  $\varphi_n$  of  $\tilde{C}(\bar{\nu}_x, 0)$ , which is simply  $\varphi_n = 2\pi n\bar{\nu}_x^0\Delta x$ . In the absence of time-averaged flow in the  $x$ -direction, the argument of the  $n$ th reflection will be preserved throughout the experiment. If flow is nonzero, then  $\Delta x$  is a function of time. Assuming a constant flow rate of  $q_x = \Delta x/t$ , then  $\Delta x$  can be replaced by  $q_x t + \Delta x_0$  in Eq. 2.25, in which  $\Delta x_0$  is the phase shift at  $t = 0$ . This substitution results in an argument for the  $n$ th peak given by the following equation.

$$\varphi_n = 2\pi n\bar{\nu}_x^0(\Delta x_0 + q_x t) \quad (2.26)$$

Notably, the rate of change in the phase shift from flow is proportional to  $n$ , such that the higher harmonics corresponding to higher spatial frequencies are likely to be more sensitive to flow than the lower harmonics. This trend mirrors analogous sensitivities to time in the fluorescence recovery from diffusion in Section 2.3, in which the higher harmonics report on fast diffusion times measured over short distances.

## 2.8 Patterned versus point photobleaching

It is worthwhile to compare the FT-FRAP approach demonstrated herein with previous studies employing spatial Fourier analysis (SFA) of FRAP measurements. In those prior studies, Fourier analysis was performed to aid in interpretation of recoveries using conventional photobleach illumination of localized points. SFA provided similar computational benefits in the mathematical simplicity arising in the Fourier domain. However, FT-FRAP has a major signal-to-noise advantage over conventional point-illumination. In the numerator, FT-FRAP supports major increases in the signal power ( $>2000$ -fold with comb illumination) by distributing the photobleach amplitude over the entire field of view, whereas conventional point-illumination saturates (photobleach depth approaching unity) at a much lower integrated signal power. Furthermore, patterned illumination enables shifting of the signal to a quiet spatial frequency for noise suppression. By analogy with  $1/f$  noise in electronics, analysis of natural images suggests a power spectrum obeying a  $1/\bar{\nu}$  dependence.<sup>[77]</sup> For optical detection in the shot-noise limit, the variance in signal is proportional to the mean. Since visible photons are often detectable with signal-to-noise approaching the shot-noise limit in instrumentation optimized for FRAP, it stands to reason that the noise in the Fourier domain will also scale with the signal power in an image with natural contrast. Consequently, the low frequency noise power spectrum is also expected to scale with  $1/\bar{\nu}$ , in direct analogy with  $1/f$  noise in electronics. As in electronics, shifting of the signal to a frequency regime with lower noise through modulation can provide a substantial noise reduction.

## 2.9 Diffusion imaging

Patterned photobleaching can be described by Eq. 2.27, where  $\boldsymbol{\rho}$  is position,  $C(\boldsymbol{\rho}, 0)$  is the initial post-bleach image,  $C_0(\boldsymbol{\rho})$  is the pre-bleach image and  $C_b(\boldsymbol{\rho})$  is the photobleach pattern.

$$C(\boldsymbol{\rho}, 0) = C_0(\boldsymbol{\rho}) \cdot C_b(\boldsymbol{\rho}) \quad (2.27)$$



The photobleach pattern,  $C_b(\boldsymbol{\rho})$  can be described as the convolution of the photobleach pattern with the point spread function of the laser beam, shown in Eq. 2.28 as a pictorial equation (not to scale).

$$C_b(\boldsymbol{\rho}) = \text{Comb photobleach} \otimes \text{Point spread function} \quad (2.28)$$

Two-dimensional spatial Fourier transformation of Eq. 2.27 yields Eq. 2.29, where  $\tilde{C}(\bar{\nu}, 0)$  is FT of the initial post-bleach,  $\tilde{C}_0(\bar{\nu})$  is the pre-bleach image. Note that by the convolution theorem  $C_b(\boldsymbol{\rho})$  transforms to the multiplication of FT of the two functions depicted in Eq. 2.28. Also, by the same theorem, the multiplication in Eq. 2.27 become a convolution following Fourier transformation.

$$\tilde{C}(\bar{\nu}, 0) = \tilde{C}_0(\bar{\nu}) \otimes \left( \text{FT of comb photobleach} \cdot \text{FT of PSF} \right) \quad (2.29)$$

If  $C_0(\boldsymbol{\rho})$  from Eq. 2.27 is a constant, as in a homogeneous sample, then  $\tilde{C}_0(\bar{\nu})$  is an impulse and convolution by  $\tilde{C}_0(\bar{\nu})$  is equivalent to multiplication by a factor. However, if  $C_0(\boldsymbol{\rho})$  is not homogeneous but has structure, then the spatial FT of  $\tilde{C}_0(\bar{\nu})$ , which contains information about the pre-bleach, will be convolved with each peak from the FT of the comb photobleach. This will produce a series of peaks that contain duplicate information about the spatial contrast in  $C_0(\boldsymbol{\rho})$ . This relationship is captured in Eq. 2.30, where  $n$  is the

harmonic,  $A_n$  is an amplitude scaling based on the FT of the PSF in Eq. 2.29 and the equation assumes a comb photobleach pattern in the  $x$  axis.

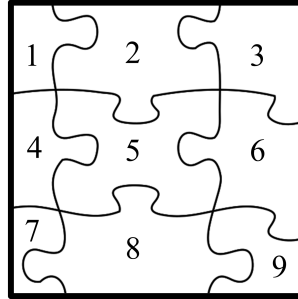
$$\tilde{C}_0(\bar{\nu}_x - n\bar{\nu}_0, \bar{\nu}_y) \approx \tilde{C}_0(\bar{\nu}_x, \bar{\nu}_y) A_n \quad (2.30)$$

The harmonic peaks at  $n\bar{\nu}_0$ , where  $\bar{\nu}_0$  is the fundamental frequency, in theory have an identical relative peak shape which contains information about the structure of the image. This equation only holds for low frequency features where  $\bar{\nu}_x < \frac{\bar{\nu}_0}{2}$  to ensure no overlap between peaks in the spatial frequency domain.

Before bringing in the time-dependence, we will assume  $C_0(\boldsymbol{\rho})$  contains segmented domains of local, isotropic diffusion with diffusion coefficient  $D_i$  in each domain,  $i$ , as shown in Eq. 2.31 and Eq. 2.32.

$$C_0(\boldsymbol{\rho})_{tot} = \sum_i C_0(\boldsymbol{\rho})_i \quad (2.31)$$

$$\tilde{C}_0(\bar{\boldsymbol{\nu}})_{tot} = \sum_i \tilde{C}_0(\bar{\boldsymbol{\nu}})_i \quad (2.32)$$



$i$  domains 1 to 9

The solution in Eq. 2.4 holds for each domain, such that the time-evolving peak shape about  $n\bar{\nu}_0$  will be:

$$\tilde{C}(\bar{\nu}_x - n\bar{\nu}_0, \bar{\nu}_y, t)_{tot} = \sum_i \tilde{C}(\bar{\nu}_x - n\bar{\nu}_0, \bar{\nu}_y, 0)_i e^{-4\pi^2(n\bar{\nu}_0)^2 D_i t} \quad (2.33)$$

Centering the spatial frequency domain about  $n\bar{\nu}_0$  and taking the two-dimensional inverse FT yields Eq. 2.34, noting that the exponential term is not a function of  $\bar{\nu}_x$  and  $\bar{\nu}_y$  (when  $\bar{\nu}_x$ ,

$\bar{\nu}_y < \bar{\nu}_0$  ).When centering the spatial frequency domain about  $n\bar{\nu}_0$ , it is important to merge the two symmetric peaks to preserve phase information.

$$C(x, y, t)_{tot} = \sum_i C(x, y, 0)_i e^{-4\pi^2(n\bar{\nu}_0)^2 D_i t} \quad (2.34)$$

The integrated amplitude of each segment  $i$  in the inverse FT image decays with a single exponential dependence on  $n\bar{\nu}_0$  and  $D_i$ . An analogous expression can be produced for anomalous diffusion.

$$C(x, y, t)_{tot} = \sum_i C(x, y, 0)_i E_{\alpha_i} \left[ - \left( 2\pi n\bar{\nu}_x^0 \right)^{\mu_i} D_i t^{2\alpha_i/\mu_i}, \alpha_i \right] \quad (2.35)$$

### 3. MATERIALS AND METHODS

FT-FRAP was performed using two different fluorescence microscopes: one using two-photon excited fluorescence, and the other using one-photon excited fluorescence. FT-FRAP was also performed using two different illumination patterns: comb illumination and dot matrix illumination.

#### 3.1 Two-photon excited fluorescence (TPEF) microscopy

A schematic of the TPEF microscope used in this study for comb photobleach FT-FRAP is depicted in Figure 3.1A. The light source of the microscope was an 80 MHz, Ti:Sapphire laser (Mai Tai, Spectra-Physics, Santa Clara, CA), tuned to 800 nm. The laser beam was scanned across the sample using a galvanometer/resonant mirror pair with an 8.8 kHz resonant scanning mirror (Electro-optical Products Corporation, Ridgewood, NY) for the fast-scan axis and a galvanometer mirror (Cambridge-Tech, Bedford, MA) for the slow-scan axis. The mirror pair was  $4f$ -coupled to the back of a 10X, 0.3 NA objective (Nikon, Melville, NY) to enable beam-scanning imaging at the focal plane. Each pixel in the FOV was measured sequentially as the laser beam was raster-scanned across the sample. The high light fluence of the laser beam produced TPEF from emitters in the focal volume. The TPEF was collected in the epi direction using a dichroic mirror (650DCXR, Chroma, Bellows Falls, VT) and a band-pass filter (FGS900, Thorlabs, Newton, NJ) to isolate the TPEF, and a photomultiplier tube (H7422P-40 MOD, Hamamatsu, Hamamatsu City, Shizuoka, Japan) as the detector. The signal from the photomultiplier tube was digitized synchronously with each laser pulse and mapped onto a  $512 \times 512$ -pixel image using custom software using MATLAB (MathWorks, Natick, MA). Scanning mirrors and data collection were synchronized using custom phase-locked timing electronics.<sup>[57]</sup> All videos in this study were recorded at approximately 4 frames per second.

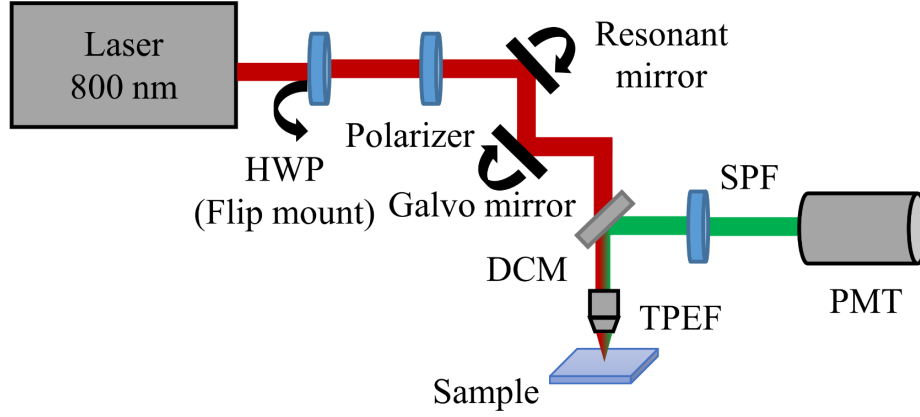


**Figure 3.1.** Instrument schematic of a nonlinear-optical beam-scanning microscope used for multi-photon FT-FRAP. A HWP on a flip mount was used to modulate from low power ( 50 mW) to high power ( 500 mW) for the photobleach. Beam scanning was performed with galvanometer (slow axis) and resonant (fast axis) mirrors. DCM = dichroic mirror, HWP = half-wave plate, PMT = photomultiplier tube, SPF = short-pass filter, TPEF = two-photon excited fluorescence.

### 3.2 Comb-photobleach FT-FRAP

A simple change to the scan pattern of the galvanometer (slow axis) mirror was used to generate a comb photobleach pattern at the sample. Following an initial low-power period for baseline TPEF microscopy of the full field of view, patterned photobleaching was performed simply by changing the number of steps in the ramp function driving the galvanometer mirror from 512 (used for normal imaging) to an integer fraction of 512 corresponding to the fundamental spatial frequency (e.g., 8, 16, 32 pixels =  $1/\bar{\nu}_0$ ). The dwell time per step was also increased proportionally such that the repetition rate of the slow axis mirror was independent of the number of lines in the comb photobleach pattern. A flip mount with a half-wave plate (depicted in Fig. 3.1) was synchronized to switch the excitation source from low power to high power concurrently with the reduction in ramp steps. This protocol resulted in a comb photobleach pattern as seen in Figure 4.1A. After 2 seconds at high power the flip mount was removed, reducing the laser power, and the number of steps for

the slow axis mirror was changed back to 512 to facilitate normal imaging at low power to track the fluorescence recovery of the sample.

### 3.3 Dot matrix photobleach FT-FRAP

A commercial FRAP microscope (Formulatrix, Bedford, MA) was modified in-house to support periodically patterned illumination during photobleaching for FT-FRAP experiments, as shown in Figure 3.2. A detailed description of the commercial microscope has been published previously.[58] A diffractive optical element (DOE) (DE-R 244) (HOLOEYE Photonics AG, Berlin, Germany) was added to the excitation light path of the microscope immediately before the dichroic mirror. The DOE diffracted the photobleach laser into a matrix of photobleach spots during the photobleaching phase of the FRAP experiment. Distributing the photobleach power across many points in the sample enabled illumination with a higher power light source for photobleaching without saturation of the sample. Consequently, the 10 mW, 532 nm photobleaching laser in the FRAP microscope was replaced with a 5 W, 532 nm, continuous-wave laser (SpectraPhysics Millennia SpectraPhysics, Santa Clara, CA), which was coupled into the microscope with a Thorlabs custom fiber optic patch cable at the location of the original photobleaching laser. The photobleach time was approximately 2 seconds and produced a dot matrix pattern that could be analyzed in the spatial frequency domain to characterize diffusion.

### 3.4 Sample preparation

Solution of fluorescein isothiocyanate bovine serum albumin (FITC-BSA) in 2:1 glycerol/water was prepared by dissolving lyophilized FITC-BSA in water at a concentration of 3 mg/mL and mixing at a ratio of 1:2 with glycerol to produce a final FITC-BSA concentration of 1 mg/mL. A solution of trimethyl rhodamine immunoglobulin G (TMR-IgG) in PBS was prepared by dissolving lyophilized TMR-IgG in PBS at a concentration of 1 mg/mL. Solutions of 2 mg/mL fluorescein isothiocyanate (FITC) polydextran (2 MDa) (Millipore-Sigma, Burlington, MA) were used to evaluate the FT-FRAP approach. These fluorescently labeled molecules were solubilized in either 50/50 glycerol/water or in an aqueous solution

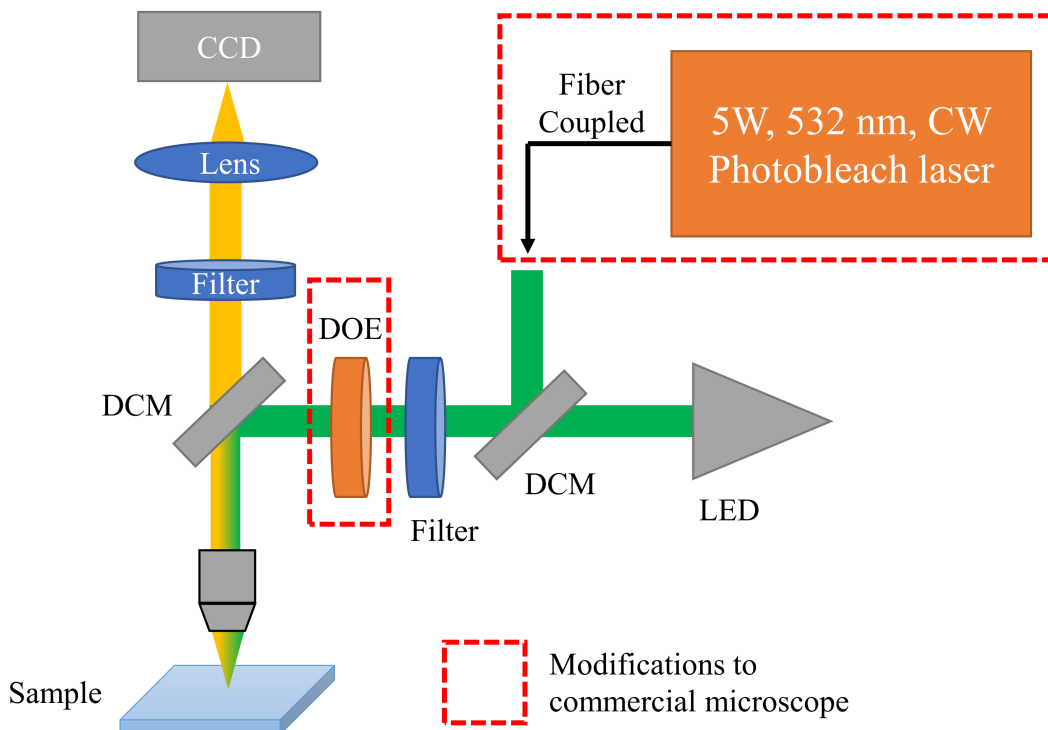


**Figure 3.2.** Instrument schematic of a commercial FRAP microscope that was modified for dot array photobleach FT-FRAP. Modifications are indicated by red dashed boxes. A more powerful laser replaced the original photobleach laser and a DOE was added to the excitation light path to produce a dot array photobleach pattern. DCM = dichroic mirror, DOE = diffractive optical element, CCD = charge-coupled device camera, LED = broadband green light emitting diode.

of 22 mg/mL hyaluronic acid (15 MDa) (Lifecore Biomedical, Chaska, MN). Solutions were mixed thoroughly prior to FRAP analysis.

### 3.5 Data analysis

Analysis of the FT-FRAP data was performed using custom software written in-house using MATLAB. A 2-dimensional FT was taken of each image. FT-FRAP curves were recovered by integrating over peaks in the FT magnitude. A fit was performed to recover the diffusion parameters using Eq. 2.14 for normal diffusion and Eq. 2.20 for anomalous diffusion. A MATLAB function written by Roberto Garrappa was used for evaluating the

Mittag-Leffler function in Eq. 2.20.[78] Phasor analysis of flow was performed by taking the argument of the complex-valued 2D-FT peaks and relating the phase back to flow velocity through Eq. 2.26. Uncertainties in the fits were calculated based on the second derivative of  $\chi^2$ -space in the vicinity of the minimum and were obtained from the covariance matrix,  $\mathbf{X}$  which was calculated from the Jacobian,  $\mathbf{J}$  and the variance in the residuals,  $v_R$ , as shown in Eq. 3.1.

$$\mathbf{X} = v_R \left( \mathbf{J}^T \times \mathbf{J} \right)^{-1} \quad (3.1)$$



## 4. NORMAL DIFFUSION CHARACTERIZATION

The capabilities of comb-photobleach and dot-array-photobleach FT-FRAP for characterizing normal diffusion were evaluated using three analytes: a polymer, a protein, and an antibody.

### 4.1 Polymer diffusion analysis by comb-photobleach FT-FRAP

As shown in Figure 4.1A, a comb pattern was employed for photobleaching a solution of 2 mg/mL FITC-polydextran (2 MDa) in 50/50 glycerol/water. Following photobleaching, spatial Fourier transformation produced sharp puncta with symmetric amplitudes about the origin peak as shown in Figure 4.1B. As diffusion progressed, the FT peak intensities exhibited simple exponential decays, as shown in Figure 4.1C. These observations are in excellent agreement with theoretical predictions in Eq. 2.4. Consistent with prior arguments on signal power, the FT-FRAP analysis clearly provides high signal-to-noise photobleaching curves by combining the analysis over the entire field of view.

Comb patterns for photobleaching enabled simultaneous analysis over multiple length scales through the  $n$ th spatial harmonics  $\bar{\nu}_{x,n}$ , as shown in Figure 4.1. Theoretical predictions in Eq. 2.14 suggest an exponential decay of each impulse with a decay constant given by  $\tau = 1/[4\pi^2(n\bar{\nu}_x^0)D_{xx}]$ . Higher harmonics are expected to exhibit faster decays with a quadratic dependence on  $n$  for normal diffusion. The decays of the first and second harmonic peaks were fit to Eq. 2.14, recovering a diffusion coefficient of  $3.70 \pm 0.02 \mu\text{m}^2/\text{s}$ . The reported uncertainty is the standard deviation of the fit.

### 4.2 Protein diffusion analysis by comb photobleach FT-FRAP

Spatial frequency diffusion analysis of FITC-BSA is shown in Figure 4.2. A 16-line comb photobleach pattern, shown in Figure 4.2A, was used to probe the mobility of FITC-BSA. The comb photobleach pattern produced a one-dimensional series of peaks in the spatial frequency domain, as shown in Figure 4.2B. The central peak represents the fluorescence background and contains no diffusion information. However, the other peaks represent har-

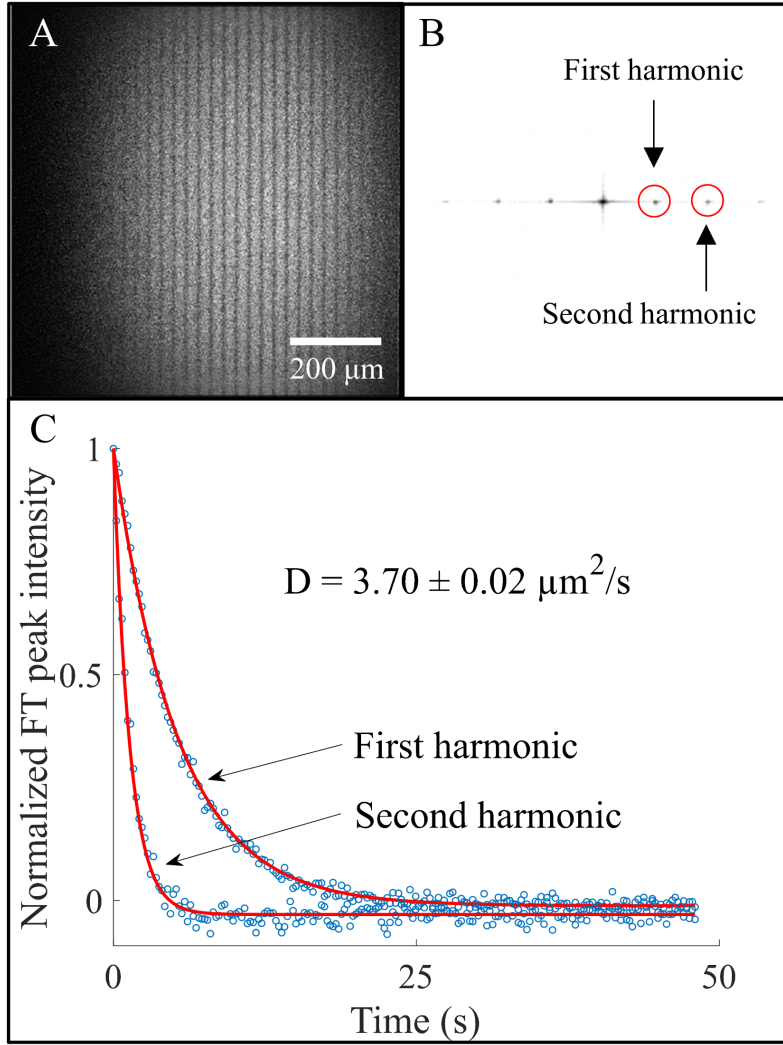


**Figure 4.1.** Multiphoton excited FT-FRAP with comb photobleach of FITC-polydextran (2 MDa) dissolved in 50/50 glycerol/water. A) Image of the solution immediately after a 32-line comb bleach. B) 2D-FT of (A) with the circled peaks corresponding to the first and second spatial frequency harmonics of the 32-line comb bleach. C) Fluorescence recovery of the first and second harmonic peaks with best-fit curves recovering a diffusion coefficient,  $D = 3.70 \pm 0.02 \mu\text{m}^2/\text{s}$ . The reported uncertainty is the standard deviation of the fit.

monics from the Fourier series of the comb photobleach pattern. The time-dependent decay of the first harmonic and the second harmonic are plotted in Figure 4.2C and 4.2D respectively, along with fits to Eq. 2.14. Both harmonics exhibit a simple exponential decay, consistent with expected theory for normal diffusion. When the harmonics were fit indepen-

dently, they recovered diffusion coefficients that were in good agreement with one another ( $8.23 \pm 0.05$  and  $8.25 \pm 0.09 \mu\text{m}^2/\text{s}$  respectively), despite having significantly different decay constants. Uncertainty values are the standard deviation of the least-squares fit. As predicted by theory, the decay time-constants were dependent on the square of the Euclidean distance from the origin in the spatial frequency domain. For this reason, the first and second harmonic exhibit decay time-constants that differed 4-fold but recovered approximately the same diffusion coefficient.

The comb bleach in Figure 4.2 is particularly well suited for multiphoton excitation in FRAP. Efficient two-photon excitation requires high peak intensity for the excitation beam, which is typically achieved by focusing an incident ultrafast laser to a tight point-spread function. Tight focusing of an intense beam at a single location as is typically performed in point-bleach FRAP can also produce rapid local heating. In such instances, the dynamics of recovery can potentially be altered by damage/modification within the focal volume. Rapid beam-scanning allows distribution of this deposited heat over substantially larger volumes, with much smaller corresponding transient temperature increases. In beam-scanning imaging using raster patterns, comb bleaching can be achieved simply by altering the slow-scan pattern from a continuous ramp to instead translocate the beam to discrete stepped locations, as demonstrated in Figure 3.1. The same hardware is used both for patterning the photobleach and subsequently recording the recovery, ensuring co-alignment.

### 4.3 Antibody diffusion analysis by dot-array-photobleach FT-FRAP

Periodically patterned photobleaching using a dot array is shown in Figure 4.3 for diffusion analysis of tetramethyl rhodamine-labeled immunoglobulin G (TMR-IgG) as a model antibody. This periodic pattern was produced using diffractive optics. The undiffracted (zero-order) beam resulted in the deep photobleach at the origin of the array, enabling simultaneous point-bleach and FT analyses. In the spatial Fourier domain, the dot array photobleach pattern produced a two-dimensional set of peaks, as shown in Figure 4.3B. As in 2D electron diffraction, each peak corresponds to a lattice plane in reciprocal space, described by the lattice indices  $h$  and  $k$ . The central peak represents the average fluorescence intensity

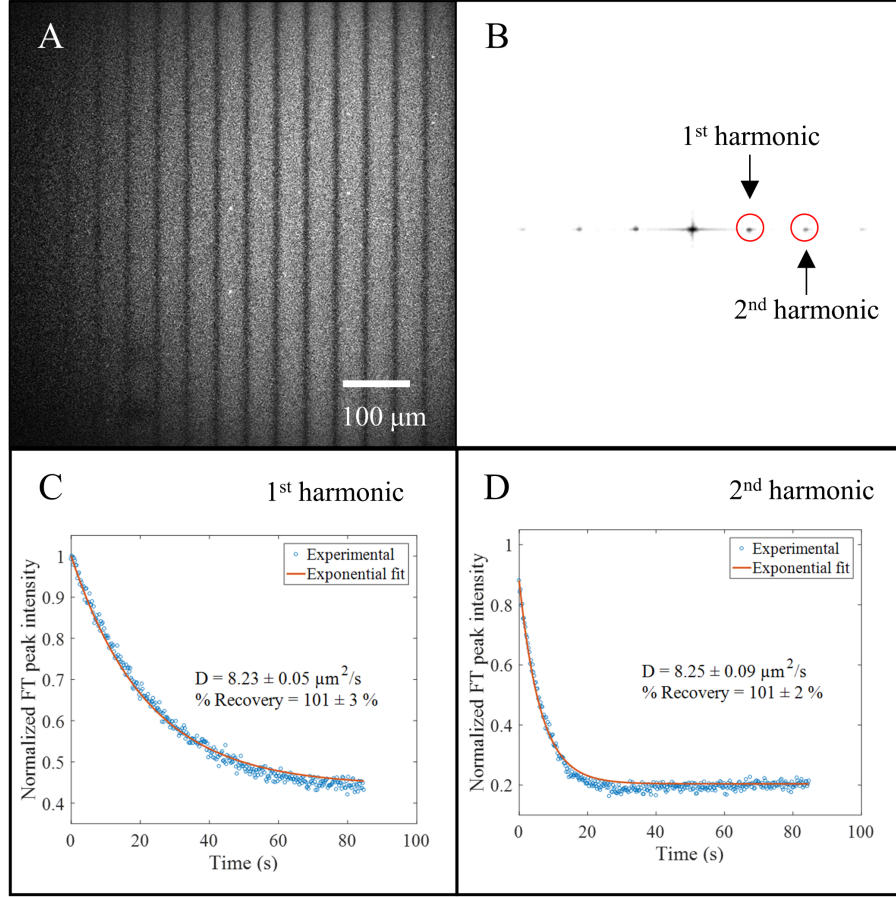


**Figure 4.2.** FT-FRAP with comb bleach of FITC-BSA dissolved in a 2:1 solution of glycerol/water. A) Image of the solution immediately subsequent to a 16-line comb bleach. B) 2D-FT of (A). C) Fluorescence recovery measured at the 1st harmonic of the 2D-FT. D) Fluorescence recovery measured at the 2<sup>nd</sup> harmonic of the 2D-FT.

of the image; while containing no diffusion information, this peak does enable quantification of (and correction for) fluorescence changes from photobleaching during the recovery measurements. Theory predicts that the decay time-constant of these peaks is dependent on the diffusion coefficient and the Euclidean distance ( $h^2 + k^2$ ) in reciprocal space from the origin of the spatial Fourier transform image. In the absence of flow and for isotropic diffusion, timescales for recovery are dictated solely by the distance scale and not the direction. Consistent with this expectation, peaks were pooled according to their distance from the origin ( $h^2 + k^2 = 1$  or  $h^2 + k^2 = 2$ ) and the time-dependent decay of the peaks was plotted in Figure

4.3C, along with a fit to Eq. 2.15. As with the comb photobleach pattern, the decays were in good agreement with simple exponential trends predicted by theory for normal diffusion, and the data exhibited the predicted dependence on Euclidean distance. When all the data from  $h^2 + k^2 = 1$  and  $h^2 + k^2 = 2$  peaks were fit, the best-fit diffusion coefficient of TMR-IgG was  $1.92 \pm 0.03 \mu\text{m}^2/\text{s}$ , where the uncertainty is the standard deviation of the fit.

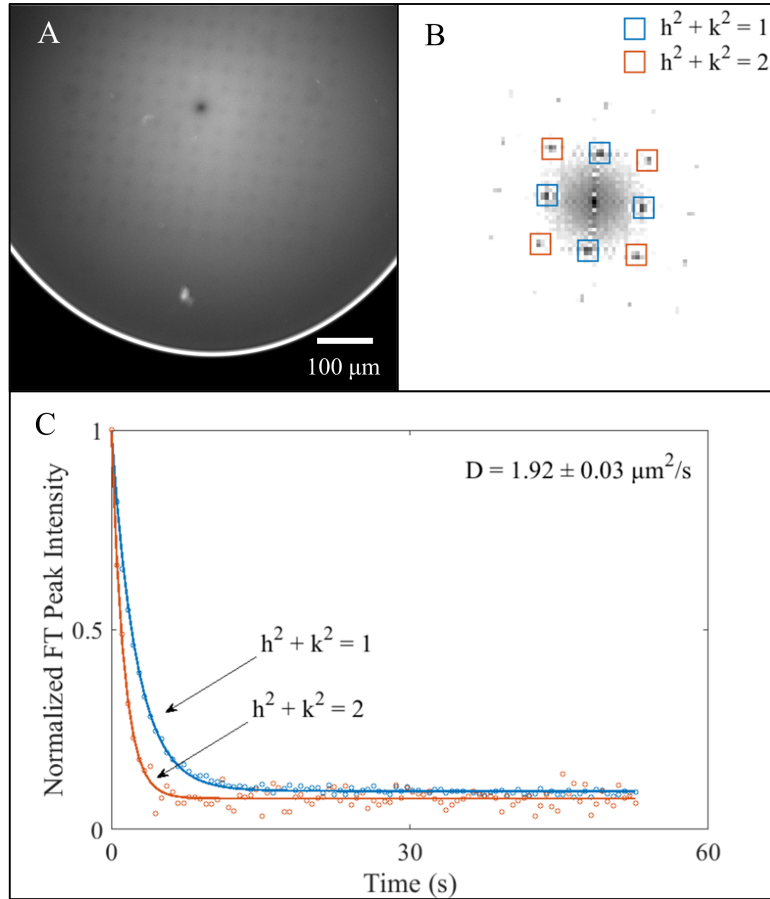


**Figure 4.3.** FT-FRAP with dot array bleach of TMR-IgG dissolved in PBS. A) Image of the solution immediately after dot array bleach. B) 2D-FT of (A). Blue and red circles indicate peaks that are equidistant from the origin C) Fluorescence recovery of pooled peaks with best-fit curves. The best-fit value for the diffusion coefficient was  $1.92 \pm 0.03 \mu\text{m}^2/\text{s}$ . The reported uncertainty is the standard deviation of the fit.

## 5. FLOW CHARACTERIZATION

The impact of flow on the phase of the recovered Fourier transform peaks was evaluated in the results shown in Figure 5.1, in which unidirectional fluid motion was simulated by sample translation with an automated stage during the fluorescence recovery. The sample under investigation was an aqueous solution of 2 mg/mL FITC-polydextran (2 MDa) in 50/50 glycerol/water. Recovery of the diffusion coefficient in FT-FRAP only requires analysis of the magnitude of the Fourier peaks. However, the real and imaginary components of the Fourier peaks contain information about the spatial phase of the photobleach pattern. Figure 5.1A shows an oscillatory decay of the real and imaginary components of the first and second harmonic peaks. The phase of the Fourier peak can be calculated using the argument of the complex number describing the peak at each time point. Figure 5.1B shows the phase shift of a sample that was not translated and the phase shift of the first and second harmonic peaks of a sample that was translated. Consistent with the expression in Eq. 2.26, the phase angle changed linearly with time for the system undergoing directional translation in the  $x$ -direction of the photobleach comb, with a proportionality constant of  $2\pi n \bar{v}_x^0 q_x$ . Consequently, the  $n$ th harmonic is predicted to exhibit an  $n$ -fold increase in the rate of phase angle change over time relative to the fundamental peak. From the results summarized in Figure 5.1B, precisely this trend was observed in the measurements, in excellent agreement with the theoretical predictions. The measured flow rate for the translated sample ( $4.14 \pm 0.02 \mu\text{m/s}$ ; uncertainty is the standard deviation of the fit) matched the measured translation rate of the sample stage ( $4.0 \pm 0.4 \mu\text{m/s}$ ; uncertainty is the standard deviation of three measurements).

Interestingly, statistically significant flow of  $0.09 \pm 0.01 \mu\text{m/s}$  was observed even in the absence of sample translation. This subtle but nonzero flow is attributed to slow sample convection within the viscous 50/50 glycerol/water solvent. The sensitivity of phase analysis is noteworthy, as this flow is  $>40$  times slower than the sample translation and corresponds to a displacement of approximately 1-2 pixels ( $2 \mu\text{m}$ ) over the entire 25 seconds of data collection. It should be noted that flow (in the absence of mixing) only changes the phase of the FT peak and not the magnitude. Phase changes are independent of the magnitude and do not influence the fluorescence recovery curve.

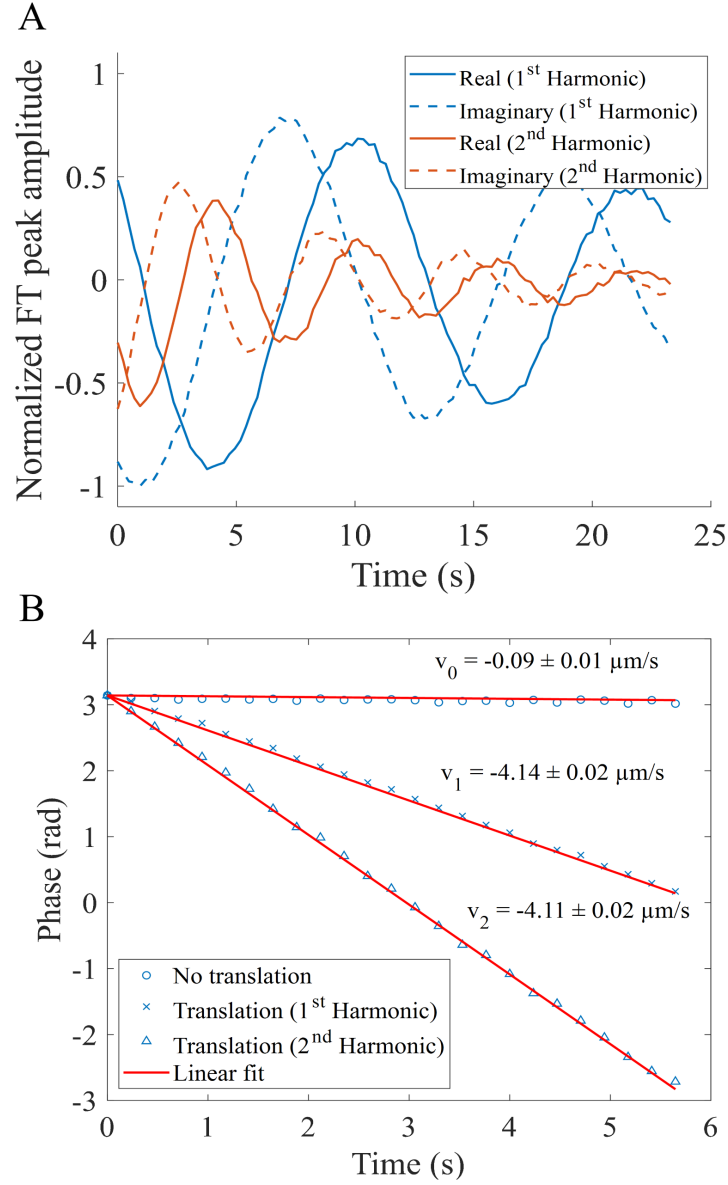


**Figure 5.1.** Bulk flow measured by FT-FRAP of FITC-polydextran (2 MDa) in 50/50 glycerol/water. A) Real and imaginary amplitudes of the 2D-FT fundamental and 2<sup>nd</sup> harmonic peaks upon sample translation during diffusion. B) Phase calculated from real and imaginary amplitudes of 2D-FT peaks. The non-translated sample has minimal bulk flow. The velocities calculated from the fundamental and 2<sup>nd</sup> harmonic peaks of the translated sample are within one standard deviation of each other and close to the translation rate of the sample stage ( $4.0 \pm 0.4 \mu\text{m/s}$ ) after correcting for bulk flow from convection. The reported uncertainties are the standard deviation of the fit.

## 6. ANOMALOUS DIFFUSION CHARACTERIZATION

Additional results were obtained to characterize anomalous diffusion in a viscous matrix. Figure 6.1 shows FT-FRAP with a comb photobleach pattern on FITC-polydextran (2 MDa) in 22 mg/mL hyaluronic acid (HA). HA is a glycosaminoglycan polymer that is found throughout the connective tissues of the body. The physiological functions in which HA is involved include lubrication, wound repair, and cell migration. HA is known to increase viscosity when added to aqueous solution. In this experiment, the fluorescence recovery of the first three spatial harmonics of the comb photobleach pattern was analyzed to characterize anomalous diffusion of FITC-polydextran in a solution with HA.

Several models for anomalous diffusion were considered. First, the three harmonics were fit to a model for systems with subdiffusive mobility, described in Eq. 2.17. Subdiffusion was considered because of possible binding and unbinding or association and dissociation of the FITC-polydextran with the HA matrix. However, analysis with this model did not produce a satisfactory fit because the data did not exhibit a quadratic dependence on spatial frequency. Second, the data were fit to a model for systems exhibiting Lévy flight, described in Eq. 2.19. Lévy flight behavior was considered because of possible crowding or trapping by HA acting as an obstacle to constrict free diffusion of the FITC-polydextran. While the Lévy flight model produced best-fit curves with a better match for the spatial frequency dependence, the shape of the best-fit curves was exponential and far from a good fit to the fluorescence recovery curves. Models incorporating just one of these two effects (subdiffusion and Lévy flight) were insufficient to describe the data.

Third, a global fit of the first three harmonics to a combined subdiffusion-Lévy flight model, described in Eq. 2.20, was performed to recover the anomalous diffusion coefficient  $D = 1.124 \pm 0.008 \mu\text{m}^\mu/\text{s}^{2\alpha/\mu}$ , the subdiffusive parameter  $\alpha = 0.571 \pm 0.003$ , and the Lévy flight parameter  $\mu = 1.173 \pm 0.006$ . The reported uncertainties are the standard deviations in the fit. The result of this fit is shown in Figure 6.1. The combined model was able to account for both the spatial frequency dependence of the harmonics and the shape of the recovery curves, which deviates from exponential. The value of  $\alpha < 1$  indicates that the



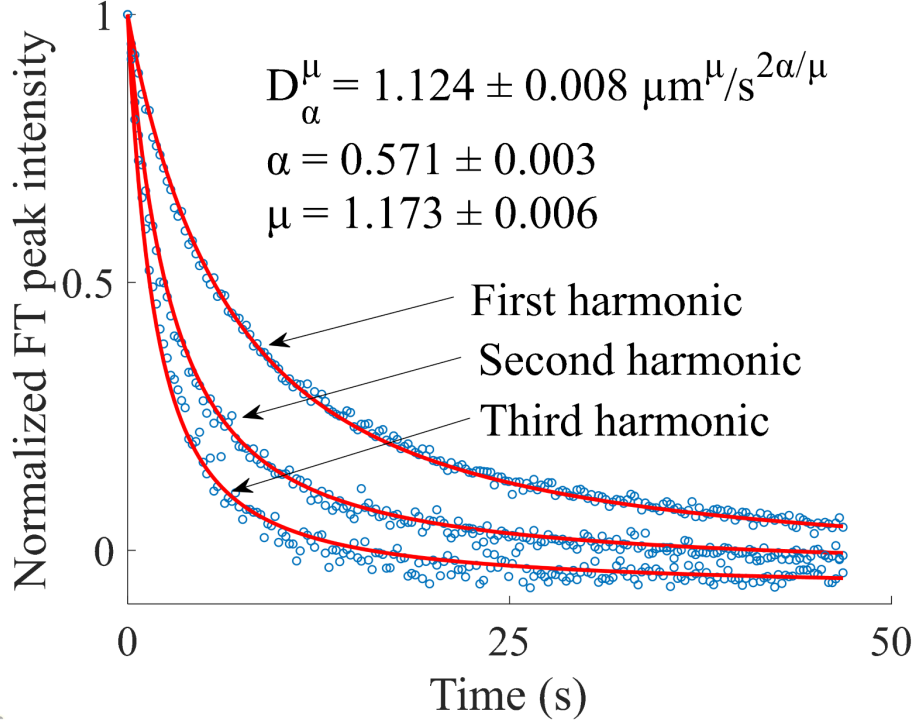


**Figure 6.1.** Harmonic analysis of anomalous diffusion with FITC-polydextran (2 MDa) in 22 mg/mL hyaluronic acid. Fluorescence recovery of the first, second, and third harmonics are fit to a modified Mittag-Leffler function to recover the anomalous diffusion coefficient,  $D = 1.124 \pm 0.008 \mu\text{m}^\mu/\text{s}^{2\alpha/\mu}$ , the subdiffusion parameter,  $\alpha = 0.571 \pm 0.003$ , and the Lévy flight parameter,  $\mu = 1.173 \pm 0.006$ . The recovered parameters reveal subdiffusive and Lévy flight behavior in the sample. The reported uncertainties are the standard deviations in the fit.

characteristic wait time diverges (subdiffusion). Furthermore, the value for  $\mu < 2$  indicates that the step length variance diverges (Lévy flight).

The results of the analysis demonstrate that FT-FRAP can sensitively and precisely disentangle covariant parameters describing anomalous diffusion by simultaneously fitting to multiple harmonics acquired in parallel. The same analysis performed with only the first harmonic yields lower confidence in the recovered parameters:  $D = 1.9 \pm 0.1 \mu\text{m}^\mu/\text{s}^{2\alpha/\mu}$ ,  $\alpha = 0.69 \pm 0.01$ , and  $\mu = 1.57 \pm 0.05$ . The reduction in precision likely arises from the increase in covariance in the single-harmonic fit; the recovered parameters are highly correlated ( $D$  &  $\alpha = 0.976$ ,  $D$  &  $\mu = 0.995$ , and  $\alpha$  &  $\mu = 0.993$ , where  $\pm 1$  corresponds to perfectly

correlated/anti-correlated parameters). By comparison, the correlation coefficients obtained in the three-harmonic fit are much less significant:  $D$  &  $\alpha = -0.204$ ,  $D$  &  $\mu = 0.286$ , and  $\alpha$  &  $\mu = 0.850$ . Comparison with a one-harmonic fit demonstrates that measuring diffusion at multiple length scales with FT-FRAP can substantially increase statistical confidence in the parameters recovered from fitting to an anomalous diffusion model by constraining the model to describe diffusion globally.

## 7. DIFFUSION IMAGING

To demonstrate experimentally the capability of FT-FRAP to map diffusion locally, diffusion imaging by FT-FRAP was performed using a comb photobleach pattern on two samples containing HA and FITC-dextran.

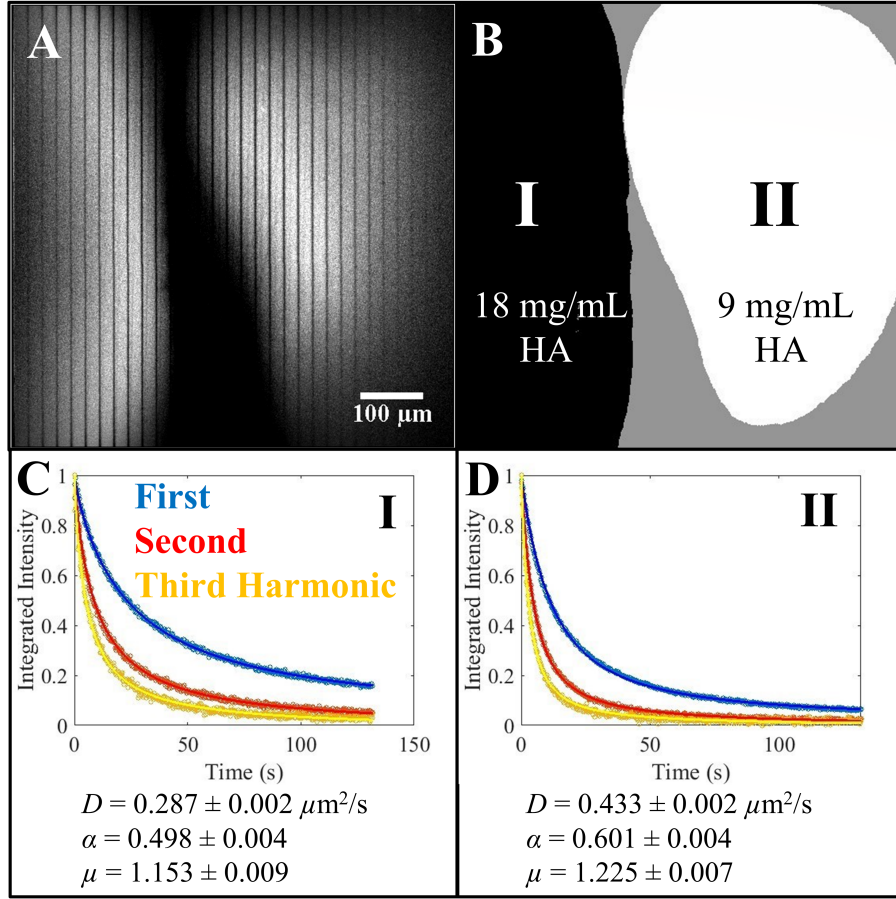


**Figure 7.1.** Diffusion imaging by FT-FRAP of two droplets containing FITC-dextran (2 MDa) and varying concentration of HA. A) Fluorescence image of the droplets after photobleaching. B) Segmented image defining the boundaries of regions I (18 mg/mL HA) and II (9 mg/mL HA). C) Decay curves of the first, second, and third spatial frequency harmonics in region I. D) Decay curves of the first, second, and third spatial frequency harmonics in region II. Regions I and II exhibit significantly different diffusion coefficients  $D$  and anomalous diffusion parameters  $\alpha$  and  $\mu$ .

The first system used to evaluate diffusion imaging by FT-FRAP had two regions separated by an air gap, as shown in Figure 7.1. Droplet I was composed of a solution of 18 mg/mL hyaluronic acid (HA) and droplet II was composed of a solution of 9 mg/mL HA. Both droplets contained 1 mg/mL FITC-dextran (2 MDa). Figure 7.1A shows a TPEF image of the sample immediately after photobleaching. Figure 7.1B shows a segmented image of 7.1A. The image was segmented into two regions so that diffusion analysis could be performed separately on each region of the sample. Figures 7.1C & 7.1D show the decay of the spatial frequency harmonics over time for regions I and II, respectively. Anomalous diffusion parameters were recovered by a least-squares fit of the decay curves for regions I and II to Eq. 2.35 and are shown in Figure 7.1. These best-fit values demonstrate that there is a significant difference in diffusion behavior between regions I and II. A simple point-bleach FRAP experiment would only be able to characterize one of the two diffusion environments at a time and FT-FRAP analysis without diffusion imaging would yield the averaged diffusion behavior over the entire field of view, rather than localized diffusion characteristics. FT-FRAP with diffusion imaging enables simultaneous measurements of local diffusion in different regions of the FOV.

The second system used to evaluate diffusion imaging by FT-FRAP was a heterogeneous sample with two distinct adjacent regions, as shown in Figure 7.2. The sample was composed of photo-crosslinked methacrylated HA (MeHA) spheres surrounded by collagen in PBS. Both the MeHA spheres and surrounding solution contained 1 mg/mL FITC-dextran (2 MDa). Figure 7.2A shows a TPEF image of the sample before photobleaching. Figure 7.2B shows a segmented image of 7.2A. The image was segmented into two regions so that diffusion analysis could be performed separately on each region of the sample. Figures 7.2C & 7.2D show the decay of the spatial frequency harmonics over time for regions I and II, respectively. Diffusion parameters were recovered by a least-squares fit of the decay curves for regions I and II to Eq. 2.35 and Eq. 2.14, respectively, and are shown in Figure 7.2. These best-fit values demonstrate that there is a significant difference in diffusion behavior between regions I and II. Anomalous diffusion is observed in region I, whereas normal diffusion is observed in region II. Furthermore, the recovery in region I is much faster than the recovery observed in region II. A simple point-bleach FRAP experiment would only be able to characterize one

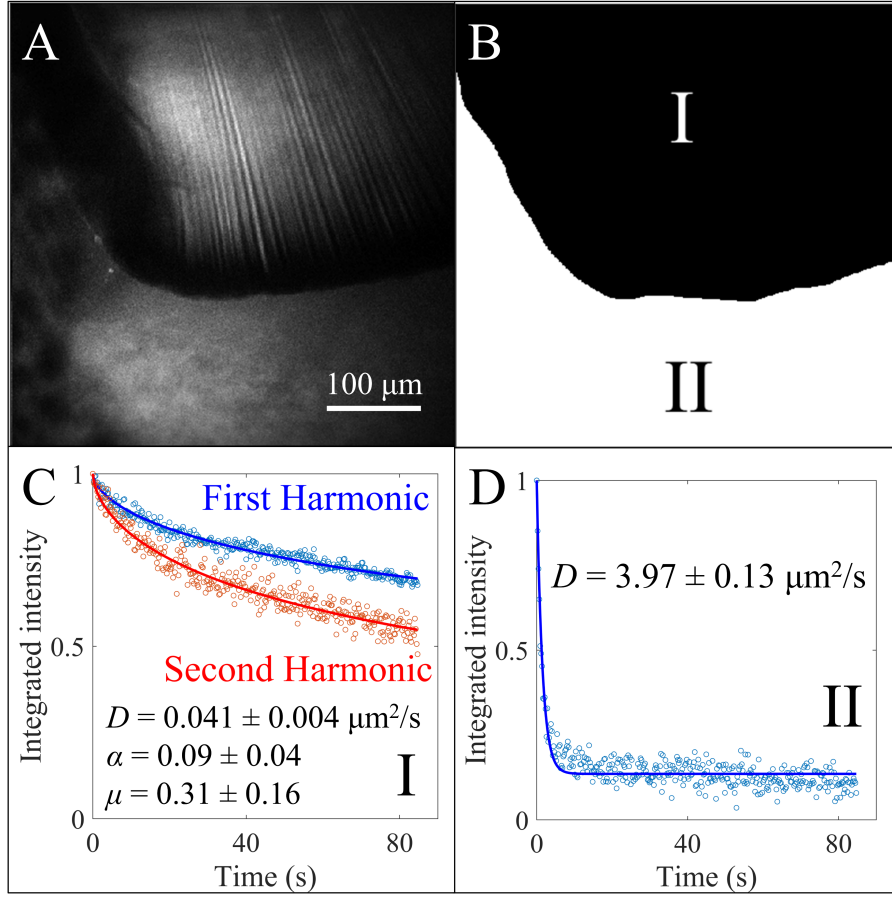


**Figure 7.2.** Diffusion imaging by FT-FRAP of FITC-dextran (2 MDa) diffusing in a sphere of methacrylated HA (MeHA) surrounded by collagen in PBS. A) Fluorescence image of the MeHA sphere before photobleaching. B) Segmented image defining the boundaries of regions I (MeHA sphere) and II (collagen). C) Decay curves of the first and second spatial frequency harmonics in region I, exhibiting anomalous diffusion. D) Decay curves of the first spatial frequency harmonics in region II, exhibiting normal diffusion. Regions I and II exhibit significantly different diffusion behavior.

of the two diffusion environments at a time and FT-FRAP analysis without the diffusion imaging approach would yield the averaged diffusion behavior over the entire field of view, rather than localized diffusion characteristics. FT-FRAP with diffusion imaging enables simultaneous measurements of local diffusion in different regions of the FOV.

## 8. CONCLUSION

FT-FRAP with patterned illumination has been described theoretically and demonstrated experimentally to characterize normal and anomalous diffusion. Relative to conventional point-bleach FRAP, FT-FRAP has the advantages of mathematical simplicity, higher SNR, representative sampling, and multi-photon compatibility. Proof-of-concept measurements with model systems showed good agreement with theory. Flow was quantified using the phase of the real and imaginary components of the FT peaks. Anomalous diffusion was characterized by FT-FRAP through a global fit to multiple harmonics of the photobleach pattern.

Diffusion imaging by FT-FRAP was demonstrated as a method for mapping diffusion properties across a FOV. Diffusion images can be generated by leveraging the information about image contrast contained in spatial frequency domain peaks. The local contribution to each spatial frequency domain peak can be obtained through centering and inverse Fourier transformation of the peak. Finally, fitting to a model recovers local diffusion properties for each pixel or segment of an image.

Future work includes implementation of these techniques in new application spaces, including measurement of mobility in pharmaceutically relevant matrices, quantification of protein aggregation, characterization of gels, and live-cell imaging. Future algorithm development includes quantification of diffusion during photobleaching, and the extension of FT-FRAP to different photobleaching patterns.

## 9. STOCHASTIC DSC BY NONLINEAR OPTICAL MICROSCOPY

Though not directly related to FT-FRAP, this chapter describes a project completed early in the doctoral work of the author and is included in this thesis to highlight the full body of work completed throughout the Ph.D. of the author.

### 9.1 Abstract

Stochastic phase transformations within individual crystalline particles were recorded by integration of second harmonic generation (SHG) imaging with differential scanning calorimetry (DSC). The SHG-activity of a crystal is highly sensitive to the specific molecular packing arrangement within a noncentrosymmetric lattice, providing access to information otherwise unavailable by conventional imaging approaches. Consequently, lattice transformations associated with dehydration/desolvation events were readily observed by SHG imaging and directly correlated to the phase transformations detected by the DSC measurements. Following studies of a model system (urea), stochastic differential scanning calorimetry (SDSC) was performed on trehalose dihydrate, which has a more complex phase behavior. From these measurements, SDSC revealed a broad diversity of single-particle thermal trajectories and direct evidence of a “cold phase transformation” process not observable by the DSC measurements alone.

### 9.2 Background

In pharmaceutical drug development, drug substances and formulations with long-term physical and chemical stability ensure full optimized of a drug when administered to the patient. During the time consuming process of formulations development (estimated  $> 3$  months and \$1 million) it is thus critical to employ methods that inform on possible avenues of reduced bioavailability.<sup>[79]</sup> Identifying possible failure points early can reduce the chances of late-stage failure, which can be costly and time consuming to remediate. For active pharmaceutical ingredients administered as crystalline formulations, phase transitions to al-

ternate crystal forms can have deleterious effects on aqueous dissolution rates, affecting both oral and parenteral bioavailability.[80]–[82] Administering these drugs as amorphous solid dispersions or as liquid formulations does not altogether avoid the problem, as spontaneous crystallization can occur during storage or even *in vivo* under certain conditions.[83]–[89] Phase transitions can dictate both direct physical depletion of bioavailable drugs through transitions to low solubility crystal forms, as well as susceptibility to chemical depletion through transitions to more reactive crystalline, liquid or glassy states. There is therefore a need in the pharmaceutical industry to thoroughly map the phase space of potential drug candidates, excipients, and mixtures. Several thermal methods exist for characterizing phase transitions within pharmaceutical powders. Differential thermal analysis applies equal heat to reference and sample pans and measures the temperature differential between the two pans to detect thermal events associated with phase transitions. Thermal gravimetric analysis (TGA) continuously measures the mass of a sample while varying temperature. TGA is especially useful for dehydration and decomposition. Differential scanning calorimetry (DSC) enables the detection of phase transitions as a function of the energy differential between reference and sample pans heated to the same temperature. DSC is a widely used technique for phase transition characterization because of its sensitivity, ease-of-use, and short measurement time.[90]

Despite these advantages, DSC probes the energy transfer into the full ensemble of the sample, averaging over all particles in the formulation. Phase transitions for ensembles of crystals are predicted to be stochastic, with nucleation typically being the rate-limiting step on a per-particle basis.[91]–[93] If phase transformation is stochastic, individual transient events may be obscured or missed in ensemble-averaged analysis. Additionally, single-particle measurements can enable the accurate modelling of kinetics for phase transitions, allowing the distinction between different mechanisms of transition (i.e., concerted or continuous).[94]

Optical microscopy measurements of changes in gross morphology coupled with DSC can recover information on single-particle phase transformations. Reading and coworkers have developed an image analysis algorithm dubbed thermal analysis by structural characterization (TASC) to detect phase transitions and the spatial distribution of phases from images acquired using hot-stage microscopy.[95]–[99] TASC measures the subtle difference



between an original image and subsequent images to quantify morphological changes within a region-of-interest as temperature is varied. The algorithm also accounts for the possibility of translation of the region-of-interest within the field-of-view (FOV). TASC is a fast and inexpensive method for characterizing the spatial distribution of phase transformations. However, TASC methods rely exclusively on morphological changes in the optical response, which are only intrinsically related to a subset of all possible phase transformations. Solid / solid phase transformations are largely inaccessible by TASC, and glass / solid phase transformations can be challenging to reliably detect without perturbing the sample. Desolvation (including dehydration) or polymorph transitions in the solid state are typically not accompanied by obvious changes in the gross morphology of a particle but can profoundly influence physico-chemical characteristics that are accompanied by thermal transients in DSC measurements. In addition, structural rearrangements between polymorphs with similar bulk free energies are quite challenging to detect by either conventional DSC or bright-field microscopy. Coupling DSC with concurrent imaging capabilities that are more directly tied to crystal form would help address these ambiguities associated with conventional bright-field microscopy and DSC.

In this work, we demonstrated the integration of second harmonic generation (SHG) microscopy with DSC analysis to monitor phase transitions on a per-particle basis. This multimodal approach enabled simultaneous single-particle analysis for distinguishing the impact of crystal size and shape on phase transitions in a single experiment, complementing the ensemble-averaged information obtained from DSC. Furthermore, the strict symmetry requirements for SHG allow the mapping of complex desolvation and crystal form transitions with sensitivity in the ppm regime.<sup>[100]</sup> Previous work has utilized the exquisite sensitivity of SHG microscopy to internal structure of the lattice in non-centrosymmetric crystals as a standalone tool for polymorph discrimination, calibration-free quantification of trace crystallinity, and protein crystal centering at X-ray beamlines.<sup>[101]–[103]</sup> Raman spectroscopy, terahertz spectroscopy, and SHG have all previously been used to characterize crystallinity, polymorphism, and phase transitions.<sup>[104]–[111]</sup> Herein, aspects of the complex phase behavior of trehalose dihydrate are elucidated through the integration of simultaneous SHG and DSC measurements.

### 9.3 Methods

SDSC was implemented using the scientific apparatus, experiments measurements, data analysis methods, and sample preparation procedures described herein.

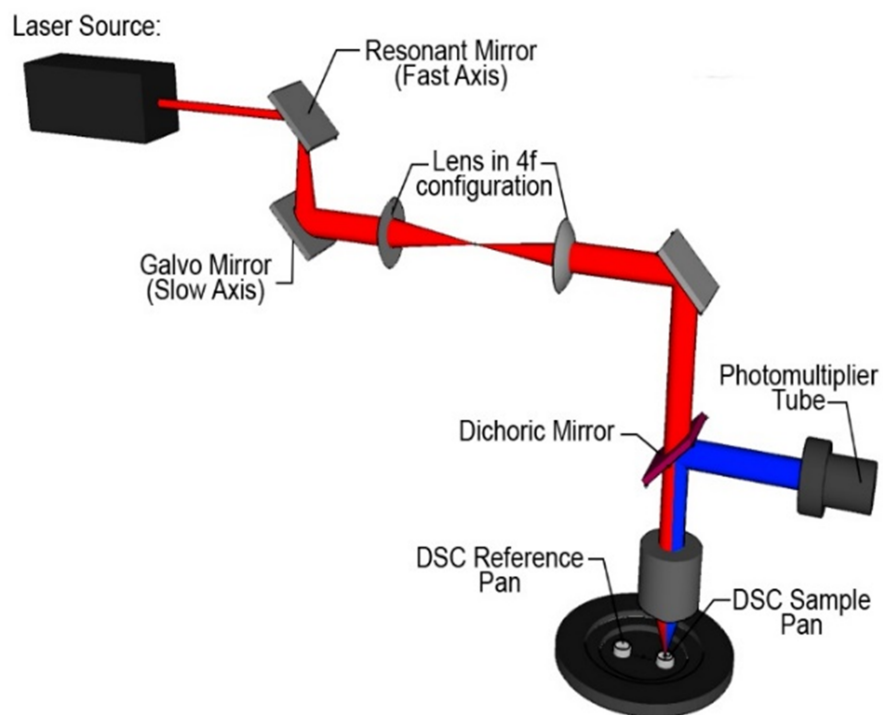


**Figure 9.1.** Schematic of the integrated SHG-DSC microscope. A pulsed laser beam (800 nm, 80 MHz) was scanned with a galvo-resonant scan pair, which was  $4f$  coupled to the back of an objective and focused onto a DSC sample pan. The SHG signal was collected in the epi direction, isolated with a dichroic mirror and detected with a photomultiplier tube.

#### 9.3.1 SHG microscopy

The experimental apparatus is depicted in Figure 9.1 and consists of an SHG microscope built in-house integrated with an optical DSC stage (Linkam, DSC450). A tunable 80 MHz, Ti:sapphire, femtosecond laser (Spectra-Physics, Mai Tai) was used for the incident

light source. The fundamental beam was raster-scanned across the sample using a resonant scanning mirror at 8.8 kHz (EOPC) for the fast-scan axis and a galvanometer mirror (Cambridge-Tech) for the slow-scan axis. A 4x, 0.1 NA objective (Nikon) was used to focus the beam onto the sample, and the SHG signal was collected in the epi direction through the same objective used for delivery of the fundamental beam. The laser was tuned to 800 nm with a power of 80–120 mW at the sample. Two long-pass dichroic mirrors (Chroma, 650DCXR) and a band-pass filter (Chroma HQ400/20M-2P) were used to isolate the 400 nm SHG signal before it was detected by a photomultiplier tube (PMT) (Hamamatsu, H7422P-40 MOD). Responses of the PMT were digitized synchronously with the laser pulses by using a digital oscilloscope card (Alazar Tech, ATS9350) and mapped onto  $512 \times 512$  images via custom software written in-house (MATLAB).<sup>[112]</sup> The SHG videos were recorded at 17 frames per second for urea samples and at eight frames per second for trehalose samples.

### 9.3.2 DSC measurements

Stochastic differential scanning calorimetry (SDSC) measurements were acquired by integration of the SHG microscope with a Linkam Optical DSC450 stage. The DSC temperature ramp range was 125–145 °C for the urea samples and 80–250 °C for the trehalose samples with ramp rates of 10 °C/min and 20 °C/min, respectively. Before the data collection, an isothermal hold time of two minutes for both urea and trehalose ensured a reliable starting temperature for all experiments to reduce the effects of initial temperature variation. Temperature and input power were measured by the DSC at a rate of five Hz. Standard aluminum sample pans were used in all DSC experiments, and were not sealed to allow for optical access of the sample. The DSC was calibrated using an indium standard in an open pan.

### 9.3.3 Data analysis

ImageJ (NIH) was used to perform single-particle analysis on the images acquired with the integrated SHG-DSC microscope. The single-particle SHG areas were measured by calculating the fraction of pixels above a threshold within the region of interest.

### 9.3.4 Sample preparation

Supersaturated solutions of urea (Sigma-Aldrich) were prepared in DI water and rapidly recrystallized in an ice bath. The water was decanted, and the crystals were left to dry overnight. Crystals were then passed through a 63  $\mu\text{m}$  mesh into the aluminum DSC sample pan. D-(+)-trehalose dihydrate (Sigma Life Sciences) was added to a DSC pan as-received.

## 9.4 Results and Discussion

SDSC was applied to study the phase transformations of urea and trehalose samples. Additionally, the impulse response function (IRF) of the DSC instrument was determined using data collected by SDSC.

### 9.4.1 SDSC of urea crystals

Initial proof of concept studies for SDSC were performed using urea, which undergoes a simple, single-stage, solid/liquid phase transformation. Figure 9.2A shows the DSC trace for the melting transition of a urea sample (black line) overlaid with vertical lines corresponding to the normalized SHG areas of individual particles dropping below a threshold of 10% (view Figure 9.3 for the overlay of the DSC trace and the full traces of the normalized SHG areas of each particle).

The DSC trace indicates that the melting transition occurred at  $\sim 135$  °C. This temperature is slightly higher than the literature value of 133 °C. This difference is attributed to a non-negligible heat transfer time to the sample. The need for optical access required the use of an unencapsulated sample pan, resulting in slower heat transfer.[113] Despite some baseline drift in the per-particle SHG activity from particle motion, the single-particle SHG area shows much sharper transitions from the SHG-active crystalline form to the SHG-inactive molten liquid of urea indicated by the DSC trace, consistent with independent, stochastic melting events. Single-particle analysis yields a mean phase transition duration of  $1.0 \pm 0.6$  s/particle while the DSC melting peak has a full-width-half-maximum of 3.3 s. This difference indicates that the rate of phase transformation was dictated largely by the rate for

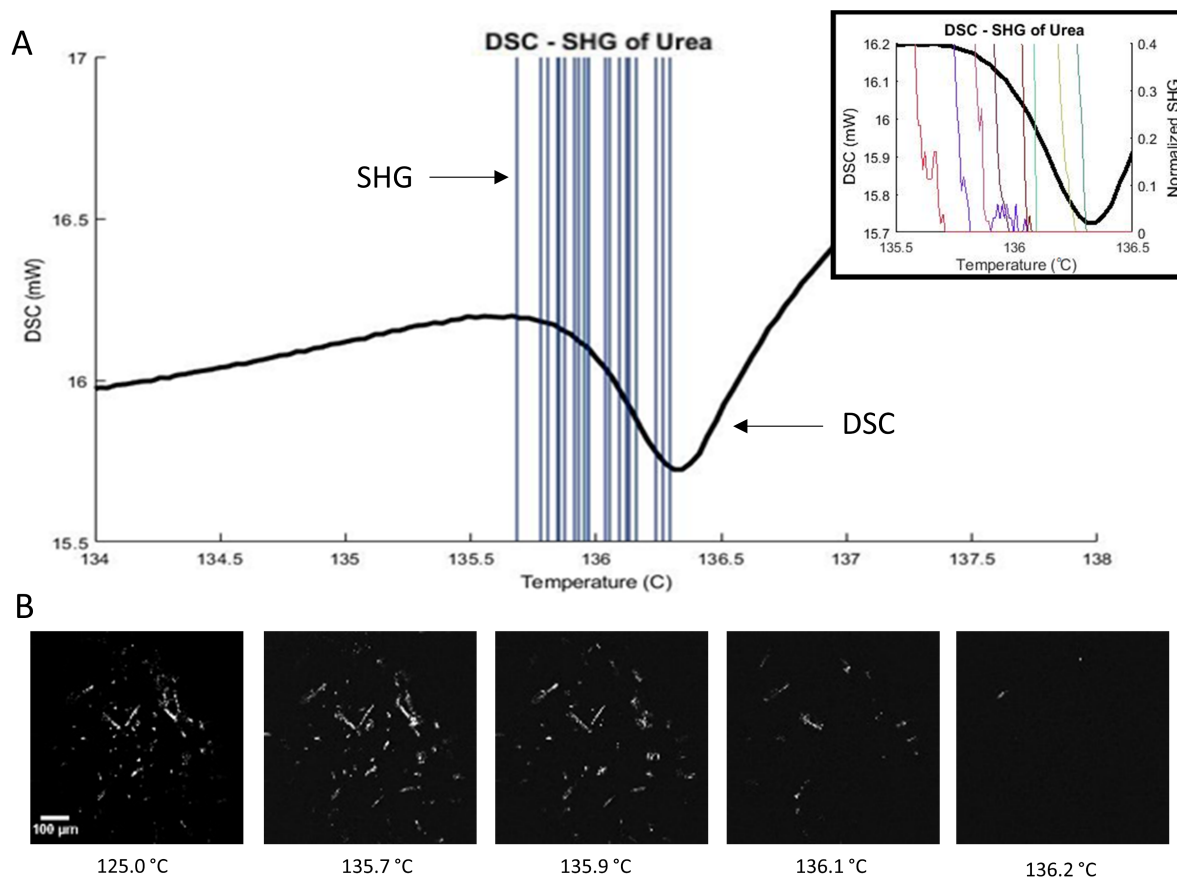


**Figure 9.2.** A) SDSC analysis of urea by combined SHG microscopy and DSC. The solid black line is the DSC trace of the melting of urea with endothermic direction being down (left-axis). The vertical colored lines show the temperatures in which the normalized SHG intensity of individual urea particles (acquired concurrently with DSC measurements) drops below a value of 0.1. DSC and SHG measurements both indicate a structural transformation in the same temperature range. The inset shows a zoom-in of the temperature range 135.5–136.5 °C where the color lines correspond to the normalized SHG intensity of individual urea particles. B) SHG microscope images of urea crystals during SDSCS analysis. SHG microscopy reveals the stochastic nature of the melting transition and enables analysis on a per-particle basis.

seed formation of the liquid-state within individual particles, followed by rapid phase transformation within a given particle. Figure 9.2B shows representative frames from a video acquired with the SHG microscope during the melting of urea. From the SHG results, the nucleation rate at the phase transformation temperature can be estimated. In this work,

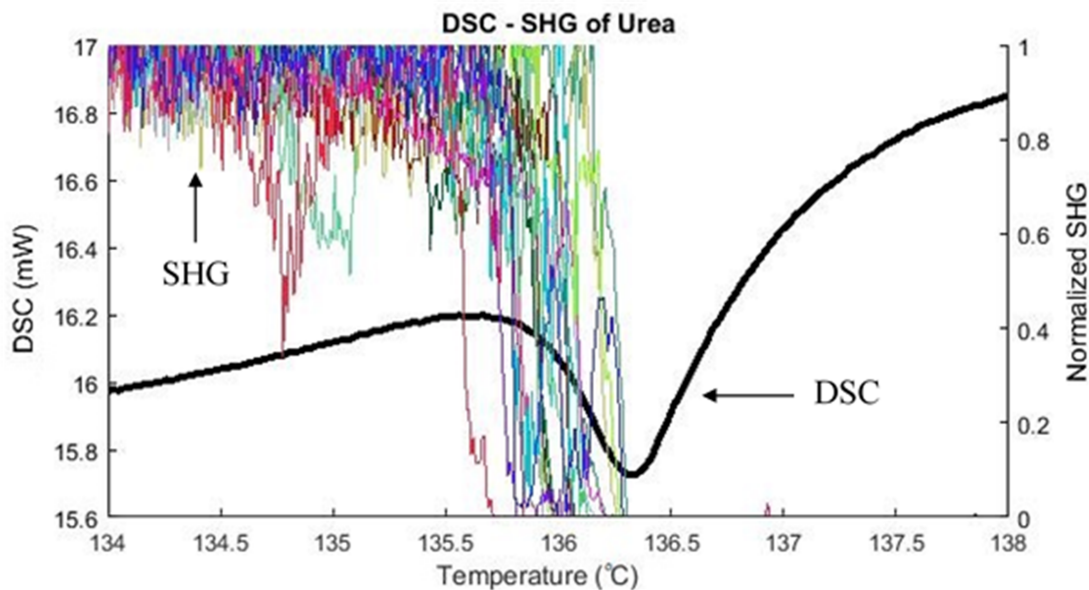


**Figure 9.3.** SDSC analysis of urea by combined SHG microscopy and DSC. The solid black line is the DSC trace of the melting of urea with endothermic direction being down (left-axis). The thin colored lines show the normalized SHG intensity of individual urea particles (right-axis), acquired concurrently with DSC measurements. DSC and SHG measurements both indicate a structural transformation in the same temperature range.

a nucleation event is defined as the phase transformation of a single crystal (in this case, from solid to liquid). Nucleation rates were determined from the loss rate of SHG-active particles, measured as the intensity of each crystal decreased below a threshold (close to zero). Approximations for the per-particle mass using the density of urea and volume estimated from particle cross-sectional area yield a peak nucleation rate of  $1.6 \pm 0.2 \times 10^4$  nuclei per s per mg (based on the observed rate of 6.13 nuclei/s in a FOV with an estimated  $0.39 \mu\text{g}$  of particulate mass; standard deviation was determined based on Poisson statistics for the number of crystals within the FOV). See Figure 9.4 for the distribution of crystal volumes and a description of the use of Poisson statistics for obtaining the uncertainty in the nucleation rate

Consistent with numerous previous DSC studies of powders, SDSC measurements were performed exclusively as the temperature was increased to interrogate phase transformations.[114], [115] While in principle, additional information can be obtained from mea-

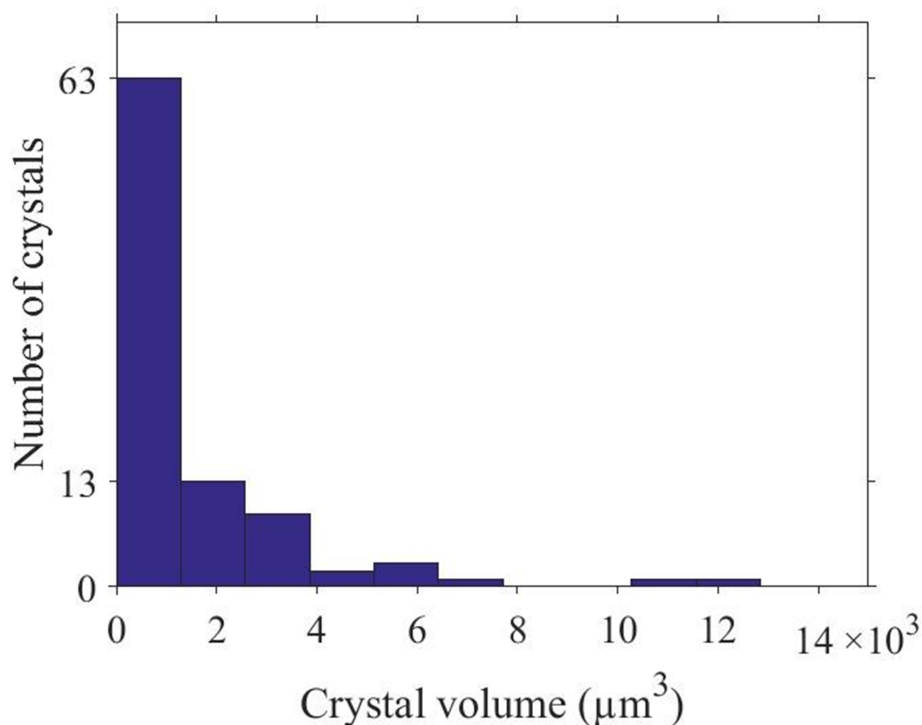


**Figure 9.4.** Distribution of urea crystal volumes. The estimated volume of the crystals was calculated from the crystal cross-sectional area (assuming rod-like shape). A total mass of  $0.39 \mu\text{g}$  was calculated from the sum of these volumes multiplied by the density of urea ( $1.32 \text{ g/cm}^3$ ). The mass combined with the observed nucleation rate of  $6.13 \text{ nuclei/s}$  yields the nucleation rate of  $1.6 \pm 0.2 \times 10^4 \text{ nuclei per second per milligram}$ .

measurements of thermal events upon cooling, the phase transformations induced by heating were generally not easily reversible (e.g., dehydration). Even in the absence of composition changes, melting of many individual isolated particles results in coalescence to a homogeneous melt, while the reverse process will not recover isolated crystalline particles upon cooling. Furthermore, SDSC measurements upon cooling are complicated in practice by wicking of the liquid, which moves much of the sample out of the field of view. Although not the focus of the present study, it is worth noting that SHG microscopy has a rich history of informing on crystallization kinetics in accelerated stability assessments for active pharmaceutical ingredients.<sup>[116]</sup>

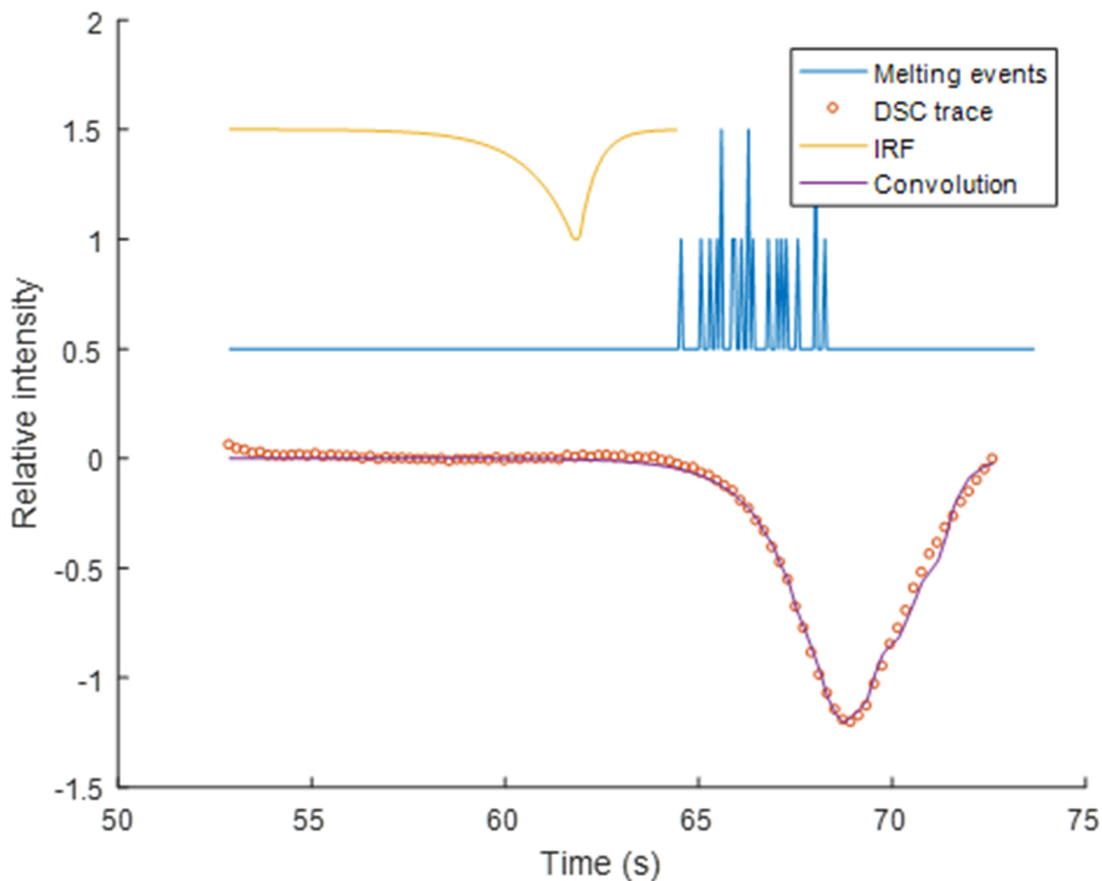


**Figure 9.5.** Comparison of the experimental DSC trace and the DSC trace generated from melting events. The best-fit double-exponential IRF (yellow) is convolved with impulsive melting events (blue) of single-particles observed in SHG images to generate the purple trace, which is in good agreement with the experimental DSC data (red). The time constant and offset of double-exponential IRF were optimized to minimize difference between experimental and generated DSC traces. Best-fit values of  $1.161 \pm 0.019$  s,  $0.435 \pm 0.013$  s, and  $3.088 \pm 0.013$  s were computed for the double-exponential time constants and the offset respectively.

#### 9.4.2 IRF determination with SDSC

The simultaneous SHG measurements were also used to determine the impulse response function (IRF) of the DSC instrument. As described in a preceding paragraph, the thermal events induced in the sample produced an instrument response with a temporal delay associated with heat transfer times. The macroscopic DSC endotherm arose from the net



collective contributions from many such stochastic events. As such, the DSC observables were given by the convolution of the impulsive phase transformations with the IRF of the DSC system. Assuming a double-exponential IRF consistent with heat flow through a thermal resistor, the measured set of impulsive phase transformations by SHG  $x$  can be combined with the recorded DSC trace  $y$  to recover the maximum likelihood estimate (MLE) for the impulse response function  $\hat{f}_{IRF} = f_{IRF}(\hat{a})$  described by the set of parameters  $a$  through  $\hat{a} = \arg \min_a ||y - x \otimes f_{IRF}(a)||^2$ . The results of an MLE fit of the measured DSC transient using the single-crystal phase transformation data from SHG is shown in Figure 9.5, recovering a phase-lag of  $3.088 \pm 0.013$  s and rising and falling exponential time constants of  $1.161 \pm 0.019$  s and  $0.435 \pm 0.013$  s, respectively, for the double-exponential IRF. The phase-lag between the DSC event and the mean of the SHG events is attributed to delays from diffusive heat transfer from the individual particles to the pan and sample mount of the DSC instrument. The two time constants are tentatively attributed to the thermal diffusion times from the sample to the sample stage, and from the stage to the heat sink.[117] Even in a relatively simple melting transition, SHG provides the capability of mapping phase transformations on individual particles with temporal resolution much faster than achievable from conventional ensemble-averaged DSC measurements. The pairing of both methods provides information inaccessible by DSC alone; namely, that phase transformation proceeds through slow nucleation followed by rapid growth on a per particle basis with an intrinsic rate of  $1.0 \pm 0.6$  s/particle (variance is dominated by particle-to-particle stochasticity).

### 9.4.3 SDSC of trehalose dihydrate crystals

The performance of SDSC using the integrated SHG-DSC microscope was further tested with trehalose dihydrate, a molecule with complex phase behavior, including the existence of multiple transient crystal forms accessible under varying conditions.[118]–[121] Since significant differences in crystal structure can exist between polymorphs, hydrates, and solvates, SHG has the potential to aid in distinguishing transitions due to its sensitivity to non-centrosymmetric crystal forms.[101] Figure 9.6 summarizes the SDSC analysis of trehalose dihydrate. Each colored line represents the percentage of pixels in an individual trehalose

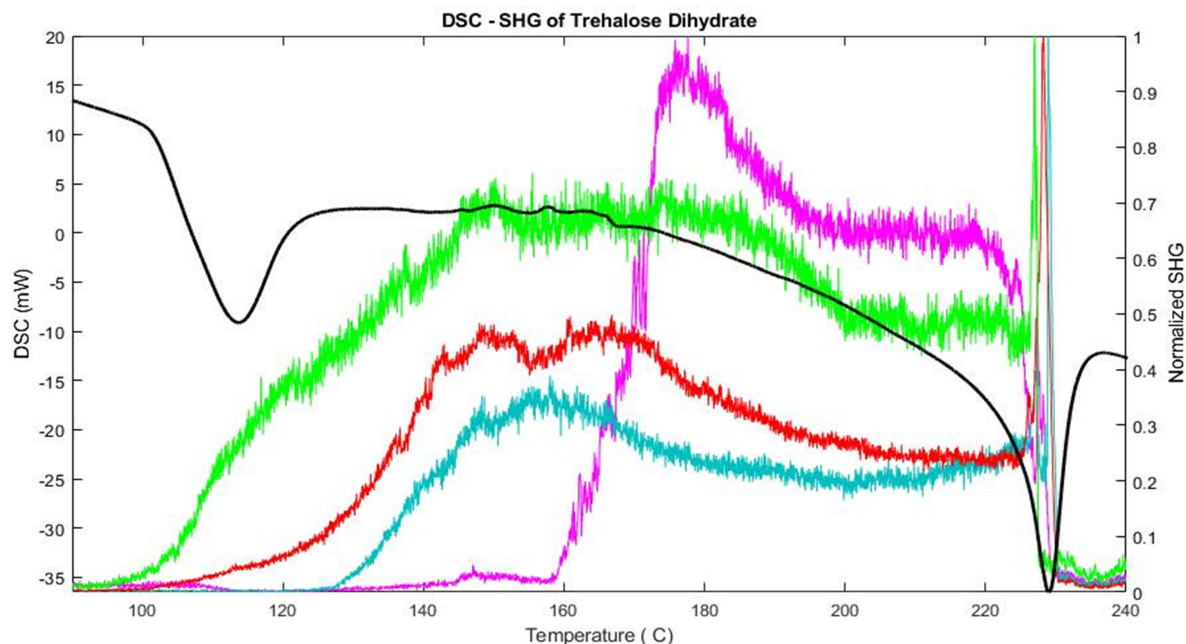


**Figure 9.6.** SDSC analysis of trehalose by SHG microscopy. The colored lines show the percentage of pixels in a trehalose particle above an SHG intensity threshold overlaid with the black line of the DSC trace with the endothermic direction being down. SDSC images were summed for the temperature range of 140–220 °C and the logarithm of the summed image was cropped to the measured region of each particle (each cropped image points to the representative SHG trace).

crystalline particle that exceeds a threshold. Four individual particles were monitored in this study. The black line is the DSC curve, in which dips correspond to endothermic events. For the temperature range of 140–220 °C, the collected SDSC images were summed and the logarithm of this summed image was cropped to the measured region of each particle.

DSC and SHG data were interpreted using previously reported literature values to map the polymorphic transitions of the sample through the temperature ramp. At the initial 80 °C, the weak SHG signal arises from the trehalose dihydrate ( $T_h$ ) form that was initially added to the DSC pan before the temperature ramp.<sup>[122]</sup> The composition of this starting material was confirmed by powder X-ray diffraction (pXRD) to be primarily composed  $T_h$ , although the unstable anhydrous form ( $T_\alpha$ ) may also be present at trace levels; previous reports indicate observation of the  $T_\alpha$  form following room temperature storage at low rel-

active humidity.[122], [123] The first signs of phase transformation activity occurred in the temperature range of 80–130 °C. The DSC curve exhibited a major endothermic peak in this range. This peak was previously reported to be the result of the dehydration of  $T_h$ . [114] Additionally, two distinct trends appear in the individual particle SHG data. Three of the trehalose particles increased in SHG activity while the other particle decreased over this same lower temperature range. The disparity in SHG activity between individual particles can be explained by the two major dehydration pathways available for  $T_h$  in this temperature range;  $T_h$  can either partially dehydrate with rearrangement to the crystalline  $T_\gamma$  form or completely dehydrate to an amorphous form ( $T_{am}$ ). [114], [122] Similarly, the  $T_\alpha$  form can also transition to the  $T_{am}$  form upon heating. [114], [115], [122], [123] The  $T_\gamma$  polymorph is theorized to be a mixture of  $T_h$  encapsulated in a shell of the crystalline, anhydrous form ( $T_\beta$ ), which is SHG-active. [114], [123] Therefore, we conclude that the three particles that increased in SHG area in this temperature range likely transitioned to the SHG-active  $T_\gamma$  form, while the particle that reduced in SHG activity likely transitioned to the SHG-inactive  $T_{am}$  form at  $\sim 110$  °C from either the  $T_h$  or  $T_\alpha$  form.

The SHG activity generally increased for individual particles over the subsequent temperature range of 130–160 °C. The DSC curve exhibited small but reproducible features in this temperature range, the magnitude of which varied between experiments, and has been reported to be due to the dehydration of  $T_h$ . [114] Measurements of the fraction of SHG-active pixels in individual particles show that the three particles that previously exhibited SHG signal continue to convert over this temperature range. This increase in highly SHG-active fraction can simply be attributed to  $T_\beta$  crystal growth over this temperature range. The fourth particle that previously decreased in SHG area shows a sharp increase in SHG area starting at  $\sim 160$  °C. SHG-inactive  $T_{am}$  has been previously reported to transition to SHG-active  $T_\beta$  in the range of 150–200 °C. [114], [122] Likewise, the  $T_\alpha$  form has been reported to be able to transition directly to the  $T_\beta$  when held at a temperature of  $\sim 150$  °C. [114], [115], [122], [123] However, this  $T_\alpha$  transition has not been observed with the faster heating rates (20 °C/min.) used in the present study. Therefore, we conclude that this polymorphic transition from  $T_{am}$  to  $T_\beta$  is likely the cause of the sharp peak in SHG from the particle represented by the magenta trace.

Following the monotonic increases in transitioning to the  $T_\beta$  form from 130–160 °C, decreases in SHG were observed for all four particles in the range 160–200 °C. No peaks are observed in the DSC curve in this range, but the trehalose particles exhibit slowly varying and inhomogeneous loss in SHG activity. Several possible mechanisms for this loss in SHG activity were considered, two of which are described in detail. One possible explanation for loss in SHG activity with large crystal-to-crystal variability may be from interference effects as crystal sizes change during phase transformation.[124] Interference fringes from single crystals were reported previously in SHG microscopy measurements. However, interference effects were deemed unlikely for three reasons: i) interference effects would be anticipated to produce increases or decreases in SHG activity with equal probability, while only decays were observed experimentally, ii) the backwards coherence length is short ( $\sim 100$  nm) relative to the sizes of the crystals, such that average activities would be expected, and iii) the interference is expected to vary with thickness, such that crystals with variance in dimensions would likely produce fringes over which the intensities are integrated. Alternatively, the decay in SHG signal can be explained by condensation of water vapor released by  $T_h$  onto the optical window of the DSC. Condensation was commonly seen in our experiments when working with hydrated samples because open crucible pans were used in the experiment to allow for imaging during DSC scans. Additionally, no purge gas was used to remove water vapor from the system, as addition of purge gas introduced measurement variance in the DSC analyses from variable heat transfer to the bath gas. Previously reported results by TGA indicate gradual water loss up to 200 °C, consistent with the observed reduction in SHG signal that is proposed to arise from scattering losses from condensation.[114] Furthermore, condensation is likely to impact some locations within the FOV to a greater extent than others, potentially providing an explanation for the large crystal-to-crystal variability in the loss. Thus, condensation is concluded to be the main cause of this loss in SHG signal.

Following the slow SHG signal loss from condensation, dramatic changes in the SHG-activity arose from 200–240 °C. In this range the DSC curve exhibited an endothermic peak at  $\sim 230$  °C, and the SHG data displayed a sharp increase and subsequent decrease during the DSC peak. It is clear from the literature that the endothermic DSC peak arises from a melting transition.[114], [123] The final fall in SHG area is attributed to this melting

event. However, the source of the sharp increase in SHG area prior to the melt has no precedent in reported DSC measurements. Two origins for the transient SHG area increase were considered.

First, significant mobility in the sample arose during the melting transition, which could alter the positions of the sample crystals relative to the focal plane. Crystals moving into the focal plane could result in an increase in SHG area, as SHG intensity scales with the squared intensity of incident light. Second, the increase could be explained by a change in the crystal form, degree of crystallinity, or crystal size of trehalose. To evaluate the first mechanism, a custom optic, designed in-house, was added to the beam path to extend the depth-of-field from  $\sim 20 \mu\text{m}$  to  $\sim 100 \mu\text{m}$ .<sup>[125]</sup> The sharp peak in SHG prior to the melt was still observed while imaging with an extended depth-of-field, suggesting that crystal movement into the focal volume is not likely to be the major cause of the increase in SHG area.

Alternatively, the increase in SHG area could arise from a change in the crystal form, degree of crystallinity, or crystal size of trehalose. While it is possible that there exists a previously unknown polymorphic transition immediately prior to the melt of trehalose, this possibility was rejected on the principal of Occam’s razor, in light of the extensive body of prior work done to characterize the polymorphism of trehalose. A more plausible origin for the spike in SHG area is from the final conversion of the remaining  $T_h$  core of  $T_\gamma$  polymorph to  $T_\beta$ , promoted by an increase in the energy in molecular diffusion immediately prior to the melting transition. Additionally, another closely related contribution to the increase in SHG area could be the rapid growth of  $T_\beta$  crystalline domains of trehalose from residual  $T_{am}$  due to increase mobility immediately prior to the melt. In summary, the particles observed in this study are theorized to undergo one of two general phase transition pathways:  $T_h \rightarrow T_{am} \rightarrow T_\beta \rightarrow \text{melt}$  or  $T_h \rightarrow T_\gamma \rightarrow T_\beta \rightarrow \text{melt}$ .

Notably, this “cold phase transformation” phenomenon, in which phase transformation to the SHG-active crystalline form occurs immediately prior to the transition to the liquid form, was clearly observable by SHG but undetectable in the DSC measurements. This latter proposed mechanism has precedent in observations of “cold crystallization” in DSC, in which transient crystallization arises upon transformation from a glassy state to a liquid.<sup>[126]</sup> In DSC, cold crystallization appears as an exothermic peak immediately preceding an endother-

mic peak. Cold crystallization has been observed in studies of  $T_h$  for the transition from a glassy material to the  $T_\beta$  form.[123] However, to our knowledge, this study represents the first observation of cold transformation between two different solid-state crystalline forms prior to the melt. Importantly, evidence supporting cold transformation was undetectable by DSC alone, presumably obfuscated by the comparatively longer response time and inherent ensemble averaging associated with the DSC measurements.

As discussed before, the reversibility of the SDSC was not investigated for trehalose dihydrate. Like the urea samples, wetting of the sample pan after heating of the sample presented challenges in maintaining sample position within the field of view following the melt. Likewise, reversibility after dehydration ( $< 220$  °C) would not be anticipated due to the large entropic barriers involved with rehydration of the sample under high humidity. Studies have shown that the dehydrated sample can rehydrate to the original material, but over timescales significantly longer than easily accessible by DSC.[127], [128]

Analysis of the impulse response function from urea provides a route for connecting the cold phase transformation and melting processes to the DSC endotherm at  $\sim 230$  °C. The entire transformation to produce the SHG-active crystal form, followed by melting progressed all within  $\sim 2$  seconds, likely explaining the absence of prior work describing cold phase transformation. Figure 9.7 shows the results of the convolution of the IRF determined from the urea analysis, with impulses corresponding to either the initial rise from the “cold phase transformation” or the melt. Neither of the resulting curves coincides directly with that of the DSC melting peak. This disparity likely arises from the statistics of small numbers, as only four particles in the FOV were available for analysis (as opposed to 58 crystals for urea).

Differences between single-particle and ensemble-averaged measurements are particularly noteworthy in the results shown in Figure 9.6. The integrated SHG intensity from one particular crystal indicated by the green trace nicely tracks the DSC trace and is likely to be representative of the major ensemble-averaged thermal event at  $\sim 110$  °C. However, it is clear that distinctly different phase transformation behaviors are observed within a subset of the population, exemplified by the red, cyan, and purple traces. This apparent incongruency is attributed to the stochastic nature of the sample, with multiple thermally accessible transformation pathways available.

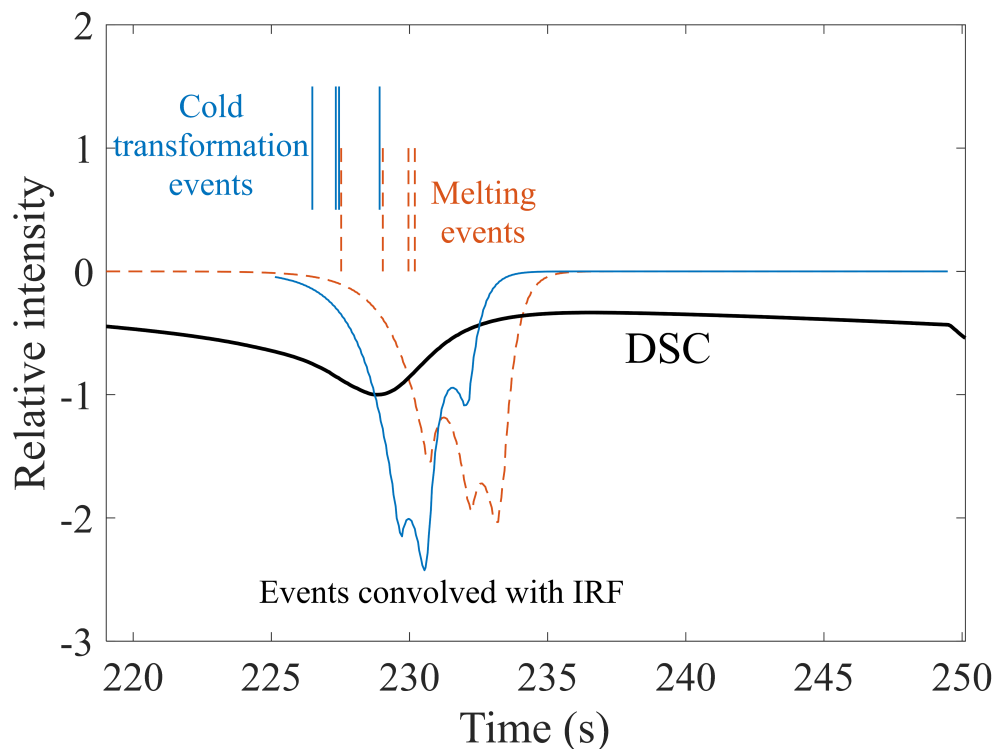


**Figure 9.7.** IRF analysis of trehalose dihydrate. The final DSC peak in the trehalose dihydrate experiment was analyzed using the IRF recovered from the urea experiment (see Fig. 9.5). The “cold phase transformation” events and the melting events of the four particles were convolved with the best-fit, double-exponential IRF determined from analysis of SDSC data for urea. The results of the convolution are shown as colored curves. Neither the cold phase transformation events nor the melting events produced curves that matched well with the DSC peak. This perhaps indicates that the four particles observed using SHG microscopy are not representative of the full population of particles in the sample. A more complete set of phase transformation events would possibly produce a curve that would better match the DSC peak.

Trehalose dihydrate has multiple competing pathways to various crystal forms, which are stochastically accessed over large temperature ranges and which are likely to produce significantly different heats of phase transformation. This rich landscape of crystal form space is largely obscured by ensemble-averaged measurements of DSC alone, but is clearly accessed by per-particle analysis using SHG microscopy.

## 9.5 Conclusions

SDSC was shown to enable connection of internal structural rearrangements within crystalline materials measured by SHG on single particles to the heat flow recorded by DSC. SHG measurements were sensitive to variations in the molecular packing arrangements during the phase transitions of individual particles that are generally inaccessible in conventional microscopy. Coupling the structural data acquired from SHG imaging with DSC enabled single-particle measurements disentangled from the ensemble-averaged thermal transients recorded with DSC. A proof-of-concept SDSC experiment was performed on urea, which has a single solid/liquid phase transformation. From these measurements, the IRF of the DSC system was determined, showing that the melt proceeds through a slow nucleation step followed by rapid growth on a per particle basis. Next, SDSC was used to characterize the phase behavior of a more complex system, trehalose dihydrate. The dehydration events of trehalose dihydrate were readily observed by SDSC and the higher temporal resolution of SHG measurements, compared to that of the temporal resolution of typical DSC measurements, allowed for detection of a rapid phase transformation not observable by DSC. Thus, SDSC is proposed as a novel technique for the pharmaceutical drug development pipeline for the characterization of single-particle phase transformations.



## REFERENCES

- [1] M. C. Catley, J. Coote, M. Bari, and K. L. Tomlinson, "Monoclonal antibodies for the treatment of asthma," *Pharmacology Therapeutics*, vol. 132, no. 3, pp. 333–351, 2011, ISSN: 0163-7258. DOI: <https://doi.org/10.1016/j.pharmthera.2011.09.005>. [Online]. Available: <http://www.sciencedirect.com/science/article/pii/S0163725811001835>.
- [2] L. Bossaller and A. Rothe, "Monoclonal antibody treatments for rheumatoid arthritis," *Expert Opinion on Biological Therapy*, vol. 13, no. 9, pp. 1257–1272, 2013, ISSN: 1471-2598. DOI: [10.1517/14712598.2013.811230](https://doi.org/10.1517/14712598.2013.811230). [Online]. Available: <https://doi.org/10.1517/14712598.2013.811230>.
- [3] D. M. Ecker, S. D. Jones, and H. L. Levine, "The therapeutic monoclonal antibody market," *mAbs*, vol. 7, no. 1, pp. 9–14, 2015, ISSN: 1942-0862. DOI: [10.4161/19420862.2015.989042](https://doi.org/10.4161/19420862.2015.989042). [Online]. Available: <https://doi.org/10.4161/19420862.2015.989042>.
- [4] M. R. Turner and S. V. Balu-Iyer, "Challenges and opportunities for the subcutaneous delivery of therapeutic proteins," *Journal of Pharmaceutical Sciences*, vol. 107, no. 5, pp. 1247–1260, 2018, ISSN: 0022-3549. DOI: <https://doi.org/10.1016/j.xphs.2018.01.007>. [Online]. Available: <http://www.sciencedirect.com/science/article/pii/S0022354918300078>.
- [5] N. Varkhede and L. Forrest, "Understanding the monoclonal antibody disposition after subcutaneous administration using a minimal physiologically based pharmacokinetic model," *Journal of pharmacy pharmaceutical sciences : a publication of the Canadian Society for Pharmaceutical Sciences, Societe canadienne des sciences pharmaceutiques*, vol. 21, no. 1s, 130s–148s, 2018, ISSN: 1482-1826. DOI: [10.18433/jpps30028](https://doi.org/10.18433/jpps30028). [Online]. Available: <https://pubmed.ncbi.nlm.nih.gov/30011390%20https://www.ncbi.nlm.nih.gov/pmc/articles/PMC6613546/>.
- [6] M. A. Steller, R. J. Parker, D. G. Covell, O. D. Holton, A. M. Keenan, S. M. Sieber, and J. N. Weinstein, "Optimization of monoclonal antibody delivery via the lymphatics: the dose dependence," *Cancer Research*, vol. 46, no. 4 Part 1, p. 1830, 1986. [Online]. Available: [http://cancerres.aacrjournals.org/content/46/4\\_Part\\_1/1830.abstract](http://cancerres.aacrjournals.org/content/46/4_Part_1/1830.abstract).
- [7] H. M. Kinnunen, V. Sharma, L. R. Contreras-Rojas, Y. Yu, C. Alleman, A. Sreedhara, S. Fischer, L. Khawli, S. T. Yohe, D. Bumbaca, T. W. Patapoff, A. L. Daugherty, and R. J. Mersy, "A novel in vitro method to model the fate of subcutaneously administered biopharmaceuticals and associated formulation components," *Journal of Controlled Release*, vol. 214, pp. 94–102, 2015, ISSN: 0168-3659. DOI: <https://doi.org/10.1016/j.jconrel.2015.07.016>. [Online]. Available: <http://www.sciencedirect.com/science/article/pii/S0168365915300298>.

- [8] H. M. Kinnunen and R. J. Mersny, "Improving the outcomes of biopharmaceutical delivery via the subcutaneous route by understanding the chemical, physical and physiological properties of the subcutaneous injection site," *Journal of Controlled Release*, vol. 182, pp. 22–32, 2014, ISSN: 0168-3659. DOI: <https://doi.org/10.1016/j.jconrel.2014.03.011>. [Online]. Available: <http://www.sciencedirect.com/science/article/pii/S016836591400145X>.
- [9] T. H. Scheuermann, S. B. Padrick, K. H. Gardner, and C. A. Brautigam, "On the acquisition and analysis of microscale thermophoresis data," *Analytical Biochemistry*, vol. 496, pp. 79–93, 2016, ISSN: 0003-2697. DOI: <https://doi.org/10.1016/j.ab.2015.12.013>. [Online]. Available: <http://www.sciencedirect.com/science/article/pii/S0003269715005758>.
- [10] J. Liu, J. D. Andya, and S. J. Shire, "A critical review of analytical ultracentrifugation and field flow fractionation methods for measuring protein aggregation," *The AAPS Journal*, vol. 8, no. 3, E580–E589, 2006, ISSN: 1550-7416. DOI: [10.1208/aapsj080367](https://doi.org/10.1208/aapsj080367). [Online]. Available: <https://doi.org/10.1208/aapsj080367>.
- [11] R. T. Wright, D. Hayes, P. J. Sherwood, W. F. Stafford, and J. J. Correia, "Auc measurements of diffusion coefficients of monoclonal antibodies in the presence of human serum proteins," *European Biophysics Journal*, vol. 47, no. 7, pp. 709–722, 2018, ISSN: 1432-1017. DOI: [10.1007/s00249-018-1319-x](https://doi.org/10.1007/s00249-018-1319-x). [Online]. Available: <https://doi.org/10.1007/s00249-018-1319-x>.
- [12] M. V. Ivanov, M. R. Talipov, and Q. K. Timerghazin, "Genetic algorithm optimization of point charges in force field development: Challenges and insights," *The Journal of Physical Chemistry A*, vol. 119, no. 8, pp. 1422–1434, 2015, ISSN: 1089-5639. DOI: [10.1021/acs.jpca.5b00218](https://doi.org/10.1021/acs.jpca.5b00218). [Online]. Available: <https://doi.org/10.1021/acs.jpca.5b00218>.
- [13] J. P. Gabrielson, M. L. Brader, A. H. Pekar, K. B. Mathis, G. Winter, J. F. Carpenter, and T. W. Randolph, "Quantitation of aggregate levels in a recombinant humanized monoclonal antibody formulation by size-exclusion chromatography, asymmetrical flow field flow fractionation, and sedimentation velocity," *J Pharm Sci*, vol. 96, no. 2, pp. 268–79, 2007, ISSN: 0022-3549 (Print) 0022-3549. DOI: [10.1002/jps.20760](https://doi.org/10.1002/jps.20760).
- [14] U. Nöbbmann, M. Connah, B. Fish, P. Varley, C. Gee, S. Mulot, J. Chen, L. Zhou, Y. Lu, F. Sheng, J. Yi, and S. E. Harding, "Dynamic light scattering as a relative tool for assessing the molecular integrity and stability of monoclonal antibodies," *Biotechnology and Genetic Engineering Reviews*, vol. 24, no. 1, pp. 117–128, 2007, ISSN: 0264-8725. DOI: [10.1080/02648725.2007.10648095](https://doi.org/10.1080/02648725.2007.10648095). [Online]. Available: <https://doi.org/10.1080/02648725.2007.10648095>.

- [15] V. I. Razinkov, M. J. Treuheit, and G. W. Becker, “Accelerated formulation development of monoclonal antibodies (mabs) and mab-based modalities: Review of methods and tools,” *Journal of Biomolecular Screening*, vol. 20, no. 4, pp. 468–483, 2015, ISSN: 1087-0571. DOI: [10.1177/1087057114565593](https://doi.org/10.1177/1087057114565593). [Online]. Available: <https://doi.org/10.1177/1087057114565593>.
- [16] H. Ruf, “Data accuracy and resolution in particle sizing by dynamic light scattering,” *Advances in Colloid and Interface Science*, vol. 46, pp. 333–342, 1993, ISSN: 0001-8686. DOI: [https://doi.org/10.1016/0001-8686\(93\)80047-F](https://doi.org/10.1016/0001-8686(93)80047-F). [Online]. Available: <http://www.sciencedirect.com/science/article/pii/000186869380047F>.
- [17] M. Asmari, R. Ratih, H. A. Alhazmi, and S. El Deeb, “Thermophoresis for characterizing biomolecular interaction,” *Methods*, vol. 146, pp. 107–119, 2018, ISSN: 1046-2023. DOI: <https://doi.org/10.1016/j.ymeth.2018.02.003>. [Online]. Available: <http://www.sciencedirect.com/science/article/pii/S1046202317304267>.
- [18] N. Loren, J. Hagman, J. K. Jonasson, H. Deschout, D. Bernin, F. Cella-Zanacchi, A. Diaspro, J. G. McNally, M. Ameloot, N. Smisdom, M. Nyden, A. M. Hermansson, M. Rudemo, and K. Braeckmans, “Fluorescence recovery after photobleaching in material and life sciences: Putting theory into practice,” *Quarterly Reviews of Biophysics*, vol. 48, no. 3, pp. 323–387, 2015, ISSN: 0033-5835. DOI: [10.1017/s0033583515000013](https://doi.org/10.1017/s0033583515000013).
- [19] E. A. J. Reits and J. J. Neefjes, “From fixed to frap: Measuring protein mobility and activity in living cells,” *Nature Cell Biology*, vol. 3, no. 6, E145–E147, 2001, ISSN: 1465-7392. DOI: [10.1038/35078615](https://doi.org/10.1038/35078615).
- [20] R. Peters, J. Peters, K. H. Tews, and W. Bähr, “A microfluorimetric study of translational diffusion in erythrocyte membranes,” *BBA - Biomembranes*, vol. 367, no. 3, pp. 282–294, 1974, ISSN: 0005-2736. DOI: [10.1016/0005-2736\(74\)90085-6](https://doi.org/10.1016/0005-2736(74)90085-6).
- [21] G. Vámosi, E. Friedländer-Brock, S. M. Ibrahim, R. Brock, J. Szöllösi, and G. Vereb, “Egf receptor stalls upon activation as evidenced by complementary fluorescence correlation spectroscopy and fluorescence recovery after photobleaching measurements,” *International Journal of Molecular Sciences*, vol. 20, no. 13, p. 3370, 2019. DOI: [10.3390/ijms20133370](https://doi.org/10.3390/ijms20133370).
- [22] G. L. Weiss, A. K. Kieninger, I. Maldener, K. Forchhammer, and M. Pilhofer, “Structure and function of a bacterial gap junction analog,” *Cell*, vol. 178, no. 2, pp. 374–+, 2019, ISSN: 0092-8674. DOI: [10.1016/j.cell.2019.05.055](https://doi.org/10.1016/j.cell.2019.05.055).
- [23] M. J. Frojd and K. Flardh, “Apical assemblies of intermediate filament-like protein filp are highly dynamic and affect polar growth determinant diviva in streptomyces venezuelae,” *Molecular Microbiology*, vol. 112, no. 1, pp. 47–61, 2019, ISSN: 0950-382X. DOI: [10.1111/mmi.14253](https://doi.org/10.1111/mmi.14253).

- [24] W. M. Babinchak and W. K. Surewicz, "Studying protein aggregation in the context of liquid-liquid phase separation using fluorescence and atomic force microscopy, fluorescence and turbidity assays, and frap," *Bio-Protocol*, vol. 10, no. 2, p. 14, 2020. DOI: [10.21769/BioProtoc.3489](https://doi.org/10.21769/BioProtoc.3489). [Online]. Available: [%3CGo%20to%20ISI%3E://WOS:000547506600004](https://www.ncbi.nlm.nih.gov/pmc/articles/PMC7506600/).
- [25] G. S. Offeddu, L. Mohee, and R. E. Cameron, "Scale and structure dependent solute diffusivity within microporous tissue engineering scaffolds," *Journal of Materials Science-Materials in Medicine*, vol. 31, no. 5, p. 11, 2020, ISSN: 0957-4530. DOI: [10.1007/s10856-020-06381-x](https://doi.org/10.1007/s10856-020-06381-x). [Online]. Available: [%3CGo%20to%20ISI%3E://WOS:000533303100003](https://www.ncbi.nlm.nih.gov/pmc/articles/PMC7333031/).
- [26] K. Hashlamoun, Z. Abusara, A. Ramirez-Torres, A. Grillo, W. Herzog, and S. Federico, "Fluorescence recovery after photobleaching: Direct measurement of diffusion anisotropy," *Biomechanics and Modeling in Mechanobiology*, p. 16, ISSN: 1617-7959. DOI: [10.1007/s10237-020-01346-z](https://doi.org/10.1007/s10237-020-01346-z). [Online]. Available: [%3CGo%20to%20ISI%3E://WOS:000543634100002](https://www.ncbi.nlm.nih.gov/pmc/articles/PMC7543634/).
- [27] E. Verheyen, S. van der Wal, H. Deschout, K. Braeckmans, S. de Smedt, A. Barendregt, W. E. Hennink, and C. F. van Nostrum, "Protein macromonomers containing reduction-sensitive linkers for covalent immobilization and glutathione triggered release from dextran hydrogels," *Journal of Controlled Release*, vol. 156, no. 3, pp. 329–336, 2011, ISSN: 0168-3659. DOI: [10.1016/j.jconrel.2011.08.040](https://doi.org/10.1016/j.jconrel.2011.08.040).
- [28] M. C. Branco, D. J. Pochan, N. J. Wagner, and J. P. Schneider, "Macromolecular diffusion and release from self-assembled beta-hairpin peptide hydrogels," *Biomaterials*, vol. 30, no. 7, pp. 1339–1347, 2009, ISSN: 0142-9612. DOI: [10.1016/j.biomaterials.2008.11.019](https://doi.org/10.1016/j.biomaterials.2008.11.019).
- [29] F. Alvarez-Mancenido, K. Braeckmans, S. C. De Smedt, J. Demeester, M. Landin, and R. Martinez-Pacheco, "Characterization of diffusion of macromolecules in konjac glucomannan solutions and gels by fluorescence recovery after photobleaching technique," *International Journal of Pharmaceutics*, vol. 316, no. 1-2, pp. 37–46, 2006, ISSN: 0378-5173. DOI: [10.1016/j.ijpharm.2006.02.029](https://doi.org/10.1016/j.ijpharm.2006.02.029).
- [30] K. B. Kosto and W. M. Deen, "Diffusivities of macromolecules in composite hydrogels," *Aiche Journal*, vol. 50, no. 11, pp. 2648–2658, 2004, ISSN: 0001-1541. DOI: [10.1002/aic.10216](https://doi.org/10.1002/aic.10216).
- [31] L. Peeters, N. N. Sanders, K. Braeckmans, K. Boussery, J. Van de Voorde, S. C. De Smedt, and J. Demeester, "Vitreous: A barrier to nonviral ocular gene therapy," *Investigative Ophthalmology Visual Science*, vol. 46, no. 10, pp. 3553–3561, 2005, ISSN: 0146-0404. DOI: [10.1167/iovs.05-0165](https://doi.org/10.1167/iovs.05-0165).

- [32] K. Remaut, N. N. Sanders, B. G. De Geest, K. Braeckmans, J. Demeester, and S. C. De Smedt, "Nucleic acid delivery: Where material sciences and bio-sciences meet," *Materials Science Engineering R-Reports*, vol. 58, no. 3-5, pp. 117–161, 2007, ISSN: 0927-796X. DOI: [10.1016/j.mser.2007.06.001](https://doi.org/10.1016/j.mser.2007.06.001).
- [33] V. Cherezov, J. Liu, M. Griffith, M. A. Hanson, and R. C. Stevens, "Lcp-frap assay for pre-screening membrane proteins for in meso crystallization," *Crystal Growth Design*, vol. 8, no. 12, pp. 4307–4315, 2008, ISSN: 1528-7483. DOI: [10.1021/cg800778j](https://doi.org/10.1021/cg800778j).
- [34] J. S. Joseph, W. Liu, J. Kunken, T. M. Weiss, H. Tsuruta, and V. Cherezov, "Characterization of lipid matrices for membrane protein crystallization by high-throughput small angle x-ray scattering," *Methods*, vol. 55, no. 4, pp. 342–349, 2011, ISSN: 1046-2023. DOI: [10.1016/j.ymeth.2011.08.013](https://doi.org/10.1016/j.ymeth.2011.08.013).
- [35] F. Xu, W. Liu, M. A. Hanson, R. C. Stevens, and V. Cherezov, "Development of an automated high throughput lcp-frap assay to guide membrane protein crystallization in lipid mesophases," *Crystal Growth Design*, vol. 11, no. 4, pp. 1193–1201, 2011, ISSN: 1528-7483. DOI: [10.1021/cg101385e](https://doi.org/10.1021/cg101385e).
- [36] E. Chun, A. A. Thompson, W. Liu, C. B. Roth, M. T. Griffith, V. Katritch, J. Kunken, F. Xu, V. Cherezov, M. A. Hanson, and R. C. Stevens, "Fusion partner toolchest for the stabilization and crystallization of g protein-coupled receptors," *Structure*, vol. 20, no. 6, pp. 967–976, 2012, ISSN: 0969-2126. DOI: [10.1016/j.str.2012.04.010](https://doi.org/10.1016/j.str.2012.04.010).
- [37] D. Mazza, F. Cella, G. Vicidomini, S. Krol, and A. Diaspro, "Role of three-dimensional bleach distribution in confocal and two-photon fluorescence recovery after photobleaching experiments," *Applied Optics*, vol. 46, no. 30, pp. 7401–7411, 2007, ISSN: 1559-128X. DOI: [10.1364/ao.46.007401](https://doi.org/10.1364/ao.46.007401).
- [38] H. Deschout, J. Hagman, S. Fransson, J. Jonasson, M. Rudemo, N. Loren, and K. Braeckmans, "Straightforward frap for quantitative diffusion measurements with a laser scanning microscope," *Optics Express*, vol. 18, no. 22, pp. 22 886–22 905, 2010, ISSN: 1094-4087. DOI: [10.1364/oe.18.022886](https://doi.org/10.1364/oe.18.022886).
- [39] K. Braeckmans, B. G. Stubbe, K. Remaut, J. Demeester, and S. C. De Smedt, "Anomalous photobleaching in fluorescence recovery after photobleaching measurements due to excitation saturation- a case study for fluorescein," *Journal of Biomedical Optics*, vol. 11, no. 4, p. 13, 2006, ISSN: 1083-3668. DOI: [10.1117/1.2337531](https://doi.org/10.1117/1.2337531).
- [40] K. Braeckmans, L. Peeters, N. N. Sanders, S. C. De Smedt, and J. Demeester, "Three-dimensional fluorescence recovery after photobleaching with the confocal scanning laser microscope," *Biophysical Journal*, vol. 85, no. 4, pp. 2240–2252, 2003, ISSN: 0006-3495. DOI: [10.1016/s0006-3495\(03\)74649-9](https://doi.org/10.1016/s0006-3495(03)74649-9).

- [41] K. Braeckmans, K. Remaut, R. E. Vandenbroucke, B. Lucas, S. C. De Smedt, and J. Demeester, "Line frap with the confocal laser scanning microscope for diffusion measurements in small regions of 3-d samples," *Biophysical journal*, vol. 92, no. 6, pp. 2172–2183, 2007, ISSN: 0006-3495.
- [42] S. K. Davis and C. J. Bardeen, "Using two-photon standing waves and patterned photobleaching to measure diffusion from nanometers to microns in biological systems," *Review of Scientific Instruments*, vol. 73, no. 5, pp. 2128–2135, 2002, ISSN: 0034-6748. DOI: [10.1063/1.1464656](https://doi.org/10.1063/1.1464656).
- [43] B. A. Smith and H. M. McConnell, "Determination of molecular-motion in membranes using periodic pattern photobleaching," *Proceedings of the National Academy of Sciences of the United States of America*, vol. 75, no. 6, pp. 2759–2763, 1978, ISSN: 0027-8424. DOI: [10.1073/pnas.75.6.2759](https://doi.org/10.1073/pnas.75.6.2759).
- [44] J. Davoust, P. F. Devaux, and L. Leger, "Fringe pattern photobleaching, a new method for the measurement of transport-coefficients of biological macromolecules," *Embo Journal*, vol. 1, no. 10, pp. 1233–1238, 1982, ISSN: 0261-4189. DOI: [10.1002/j.1460-2075.1982.tb00018.x](https://doi.org/10.1002/j.1460-2075.1982.tb00018.x).
- [45] B. Wehrle-Haller, "Analysis of integrin dynamics by fluorescence recovery after photobleaching," in *Adhesion Protein Protocols*. Springer, 2007, pp. 173–201.
- [46] D. A. Stavreva and J. G. McNally, "Fluorescence recovery after photobleaching (frap) methods for visualizing protein dynamics in living mammalian cell nuclei," *Chromatin and Chromatin Remodeling Enzymes, Pt A*, vol. 375, pp. 443–455, 2004, ISSN: 0076-6879. [Online]. Available: [3CGo%20to%20ISI%3E://WOS:000189397900027](https://www.ncbi.nlm.nih.gov/pubmed/15333333).
- [47] K. Braeckmans, L. Peeters, N. N. Sanders, S. C. De Smedt, and J. Demeester, "Three-dimensional fluorescence recovery after photobleaching with the confocal scanning laser microscope," *Biophysical Journal*, vol. 85, no. 4, pp. 2240–2252, 2003, ISSN: 0006-3495. DOI: [10.1016/s0006-3495\(03\)74649-9](https://doi.org/10.1016/s0006-3495(03)74649-9). [Online]. Available: [3CGo%20to%20ISI%3E://WOS:000185575400015](https://www.ncbi.nlm.nih.gov/pubmed/12744444).
- [48] K. Braeckmans, K. Remaut, R. E. Vandenbroucke, B. Lucas, S. C. De Smedt, and J. Demeester, "Line frap with the confocal laser scanning microscope for diffusion measurements in small regions of 3-d samples," *Biophysical journal*, vol. 92, no. 6, pp. 2172–2183, 2007, ISSN: 0006-3495.
- [49] S. K. Davis and C. J. Bardeen, "Using two-photon standing waves and patterned photobleaching to measure diffusion from nanometers to microns in biological systems," *Review of Scientific Instruments*, vol. 73, no. 5, pp. 2128–2135, 2002, ISSN: 0034-6748. DOI: [10.1063/1.1464656](https://doi.org/10.1063/1.1464656). [Online]. Available: [3CGo%20to%20ISI%3E://WOS:000175194200024](https://www.ncbi.nlm.nih.gov/pubmed/12000024).



- [50] B. A. Smith and H. M. McConnell, "Determination of molecular-motion in membranes using periodic pattern photobleaching," *Proceedings of the National Academy of Sciences of the United States of America*, vol. 75, no. 6, pp. 2759–2763, 1978, ISSN: 0027-8424. DOI: [10.1073/pnas.75.6.2759](https://doi.org/10.1073/pnas.75.6.2759). [Online]. Available: [%3CGo%20to%20ISI%3E://WOS:A1978FF05900049](https://www.ncbi.nlm.nih.gov/pmc/articles/PMC3300049/).
- [51] J. Davoust, P. F. Devaux, and L. Leger, "Fringe pattern photobleaching, a new method for the measurement of transport-coefficients of biological macromolecules," *Embo Journal*, vol. 1, no. 10, pp. 1233–1238, 1982, ISSN: 0261-4189. DOI: [10.1002/j.1460-2075.1982.tb00018.x](https://doi.org/10.1002/j.1460-2075.1982.tb00018.x). [Online]. Available: [%3CGo%20to%20ISI%3E://WOS:A1982PR04000014](https://www.ncbi.nlm.nih.gov/pmc/articles/PMC3300014/).
- [52] G. M. Hagen, W. Caarls, K. A. Lidke, A. H. B. De Vries, C. Fritsch, B. G. Barisas, D. J. Arndt-Jovin, and T. M. Jovin, "Fluorescence recovery after photobleaching and photoconversion in multiple arbitrary regions of interest using a programmable array microscope," *Microscopy Research and Technique*, vol. 72, no. 6, pp. 431–440, 2009, ISSN: 1059-910X. DOI: [10.1002/jemt.20686](https://doi.org/10.1002/jemt.20686). [Online]. Available: [%3CGo%20to%20ISI%3E://WOS:000267099100003](https://www.ncbi.nlm.nih.gov/pmc/articles/PMC267099100003/).
- [53] C. M. Hobson, E. T. O'Brien, M. R. Falvo, and R. Superfine, "Combined selective plane illumination microscopy and frap maps intranuclear diffusion of nls-gfp," *Biophysical Journal*, vol. 119, no. 3, pp. 514–524, 2020, ISSN: 0006-3495. DOI: [10.1016/j.bpj.2020.07.001](https://doi.org/10.1016/j.bpj.2020.07.001). [Online]. Available: [%3CGo%20to%20ISI%3E://WOS:000557759900005](https://www.ncbi.nlm.nih.gov/pmc/articles/PMC557759900005/).
- [54] B. Liu, C. M. Hobson, F. M. Pimenta, E. Nelsen, J. Hsiao, T. O'Brien, M. R. Falvo, K. M. Hahn, and R. Superfine, "View-mod: A versatile illumination engine with a modular optical design for fluorescence microscopy," *Optics Express*, vol. 27, no. 14, pp. 19 950–19 972, 2019, ISSN: 1094-4087. DOI: [10.1364/oe.27.019950](https://doi.org/10.1364/oe.27.019950). [Online]. Available: [%3CGo%20to%20ISI%3E://WOS:000474429600077](https://www.ncbi.nlm.nih.gov/pmc/articles/PMC600077/).
- [55] D. A. Berk, F. Yuan, M. Leunig, and R. K. Jain, "Fluorescence photobleaching with spatial fourier-analysis - measurement of diffusion in light-scattering media," *Biophysical Journal*, vol. 65, no. 6, pp. 2428–2436, 1993, ISSN: 0006-3495. DOI: [10.1016/s0006-3495\(93\)81326-2](https://doi.org/10.1016/s0006-3495(93)81326-2).
- [56] T. K. L. Meyvis, S. C. De Smedt, P. Van Oostveldt, and J. Demeester, "Fluorescence recovery after photobleaching: A versatile tool for mobility and interaction measurements in pharmaceutical research," *Pharmaceutical Research*, vol. 16, no. 8, pp. 1153–1162, 1999, ISSN: 0724-8741. DOI: [10.1023/a:1011924909138](https://doi.org/10.1023/a:1011924909138).

- [57] C. C. Shi, J. Kuo, P. D. Bell, and H. Yao, “Anisotropic solute diffusion tensor in porcine tmj discs measured by frap with spatial fourier analysis,” *Annals of Biomedical Engineering*, vol. 38, no. 11, pp. 3398–3408, 2010, ISSN: 0090-6964. DOI: [10.1007/s10439-010-0099-y](https://doi.org/10.1007/s10439-010-0099-y).
- [58] T. T. Tsay and K. A. Jacobson, “Spatial fourier-analysis of video photobleaching measurements - principles and optimization,” *Biophysical Journal*, vol. 60, no. 2, pp. 360–368, 1991, ISSN: 0006-3495. DOI: [10.1016/s0006-3495\(91\)82061-6](https://doi.org/10.1016/s0006-3495(91)82061-6).
- [59] R. Metzler and J. Klafter, “The random walk’s guide to anomalous diffusion: A fractional dynamics approach,” *Physics Reports-Review Section of Physics Letters*, vol. 339, no. 1, pp. 1–77, 2000, ISSN: 0370-1573. DOI: [10.1016/s0370-1573\(00\)00070-3](https://doi.org/10.1016/s0370-1573(00)00070-3).
- [60] J. Klafter, A. Blumen, and M. F. Shlesinger, “Stochastic pathway to anomalous diffusion,” *Physical Review A*, vol. 35, no. 7, pp. 3081–3085, 1987, ISSN: 2469-9926. DOI: [10.1103/PhysRevA.35.3081](https://doi.org/10.1103/PhysRevA.35.3081).
- [61] M. Wachsmuth, W. Waldeck, and J. Langowski, “Anomalous diffusion of fluorescent probes inside living cell nuclei investigated by spatially-resolved fluorescence correlation spectroscopy,” *Journal of Molecular Biology*, vol. 298, no. 4, pp. 677–689, 2000, ISSN: 0022-2836. DOI: [10.1006/jmbi.2000.3692](https://doi.org/10.1006/jmbi.2000.3692).
- [62] I. Y. Wong, M. L. Gardel, D. R. Reichman, E. R. Weeks, M. T. Valentine, A. R. Bausch, and D. A. Weitz, “Anomalous diffusion probes microstructure dynamics of entangled f-actin networks,” *Physical Review Letters*, vol. 92, no. 17, p. 4, 2004, ISSN: 0031-9007. DOI: [10.1103/PhysRevLett.92.178101](https://doi.org/10.1103/PhysRevLett.92.178101).
- [63] D. S. Banks and C. Fradin, “Anomalous diffusion of proteins due to molecular crowding,” *Biophysical Journal*, vol. 89, no. 5, pp. 2960–2971, 2005, ISSN: 0006-3495. DOI: [10.1529/biophysj.104.051078](https://doi.org/10.1529/biophysj.104.051078).
- [64] I. M. Tolic-Norrelykke, E. L. Munteanu, G. Thon, L. Oddershede, and K. Berg-Sorensen, “Anomalous diffusion in living yeast cells,” *Physical Review Letters*, vol. 93, no. 7, p. 4, 2004, ISSN: 0031-9007. DOI: [10.1103/PhysRevLett.93.078102](https://doi.org/10.1103/PhysRevLett.93.078102).
- [65] M. K. Daddysman and C. J. Fecko, “Revisiting point frap to quantitatively characterize anomalous diffusion in live cells,” *Journal of Physical Chemistry B*, vol. 117, no. 5, pp. 1241–1251, 2013, ISSN: 1520-6106. DOI: [10.1021/jp310348s](https://doi.org/10.1021/jp310348s).
- [66] K. G. Heinze, S. Costantino, P. De Koninck, and P. W. Wiseman, “Beyond photobleaching, laser illumination unbinds fluorescent proteins,” *The Journal of Physical Chemistry B*, vol. 113, no. 15, pp. 5225–5233, 2009, ISSN: 1520-6106.



- [67] P. Wedekind, U. Kubitscheck, and R. Peters, “Scanning microphotolysis - a new photobleaching technique based on fast intensity modulation of a scanned laser-beam and confocal imaging,” *Journal of Microscopy-Oxford*, vol. 176, pp. 23–33, 1994, ISSN: 0022-2720. DOI: [10.1111/j.1365-2818.1994.tb03496.x](https://doi.org/10.1111/j.1365-2818.1994.tb03496.x).
- [68] D. Blumenthal, L. Goldstien, M. Edidin, and L. A. Gheber, “Universal approach to frap analysis of arbitrary bleaching patterns,” *Scientific Reports*, vol. 5, 2015, ISSN: 2045-2322. DOI: [10.1038/srep11655](https://doi.org/10.1038/srep11655).
- [69] P. Wedekind, U. Kubitscheck, O. Heinrich, and R. Peters, “Line-scanning microphotolysis for diffraction-limited measurements of lateral diffusion,” *Biophysical Journal*, vol. 71, no. 3, pp. 1621–1632, 1996, ISSN: 0006-3495. DOI: [10.1016/s0006-3495\(96\)79366-9](https://doi.org/10.1016/s0006-3495(96)79366-9).
- [70] F. Lanni and B. R. Ware, “Modulation detection of fluorescence photobleaching recovery,” *Review of Scientific Instruments*, vol. 53, no. 6, pp. 905–908, 1982, ISSN: 0034-6748. DOI: [10.1063/1.1137078](https://doi.org/10.1063/1.1137078).
- [71] I. M. Sokolov, “Models of anomalous diffusion in crowded environments,” *Soft Matter*, vol. 8, no. 35, pp. 9043–9052, 2012.
- [72] J.-P. Bouchaud and A. Georges, “Anomalous diffusion in disordered media: Statistical mechanisms, models and physical applications,” *Physics reports*, vol. 195, no. 4-5, pp. 127–293, 1990, ISSN: 0370-1573.
- [73] H. Sun, W. Chen, and Y. Chen, “Variable-order fractional differential operators in anomalous diffusion modeling,” *Physica A: Statistical Mechanics and its Applications*, vol. 388, no. 21, pp. 4586–4592, 2009, ISSN: 0378-4371.
- [74] W. Chen, H. Sun, X. Zhang, and D. Korošak, “Anomalous diffusion modeling by fractal and fractional derivatives,” *Computers Mathematics with Applications*, vol. 59, no. 5, pp. 1754–1758, 2010, ISSN: 0898-1221.
- [75] M. J. Saxton, “Anomalous diffusion due to obstacles - a monte-carlo study,” *Biophysical Journal*, vol. 66, no. 2, pp. 394–401, 1994, ISSN: 0006-3495. DOI: [10.1016/s0006-3495\(94\)80789-1](https://doi.org/10.1016/s0006-3495(94)80789-1).
- [76] R. N. Bracewell and R. N. Bracewell, *The Fourier transform and its applications*. McGraw-Hill New York, 1986, vol. 31999.
- [77] A. vanderSchaaf and J. H. vanHateren, “Modelling the power spectra of natural images: Statistics and information,” *Vision Research*, vol. 36, no. 17, pp. 2759–2770, 1996, ISSN: 0042-6989. DOI: [10.1016/0042-6989\(96\)00002-8](https://doi.org/10.1016/0042-6989(96)00002-8).

- [78] R. Garrappa, "Numerical evaluation of two and three parameter mittag-leffler functions," *Siam Journal on Numerical Analysis*, vol. 53, no. 3, pp. 1350–1369, 2015, ISSN: 0036-1429. DOI: [10.1137/140971191](https://doi.org/10.1137/140971191).
- [79] J. Strovel, S. Sittampalam, N. P. Coussens, M. Hughes, J. Inglese, A. Kurtz, A. Andalibi, L. Patton, C. Austin, and M. Baltezor, "Early drug discovery and development guidelines: For academic researchers, collaborators, and start-up companies," 2016.
- [80] M. L. Cheney, N. Shan, E. R. Healey, M. Hanna, L. Wojtas, M. J. Zaworotko, V. Sava, S. Song, and J. R. Sanchez-Ramos, "Effects of crystal form on solubility and pharmacokinetics: A crystal engineering case study of lamotrigine," *Crystal Growth Design*, vol. 10, no. 1, pp. 394–405, 2009, ISSN: 1528-7483.
- [81] D. Maddileti, B. Swapna, and A. Nangia, "High solubility crystalline pharmaceutical forms of blonanserin," *Crystal Growth Design*, vol. 14, no. 5, pp. 2557–2570, 2014, ISSN: 1528-7483.
- [82] A. Yadav, A. Shete, A. Dabke, P. Kulkarni, and S. Sakhare, "Co-crystals: A novel approach to modify physicochemical properties of active pharmaceutical ingredients," *Indian journal of pharmaceutical sciences*, vol. 71, no. 4, p. 359, 2009.
- [83] A. Newman, G. Knipp, and G. Zografi, "Assessing the performance of amorphous solid dispersions," *Journal of pharmaceutical sciences*, vol. 101, no. 4, pp. 1355–1377, 2012, ISSN: 0022-3549.
- [84] S. Baghel, H. Cathcart, and N. J. O'Reilly, "Polymeric amorphous solid dispersions: A review of amorphization, crystallization, stabilization, solid-state characterization, and aqueous solubilization of biopharmaceutical classification system class ii drugs," *Journal of pharmaceutical sciences*, vol. 105, no. 9, pp. 2527–2544, 2016, ISSN: 0022-3549.
- [85] M. J. Jackson, U. S. Kestur, M. A. Hussain, and L. S. Taylor, "Dissolution of danazol amorphous solid dispersions: Supersaturation and phase behavior as a function of drug loading and polymer type," *Molecular pharmaceuticals*, vol. 13, no. 1, pp. 223–231, 2015, ISSN: 1543-8384.
- [86] H. Konno and L. S. Taylor, "Ability of different polymers to inhibit the crystallization of amorphous felodipine in the presence of moisture," *Pharmaceutical research*, vol. 25, no. 4, pp. 969–978, 2008, ISSN: 0724-8741.
- [87] S. L. Shamblin and G. Zografi, "The effects of absorbed water on the properties of amorphous mixtures containing sucrose," *Pharmaceutical research*, vol. 16, no. 7, pp. 1119–1124, 1999, ISSN: 0724-8741.

- [88] V. Andronis, M. Yoshioka, and G. Zografi, “Effects of sorbed water on the crystallization of indomethacin from the amorphous state,” *Journal of pharmaceutical sciences*, vol. 86, no. 3, pp. 346–351, 1997, ISSN: 0022-3549.
- [89] A. C. Rumondor, L. A. Stanford, and L. S. Taylor, “Effects of polymer type and storage relative humidity on the kinetics of felodipine crystallization from amorphous solid dispersions,” *Pharmaceutical research*, vol. 26, no. 12, p. 2599, 2009, ISSN: 0724-8741.
- [90] S.-D. Clas, C. R. Dalton, and B. C. Hancock, “Differential scanning calorimetry: Applications in drug development,” *Pharmaceutical science technology today*, vol. 2, no. 8, pp. 311–320, 1999, ISSN: 1461-5347.
- [91] D. W. Oxtoby, “Nucleation of first-order phase transitions,” *Accounts of chemical research*, vol. 31, no. 2, pp. 91–97, 1998, ISSN: 0001-4842.
- [92] R. Z. Khaliullin, H. Eshet, T. D. Kühne, J. Behler, and M. Parrinello, “Nucleation mechanism for the direct graphite-to-diamond phase transition,” *Nature materials*, vol. 10, no. 9, p. 693, 2011, ISSN: 1476-4660.
- [93] M. Sleutel, J. Lutsko, A. E. Van Driessche, M. A. Durán-Olivencia, and D. Maes, “Observing classical nucleation theory at work by monitoring phase transitions with molecular precision,” *Nature communications*, vol. 5, p. 5598, 2014, ISSN: 2041-1723.
- [94] H. Liu, O.-H. Kwon, J. Tang, and A. H. Zewail, “4d imaging and diffraction dynamics of single-particle phase transition in heterogeneous ensembles,” *Nano letters*, vol. 14, no. 2, pp. 946–954, 2014, ISSN: 1530-6984.
- [95] M. Reading, “Thermal analysis by structural characterization (tasc): Structural and thermo-rheological information from hot stage microscopy,” *Microscopy Today*, vol. 25, no. 5, pp. 18–23, 2017, ISSN: 1551-9295.
- [96] M. Reading, M. Morton, M. Antonijevic, D. Grandy, D. Hourston, and A. Lacey, “New methods of thermal analysis and chemical mapping on a micro and nano scale by combining microscopy with image analysis,” *Microscopy: advances in scientific research and education. Formater Research Center*, pp. 1083–9, 2014.
- [97] M. Alhijjaj, P. Belton, L. Fabian, N. Wellner, M. Reading, and S. Qi, “Novel thermal imaging method for rapid screening of drug–polymer miscibility for solid dispersion based formulation development,” *Molecular pharmaceuticals*, vol. 15, no. 12, pp. 5625–5636, 2018, ISSN: 1543-8384.

- [98] M. Alhijaj, M. Reading, P. Belton, and S. Qi, "Thermal analysis by structural characterization as a method for assessing heterogeneity in complex solid pharmaceutical dosage forms," *Analytical chemistry*, vol. 87, no. 21, pp. 10 848–10 855, 2015, ISSN: 0003-2700.
- [99] M. Alhijaj, S. Yassin, M. Reading, J. A. Zeitler, P. Belton, and S. Qi, "Characterization of heterogeneity and spatial distribution of phases in complex solid dispersions by thermal analysis by structural characterization and x-ray micro computed tomography," *Pharmaceutical research*, vol. 34, no. 5, pp. 971–989, 2017, ISSN: 0724-8741.
- [100] U. S. Kestur, D. Wanapun, S. J. Toth, L. A. Wegiel, G. J. Simpson, and L. S. Taylor, "Nonlinear optical imaging for sensitive detection of crystals in bulk amorphous powders," *Journal of pharmaceutical sciences*, vol. 101, no. 11, pp. 4201–4213, 2012, ISSN: 0022-3549.
- [101] A. U. Chowdhury, C. M. Dettmar, S. Z. Sullivan, S. Zhang, K. T. Jacobs, D. J. Kissick, T. Maltais, H. G. Hedderich, P. A. Bishop, and G. J. Simpson, "Kinetic trapping of metastable amino acid polymorphs," *Journal of the American Chemical Society*, vol. 136, no. 6, pp. 2404–2412, 2014, ISSN: 0002-7863.
- [102] C. J. Smith, J. Dinh, P. D. Schmitt, P. A. Stroud, J. Hinds, M. Johnson, and G. Simpson, "Express: Calibration-free second harmonic generation (shg) image analysis for quantification of trace crystallinity within final dosage forms of amorphous solid dispersions," *Applied spectroscopy*, p. 0 003 702 818 786 506, 2018, ISSN: 0003-7028.
- [103] N. M. Scarborough, G. Godaliyadda, D. H. Ye, D. J. Kissick, S. Zhang, J. A. Newman, M. J. Sheedlo, A. Chowdhury, R. F. Fischetti, and C. Das, "Synchrotron x-ray diffraction dynamic sampling for protein crystal centering," *Electronic Imaging*, vol. 2017, no. 17, pp. 6–9, 2017, ISSN: 2470-1173.
- [104] F. Simon, S. Clevers, V. Dupray, and G. Coquerel, "Relevance of the second harmonic generation to characterize crystalline samples," *Chemical Engineering Technology*, vol. 38, no. 6, pp. 971–983, 2015, ISSN: 0930-7516.
- [105] A. Galland, V. Dupray, B. Berton, S. Morin-Grognon, M. Sanselme, H. Atmani, and G. Coquerel, "Spotting conglomerates by second harmonic generation," *Crystal Growth and Design*, vol. 9, no. 6, pp. 2713–2718, 2009, ISSN: 1528-7483.
- [106] A. T. Francis, T. T. Nguyen, M. S. Lamm, R. Teller, S. P. Forster, W. Xu, T. Rhodes, R. L. Smith, J. Kuiper, and Y. Su, "In situ stimulated raman scattering (srs) microscopy study of the dissolution of sustained-release implant formulation," *Molecular pharmaceutics*, vol. 15, no. 12, pp. 5793–5801, 2018, ISSN: 1543-8384.

- [107] A. Heinz, C. J. Strachan, K. C. Gordon, and T. Rades, "Analysis of solid-state transformations of pharmaceutical compounds using vibrational spectroscopy," *Journal of Pharmacy and Pharmacology*, vol. 61, no. 8, pp. 971–988, 2009, ISSN: 0022-3573.
- [108] J. A. Zeitler, K. Kogermann, J. Rantanen, T. Rades, P. F. Taday, M. Pepper, J. Aaltonen, and C. J. Strachan, "Drug hydrate systems and dehydration processes studied by terahertz pulsed spectroscopy," *International journal of pharmaceuticals*, vol. 334, no. 1-2, pp. 78–84, 2007, ISSN: 0378-5173.
- [109] J. A. Zeitler, D. A. Newnham, P. F. Taday, T. L. Threlfall, R. W. Lancaster, R. W. Berg, C. J. Strachan, M. Pepper, K. C. Gordon, and T. Rades, "Characterization of temperature-induced phase transitions in five polymorphic forms of sulfathiazole by terahertz pulsed spectroscopy and differential scanning calorimetry," *Journal of pharmaceutical sciences*, vol. 95, no. 11, pp. 2486–2498, 2006, ISSN: 0022-3549.
- [110] C. J. Strachan, T. Rades, K. C. Gordon, and J. Rantanen, "Raman spectroscopy for quantitative analysis of pharmaceutical solids," *Journal of pharmacy and pharmacology*, vol. 59, no. 2, pp. 179–192, 2007, ISSN: 0022-3573.
- [111] C. J. Strachan, P. F. Taday, D. A. Newnham, K. C. Gordon, J. A. Zeitler, M. Pepper, and T. Rades, "Using terahertz pulsed spectroscopy to quantify pharmaceutical polymorphism and crystallinity," *Journal of Pharmaceutical Sciences*, vol. 94, no. 4, pp. 837–846, 2005, ISSN: 0022-3549.
- [112] R. D. Muir, S. Z. Sullivan, R. A. Oglesbee, and G. J. Simpson, "Synchronous digitization for high dynamic range lock-in amplification in beam-scanning microscopy," *Review of Scientific Instruments*, vol. 85, no. 3, p. 033 703, 2014, ISSN: 0034-6748.
- [113] S. Gaisford, V. Kett, and P. Haines, *Principles of thermal analysis and calorimetry*. Royal society of chemistry, 2016, ISBN: 1782620516.
- [114] B. T. Raimi-Abraham, J. G. Moffat, P. S. Belton, S. A. Barker, and D. Q. M. Craig, "Generation and characterization of standardized forms of trehalose dihydrate and their associated solid-state behavior," *Crystal Growth Design*, vol. 14, no. 10, pp. 4955–4967, 2014, ISSN: 1528-7483. DOI: [10.1021/cg5004885](https://doi.org/10.1021/cg5004885). [Online]. Available: [%3CGo%20to%20ISI%3E://WOS:000342609300014](https://www.wosid.org/doi/10.1021/cg5004885).
- [115] M. Rani, R. Govindarajan, R. Surana, and R. Suryanarayanan, "Structure in dehydrated trehalose dihydrate - evaluation of the concept of partial crystallinity," *Pharmaceutical Research*, vol. 23, no. 10, pp. 2356–2367, 2006, ISSN: 0724-8741. DOI: [10.1007/s11095-006-9058-6](https://doi.org/10.1007/s11095-006-9058-6). [Online]. Available: [%3CGo%20to%20ISI%3E://WOS:000241112000013](https://www.wosid.org/doi/10.1007/s11095-006-9058-6).

- [116] Z. T. Song, S. Sarkar, A. D. Vogt, G. D. Danzer, C. J. Smith, E. J. Gualtier, and G. J. Simpson, "Kinetic modeling of accelerated stability testing enabled by second harmonic generation microscopy," *Analytical Chemistry*, vol. 90, no. 7, pp. 4406–4413, 2018, ISSN: 0003-2700. DOI: [10.1021/acs.analchem.7b04260](https://doi.org/10.1021/acs.analchem.7b04260). [Online]. Available: [30042938](https://www.ncbi.nlm.nih.gov/pubmed/30042938).
- [117] G. W. H. Höhne, W. Hemminger, and H.-J. Flammersheim, "Theoretical fundamentals of differential scanning calorimeters," in *Differential Scanning Calorimetry*. Springer, 1996, pp. 21–40.
- [118] S. K. Singh, "Sucrose and trehalose in therapeutic protein formulations," in *Challenges in Protein Product Development*. Springer, 2018, pp. 63–95.
- [119] L. S. Taylor, A. C. Williams, and P. York, "Particle size dependent molecular rearrangements during the dehydration of trehalose dihydrate-in situ ft-raman spectroscopy," *Pharmaceutical research*, vol. 15, no. 8, pp. 1207–1214, 1998, ISSN: 0724-8741.
- [120] L. S. Taylor and P. York, "Effect of particle size and temperature on the dehydration kinetics of trehalose dihydrate," *International journal of pharmaceutics*, vol. 167, no. 1-2, pp. 215–221, 1998, ISSN: 0378-5173.
- [121] L. S. Taylor and P. York, "Characterization of the phase transitions of trehalose dihydrate on heating and subsequent dehydration," *Journal of pharmaceutical sciences*, vol. 87, no. 3, pp. 347–355, 1998, ISSN: 0022-3549.
- [122] F. Sussich, R. Urbani, F. Princivale, and A. Cesaro, "Polymorphic amorphous and crystalline forms of trehalose," *Journal of the American Chemical Society*, vol. 120, no. 31, pp. 7893–7899, 1998, ISSN: 0002-7863. DOI: [10.1021/ja9800479](https://doi.org/10.1021/ja9800479). [Online]. Available: [9800479](https://www.ncbi.nlm.nih.gov/pubmed/9800479).
- [123] F. Sussich, F. Princivale, and A. Cesàro, "The interplay of the rate of water removal in the dehydration of , -trehalose," *Carbohydrate research*, vol. 322, no. 1-2, pp. 113–119, 1999, ISSN: 0008-6215.
- [124] X. Y. Dow, E. L. DeWalt, S. Z. Sullivan, P. D. Schmitt, J. R. Ulcickas, and G. J. Simpson, "Imaging the nonlinear susceptibility tensor of collagen by nonlinear optical stokes ellipsometry," *Biophysical journal*, vol. 111, no. 7, pp. 1361–1374, 2016, ISSN: 0006-3495.
- [125] C. Ding, C. Li, F. Deng, and G. J. Simpson, "Axially-offset differential interference contrast microscopy via polarization wavefront shaping," *Optics express*, vol. 27, no. 4, pp. 3837–3850, 2019.

- [126] B. Wunderlich, "Theory of cold crystallization of high polymers," *The Journal of Chemical Physics*, vol. 29, no. 6, pp. 1395–1404, 1958, ISSN: 0021-9606.
- [127] T. Furuki, A. Kishi, and M. Sakurai, "De- and rehydration behavior of alpha,alpha-trehalose dihydrate under humidity-controlled atmospheres," *Carbohydrate Research*, vol. 340, no. 3, pp. 429–438, 2005, ISSN: 0008-6215. DOI: [10.1016/j.carres.2004.12.003](https://doi.org/10.1016/j.carres.2004.12.003). [Online]. Available: [10.1016/j.carres.2004.12.003](https://www.isinet.com/doi/10.1016/j.carres.2004.12.003).
- [128] M. D. Jones, J. C. Hooton, M. L. Dawson, A. R. Ferrie, and R. Price, "Dehydration of trehalose dihydrate at low relative humidity and ambient temperature," *International Journal of Pharmaceutics*, vol. 313, no. 1-2, pp. 87–98, 2006, ISSN: 0378-5173. DOI: [10.1016/j.ijpharm.2006.01.026](https://doi.org/10.1016/j.ijpharm.2006.01.026). [Online]. Available: [10.1016/j.ijpharm.2006.01.026](https://www.isinet.com/doi/10.1016/j.ijpharm.2006.01.026).

## DATA ANALYSIS SCRIPTS

This appendix includes MATLAB data analysis scripts that were used to process images from the FT-FRAP experiments to calculate diffusion properties.

### Normal diffusion analysis by comb photobleach FT-FRAP script

The following is a MATLAB script that is used to analyze a comb photobleach FT-FRAP experiment on a sample exhibiting normal diffusion:

```
% title: ft_frap_analysis
% author: Andreas C Geiger
% date last updated: 2020/11/23
% purpose: this program analyzes ft-frap data
% instructions:
%   1) change user-defined inputs
%   2) Hit "Run"

%% user-defined inputs
path = 'str'; % folder name
file = 'str'; % file name
t0 = 40; % first frame of fluorescence recovery
t_end = 121;
ft_peak = 31; % number of lines - 1
vpix = 512; % number of pixels in vertical axis
hpix = 512; % number of pixels in horizontal axis
microns = 284;% number of microns in one axis

%% import data
FID = fopen(strcat(path, file));
```



```

image = fread(FID, 'uint32');
image = reshape(image, vpix, hpix, []);
image_norm = image ./ mean(image(:, :, 1:21), 3);

%% extract fluorescence recovery with fourier transform
clear ft
clear ft_norm
% compute 2d fourier transform
for i = 1:t_end
    ft(:, :, i) = fft2(image(:, :, i));
    ft_norm(:, :, i) = fft2(image_norm(:, :, i));
end
power = sqrt(ft_norm .* conj(ft_norm));
    % compute power from fourier transform
peak_x = 1:5; % width of peak
peak_y = ft_peak: ft_peak + 2; % length of peak
frap = reshape(sum(power(peak_x, peak_y, t0:end), [1, 2]), 1, []);
    % integrate over peak
t = 4/17 * (0:(numel(frap) - 1));% time in seconds

%% fit fluorescence recovery to recovery diffusion parameters
A = frap(1); % amplitude of recovery
a = mean(sum(power(peak_x, peak_y, 1:20), [1, 2])); % baseline
frap = (frap - a) / (A - a); % normalize and remove baseline

% nonlinear fit
fun = @(r) (1 - r(2)) * exp(-t * 4 * pi^2...
    * (ft_peak / vpix)^2 * r(1)) + r(2) - frap;
    % cost function to minimize
r0 = rand(1, 2); % random initial guess

```

```

options = optimoptions('lsqnonlin', 'MaxFunctionEvaluations', 100000,...
    'MaxIterations', 10000);
[r, ~, residual, ~, ~, ~, jacobian] = ...
lsqnonlin(fun, r0, [], [], options);
    % nonlinear fitting function

% calculate uncertainty in the fit
residual = reshape(residual, 1, []); % residuals from the fit
var_res = var(residual, [], 2); % variance in the residuals
J = full(jacobian); % jacobian from the fit
J = J(:, 1:numel(r));
covar = inv(J' * J) * var_res; % calculate the covariance matrix
[sigma, corr] = cov2corr(covar); % calculate standard deviation

D = r(1) * (microns)^2 / (vpix)^2; % diffusion coefficient in um^2/s
stdev = sigma(1) * (microns)^2 / (vpix)^2;
% standard deviation in um^2/s

%% plot and display results
fit = ...
(1 - r(2)) * exp(-t * 4 * pi^2 * (ft_peak / vpix)^2 * r(1)) + r(2);
    % result from fit

% plot ft-frap data and fit
figure
hold on
plot(t, frap, 'o', 'MarkerSize', 4)
plot(t, fit, 'LineWidth', 2, 'Color', 'r')
xlabel('Time (s)')
ylabel('FT peak intensity')

```

```

% display results
disp('Diffusion Coefficient (um^2 / s)'); disp(D)
disp('Diffusion Coefficient Error (um^2 / s)'); disp(stddev)
disp('Percent Recovery'); disp(r(2))
disp('Percent Recovery Error'); disp(sigma(2))

```

## Flow analysis by comb photobleach FT-FRAP script

The following is a MATLAB script that is used to analyze a comb photobleach FT-FRAP experiment on a sample exhibiting flow:

```

% title: ft_frap_flow
% author: Andreas C Geiger
% date last updated: 2020/11/23
% purpose: this program analyzes ft-frap data from experiments with flow
% instructions:
%   1) change user-defined inputs
%   2) Hit "Run"

%% user-defined inputs
path = ''; % folder name
file = ''; % file name
t0 = 40; % first frame of fluorescence recovery
t_end = 121;
ft_peak = 31; % number of lines - 1
vpix = 512; % number of pixels in vertical axis
hpix = 512; % number of pixels in horizontal axis
microns = 284;% number of microns in one axis

% flow analysis

```

```

flow = 0; % 1 = calculate flow, 0 = do not calculate flow
flow_time = 25; % number of time points in flow analysis
flow_offset = 6; % time offset in flow analysis

%% import data
FID = fopen(strcat(path, file));
image = fread(FID, 'uint32');
image = reshape(image, vpix, hpix, []);
image_norm = image ./ mean(image(:, :, 1:21), 3);

%% extract fluorescence recovery with fourier transform
clear ft
clear ft_norm
% compute 2d fourier transform
for i = 1:t_end
    ft(:, :, i) = fft2(image(:, :, i));
    ft_norm(:, :, i) = fft2(image_norm(:, :, i));
end
% compute power from fourier transform
power = sqrt(ft_norm .* conj(ft_norm));
peak_x = 1:5; % width of peak
peak_y = ft_peak: ft_peak + 2; % length of peak
% integrate over peak
frap = reshape(sum(power(peak_x, peak_y, t0:end), [1, 2]), 1, []);
% real component
frap_real = reshape(real(ft(1, ft_peak, t0:end)), 1, []);
% imaginary component
frap_imag = reshape(imag(ft(1, ft_peak, t0:end)), 1, []);
frap_complex = frap_real + 1i * frap_imag; % complex-valued recovery
t = 4/17 * (0:(numel(frap) - 1)); % time in seconds

```

```

phase = angle(frap_complex); % phase angle of complex number

%% fit fluorescence recovery to recovery diffusion parameters
A = frap(1); % amplitude of recovery
a = mean(sum(power(peak_x, peak_y, 1:20), [1, 2])); % baseline
frap = (frap - a) / (A - a); % normalize and remove baseline

% nonlinear fit
% cost function to minimize
fun = @(r) (1 - r(2)) * ...
    exp(-t * 4 * pi^2 * (ft_peak / vpix)^2 * r(1)) + r(2) - frap;
r0 = rand(1, 2); % random initial guess
options = optimoptions('lsqnonlin', 'MaxFunctionEvaluations', 100000,...
    'MaxIterations', 10000);
% nonlinear fitting function
[r, ~, residual, ~, ~, ~, jacobian] = lsqnonlin(fun, ...
    r0, [], [], options);

% calculate uncertainty in the fit
residual = reshape(residual, 1, []); % residuals from the fit
var_res = var(residual, [], 2); % variance in the residuals
J = full(jacobian); % jacobian from the fit
J = J(:, 1:numel(r));
covar = inv(J' * J) * var_res; % calculate the covariance matrix
[sigma, corr] = cov2corr(covar); % calculate standard deviation

D = r(1) * (microns)^2 / (vpix)^2; % diffusion coefficient in um^2/s
stdev = sigma(1) * (microns)^2 / (vpix)^2;
% standard deviation in um^2/s

```

```

%% flow analysis
phase_v = phase(1 + flow_offset:flow_time + flow_offset);
t_v = t(1:flow_time);

% linear fit
beta_v = [sum(phase_v); sum(t_v .* phase_v)];
alpha_v = [numel(t_v), sum(t_v);
           sum(t_v), sum(t_v.^2)];
v = alpha_v \ beta_v;
v_fit = v(1) + v(2) * t_v;

% calculate uncertainty in the fit
ssr = sum((v_fit - phase_v).^2); %% sum of squared residuals
sigma_2r = ssr / (numel(phase_v) - 2); % divide by degrees of freedom
ssxx_slope = sum((t_v - mean(t_v)).^2);
sigma_slope = sqrt(sigma_2r / ssxx_slope);

flow_v = v(2) / 2 / pi / ft_peak * microns; % flow velocity in um / s
flow_std = sigma_slope / 2 / pi / ft_peak * microns;
% standard deviation

%% plot and display results
% result from fit
fit = ...
(1 - r(2)) * exp(-t * 4 * pi^2 * (ft_peak / vpix)^2 * r(1)) + r(2);

% plot ft-frap data and fit
figure
hold on
plot(t, frap, 'o', 'MarkerSize', 4)

```

```

plot(t, fit, 'LineWidth', 2, 'Color', 'r')
xlabel('Time (s)')
ylabel('FT peak intensity')

% plot flow analysis results
if flow
    figure
    hold on
    plot(t(1:100), frap_real(1:100))
    plot(t(1:100), frap_imag(1:100))
    xlabel('Time (s)')
    ylabel('FT peak amplitude')
    legend('Real', 'Imaginary')
    figure
    hold on
    plot(t_v, phase_v, 'o', 'MarkerSize', 5)
    plot(t_v, v_fit, 'LineWidth', 2, 'Color', 'r')
    xlabel('Time (s)')
    ylabel('Phase (rad)')
    legend('Experimental', 'Linear fit')
end

% display results
disp('Diffusion Coefficient (um^2 / s)'); disp(D)
disp('Diffusion Coefficient Error (um^2 / s)'); disp(stdev)
disp('Percent Recovery'); disp(r(2))
disp('Percent Recovery Error'); disp(sigma(2))
disp('Flow (um / s)'); disp(flow_v)
disp('Flow Error (um / s)'); disp(flow_std)

```

## Anomalous diffusion analysis by comb photobleach FT-FRAP script

The following is a MATLAB script that is used to analyze a comb photobleach FT-FRAP experiment on a sample exhibiting anomalous diffusion. The script contains a MATLAB function named "ml.m" written by Roberto Garrappa for evaluating the Mittag-Leffler function:

```
path = 'str';
file = 'str';
t0 = 40;
ft_peak_1 = 31;
ft_peak_2 = ft_peak_1 * 2;
ft_peak_3 = ft_peak_1 * 3;
peak_x = 1:3;
peak_y_1 = ft_peak_1:ft_peak_1 + 2;
peak_y_2 = ft_peak_2:ft_peak_2 + 2;
peak_y_3 = ft_peak_3:ft_peak_3 + 2;

%%
FID = fopen(strcat(path, file));
image = fread(FID, 'uint32');
image = reshape(image, 512, 512, []);

%%
clear ft
for i = 1:numel(image(1, 1, :))
ft(:, :, i) = fft2(image(:, :, i));
end
power = sqrt(ft .* conj(ft));
%power = power(:, :, 1:100);
frap_1 = reshape(sum(sum(power(peak_x, peak_y_1, t0:end))), 1, []);
```



```

frap_2 = reshape(sum(sum(power(peak_x, peak_y_2, t0:end))), 1, []);
frap_3 = reshape(sum(sum(power(peak_x, peak_y_3, t0:end))), 1, []);

%%
A_1 = max(frap_1);
a1_1 = mean(sum(sum(power(peak_x, peak_y_1, 1:20))));
frap_1 = (frap_1 - a1_1) / (A_1 - a1_1);
A_2 = max(frap_2);
a1_2 = mean(sum(sum(power(peak_x, peak_y_2, 1:20))));
frap_2 = (frap_2 - a1_2) / (A_2 - a1_2);
A_3 = max(frap_3);
a1_3 = mean(sum(sum(power(peak_x, peak_y_3, 1:20))));
frap_3 = (frap_3 - a1_3) / (A_3 - a1_3);
t = 4/17 * (0:(numel(frap_1) - 1));
N = numel(t);

fun = @(r) cat(2,
    (1 - r(2)) * ml(-t.^(2 * r(5)/r(6)))...
    * (2 * pi * ft_peak_1 / 512)^(r(6)) * r(1), r(5))...
    + r(2) - frap_1,...
    (1 - r(3)) * ml(-t.^(2 * r(5)/r(6)))...
    * (2 * pi * ft_peak_2 / 512)^(r(6)) * r(1), r(5))...
    + r(3) - frap_2,...
    (1 - r(4)) * ml(-t.^(2 * r(5)/r(6)))...
    * (2 * pi * ft_peak_3 / 512)^(r(6)) * r(1), r(5))...
    + r(4) - frap_3);

r0 = rand(1, 6);
lb = [0, -0.5, -0.5, -0.5 0, 0];

```

```

ub = [inf, 1, 1, 1, 2, 4];
options = optimoptions('lsqnonlin', 'MaxFunctionEvaluations', 100000,...
    'MaxIterations', 10000);
[r, ~, residual, ~, ~, ~, jacobian] = ...
lsqnonlin(fun, r0, lb, ub, options);
% r(1) = Diffusion Coefficient, r(2)-r(4) = recoverable fractions,
% r(5) = alpha parameter - normal = 1, r(6) = mu parameter - normal = 2
residual = reshape(residual, 1, []);
var_res = var(residual, [], 2);
J = full(jacobian);
J = J(:, 1:numel(r));
covar = inv(J' * J) * var_res;
[sigma, corr] = cov2corr(covar);

fit_1 = (1 - r(2)) * ml(-t.^(2 * r(5)/r(6)))...
    * (2 * pi * ft_peak_1 / 512)^(r(6)) * r(1), r(5)) + r(2);
fit_2 = (1 - r(3)) * ml(-t.^(2 * r(5)/r(6)))...
    * (2 * pi * ft_peak_2 / 512)^(r(6)) * r(1), r(5)) + r(3);
fit_3 = (1 - r(4)) * ml(-t.^(2 * r(5)/r(6)))...
    * (2 * pi * ft_peak_3 / 512)^(r(6)) * r(1), r(5)) + r(4);

figure
hold on
plot(t, frap_1, 'o', 'MarkerSize', 4)
plot(t, fit_1, 'LineWidth', 2)
plot(t, frap_2, 'o', 'MarkerSize', 4)
plot(t, fit_2, 'LineWidth', 2)
plot(t, frap_3, 'o', 'MarkerSize', 4)
plot(t, fit_3, 'LineWidth', 2)
xlabel('Time (s)')

```

```

ylabel('FT peak intensity')

factor = (808)^2 / (512)^2;
r(1) = r(1) * factor;
sigma(1) = sigma(1) * factor;

```

## Dot-array photobleach FT-FRAP normal diffusion analysis script

The following is a MATLAB script that is used to analyze a dot-array photobleach FT-FRAP experiment on a sample exhibiting normal diffusion.

```

% title: ft_frap_h_k_harmonic
% author: Andreas C Geiger
% date last updated: 2020/09/14
% purpose: this program analyzes ft-frap data with a dot-matrix
% photobleach pattern
% instructions:
% 1) change user-defined inputs
% 2) Hit "Run"

%% user-defined inputs
path = ''; % folder name
t0 = 6; % first frame after photobleaching
t_end = 100; % last frame to analyze
h_max = 1; % highest peak index in x-axis
k_max = 1; % highest peak index in y-axis
a = round(sqrt(2^2 + 12^2)); % number of pixels between Fourier peaks
theta = atan(12/2); % angle of peak between 0 and pi/2
x_crop = 1:700; % range of pixels to crop in x-axis (y-axis in imagesc)
% range of pixels to crop in y-axis (x-axis in imagesc)
y_crop = 350:350 + 699;

```

```

% conversion factor from pixels to microns (microns divided by pixels)
factor = 1604 / 1392;

%% error messages
xpix = numel(x_crop); % number of pixels in x_range
ypix = numel(y_crop); % number of pixels in y_range
if xpix ~= ypix
    error('ERROR: xpix and ypix must be equal')
end

%% read image files
directory = dir(path); % obtain list of objects in folder
im = 0; % initialize index
% waitbar(0, 'Reading image files') % initialize waitbar
for i = 1:numel(directory)
    if contains(directory(i).name, '.tif')
        im = im + 1; % increase index by one for every file
        file = directory(i).name; % obtain file name
        data = imread(strcat(path, file)); % import image file
        image(:, :, im) = double(data(:, :, 1)); % save to workspace
        t(im) = str2double(directory(i).name(end-9:end-4)) * 0.001;
    end
end

t = t(t0:t_end); % discard pre-photobleach and photobleach frames
% adjust the time 0 to be at the bleach point. to exclude the prebleach
t = t - t(1);

image_norm = image ./ mean(image(:, :, 1:3), 3); % normalize images
image_norm = image_norm(x_crop, y_crop, :); % crop images

```

```

%% calculate fourier transform
clear ft
clear ft_norm
for i = 1:t_end
ft(:, :, i) = fft2(image(:, :, i)); % fourier transform
% fourier transform of normalized images
ft_norm(:, :, i) = fft2(image_norm(:, :, i));
% shift fourier transform to center
ft_norm(:, :, i) = fftshift(ft_norm(:, :, i));
end
% compute power from fourier transform
power = sqrt(ft_norm .* conj(ft_norm));

%% identify coordinates of fourier peaks
peak_x_grid = a * repmat([0:h_max]', [1, k_max + 1]); % x coordinates
peak_y_grid = a * repmat(0:k_max, [h_max + 1, 1]); % y coordinates
% rotation
peak_x = round(cos(theta) * peak_x_grid - sin(theta) * peak_y_grid);
peak_y = round(sin(theta) * peak_x_grid + cos(theta) * peak_y_grid);
peak_x = peak_x + xpix / 2; % move to center
peak_y = peak_y + ypix / 2; % move to center

%% extract fluorescence recovery signal
% preallocate arrays
frap = zeros(h_max^2 + k_max^2, t_end - t0 + 1);
a1 = zeros(h_max^2 + k_max^2, 1);
% loop through each fourier peak
for h = 0:h_max
    for k = 0:k_max

```

```

n2= h^2 + k^2; % calculate distance from origin
if n2 > 0
    % extract fluorescence recovery and sum equidistant peaks
    frap(n2, :) = frap(n2, :) + reshape(sum(sum(power...
        (peak_x(h + 1, k + 1):peak_x(h + 1, k + 1) + 2,...
        peak_y(h + 1, k + 1):peak_y(h + 1, k + 1) + 2,...
        t0:t_end), 1), 2), 1, []));
    a1(n2, :) = a1(n2, :) + mean(sum(sum(power...
        (peak_x(h + 1, k + 1):peak_x(h + 1, k + 1) + 2, ...
        peak_y(h + 1, k + 1):peak_y(h + 1, k + 1) + 2, ...
        1:3), 1), 2)); % calculate background
end
end
end

% excludes columns with no data
n2_i = [1:n2]';
n2_i(sum(frap, 2) == 0) = [];
frap(sum(frap, 2) == 0, :) = [];
a1(sum(a1, 2) == 0, :) = [];

%% fit fluorescence recovery to diffusion model
A = frap(:, 1); % first frap data point
frap = (frap - a1) ./ (A - a1); % normalize frap data

% nonlinear fit
fun = @(r) fun_h_k(r, frap, t, n2_i, a); % function to minimize

r0 = rand(numel(n2_i) + 1, 1); % random initial guess values
lb = cat(1, 0, -0.5 * ones(numel(n2_i), 1)); % lower bound

```

```

ub = cat(1, inf, 1 * ones(numel(n2_i), 1)); % upper bound

% least-squares minimization
[r, ~, residual, ~, ~, ~, jacobian] = lsqnonlin(fun, r0, lb, ub);
% r(1) = diffusion coefficient (pixels^2/s)
% r(2:end) = recoverable fraction

% error analysis
residual = reshape(residual, 1, []);
var_res = var(residual, [], 2);
J = full(jacobian);
J = J(:, 1:numel(r));
covar = inv(J' * J) * var_res;
[sigma, corr] = cov2corr(covar);
sigma = sigma'; % standard deviation of the fit

%% plot results of fit
% calculate best-fit curve
D = r(1);
R = r(2:end);
fit = (1 - R) .* exp(-4 * pi^2 * (n2_i / a^2) * D * t) + R;

% generate figure
figure
hold on
plot(t, frap, 'o', 'MarkerSize', 4)
plot(t, fit, 'LineWidth', 2)

% convert from pixels to microns
r(1) = r(1) * factor^2; % diffusion coefficient (um^2/s)

```

```
sigma(1) = sigma(1) * factor^2; % standard deviation of the fit
```

The previous script uses a MATLAB function named "fun\_h\_k.m", which is as follows:

```
function F = fun_h_k(r, frap, t, n2_i, a)
```

```
D = r(1);
```

```
R = r(2:end);
```

```
F = (1 - R) .* exp(-4 * pi^2 * (n2_i / a^2) * D * t) + R - frap;
```

### **Diffusion imaging by comb photobleach FT-FRAP script**

The following is a MATLAB script that is used to perform diffusion imaging by comb photobleach FT-FRAP experiment on a sample exhibiting anomalous diffusion. In this script, the image is segmented and pixels are pooled prior to fitting for greater SNR in the recovered diffusion properties.

```
% title: ft_frap_analysis_segmented_m1
```

```
% author: Andreas C Geiger
```

```
% date last updated: 2021/02/09
```

```
% purpose: this program produces segmented images...
```

```
%   of diffusion properties from a comb-bleach ft-frap...
```

```
%   experiment with a sample exhibiting anomalous diffusion
```

```
% instructions:
```

```
%   1) change user-defined inputs
```

```
%   2) Hit "Run"
```

```
%% user-defined inputs
```

```
path = '' % folder name
```

```
file = '' % file name
```

```
t0 = 40; % first frame of fluorescence recovery
```



```

t_end = 400;
ft_peak_1 = 31; % number of lines - 1
ft_peak_2 = 31 * 2;
ft_peak_3 = 31 * 3;
vpix = 512; % number of pixels in vertical axis
hpix = 512; % number of pixels in horizontal axis
microns = 693;% number of microns in one axis

%% import data
FID = fopen(strcat(path, file));
image = fread(FID, 'float32');
image = reshape(image, vpix, hpix, []);
image_norm = image ./ mean(image(:, :, 1:20), 3);

%% extract fluorescence recovery with fourier transform
clear ft
% compute 2d fourier transform
for i = 1:t_end %numel(image(1, 1, :))
    ft(:, :, i) = fft2(image(:, :, i));
    ft_norm(:, :, i) = fft2(image_norm(:, :, i));
    %ft(:, :, i) = fftshift(ft(:, :, i));
end
power = sqrt(ft_norm .* conj(ft_norm));
% compute power from fourier transform
peak_x = 1:3;
peak_y_1 = ft_peak_1:ft_peak_1 + 2;
peak_y_2 = ft_peak_2:ft_peak_2 + 2;
peak_y_3 = ft_peak_3:ft_peak_3 + 2;

%% peak shape analysis

```

```

% crop and center ft peaks
ft_crop_1 = ft_norm(:, ft_peak_1 + 1:end - ft_peak_1, :);
ft_crop_1(:, round(ft_peak_1/4):end - round(ft_peak_1/4), :) = 0;
ft_crop_1(round(ft_peak_1/4):end - round(ft_peak_1/4), :, :) = 0;

ft_crop_2 = ft_norm(:, ft_peak_2 + 1:end - ft_peak_2, :);
ft_crop_2(:, round(ft_peak_1/4):end - round(ft_peak_1/4), :) = 0;
ft_crop_2(round(ft_peak_1/4):end - round(ft_peak_1/4), :, :) = 0;

ft_crop_3 = ft_norm(:, ft_peak_3 + 1:end - ft_peak_3, :);
ft_crop_3(:, round(ft_peak_1/4):end - round(ft_peak_1/4), :) = 0;
ft_crop_3(round(ft_peak_1/4):end - round(ft_peak_1/4), :, :) = 0;

% perform inverse ft on cropped and centered ft peaks
for i = 1:numel(ft_norm(1, 1, :))
    ift_crop_1(:, :, i) = ifft2(ft_crop_1(:, :, i) , 512, 512);
    diff_im_1(:, :, i) =...
    sqrt(ift_crop_1(:, :, i) .* conj(ift_crop_1(:, :, i)));
    diff_im_gauss_1(:, :, i) = imgaussfilt(diff_im_1(:, :, i), 10);

    ift_crop_2(:, :, i) = ifft2(ft_crop_2(:, :, i) , 512, 512);
    diff_im_2(:, :, i) =...
    sqrt(ift_crop_2(:, :, i) .* conj(ift_crop_2(:, :, i)));
    diff_im_gauss_2(:, :, i) = imgaussfilt(diff_im_2(:, :, i), 10);

    ift_crop_3(:, :, i) = ifft2(ft_crop_3(:, :, i) , 512, 512);
    diff_im_3(:, :, i) =...
    sqrt(ift_crop_3(:, :, i) .* conj(ift_crop_3(:, :, i)));
    diff_im_gauss_3(:, :, i) = imgaussfilt(diff_im_3(:, :, i), 10);
end

```

```

% pool inverse ft pixels from each image segment
for i = 1:numel(mask_segment(1, 1, :))
    diff_region_1(i, :) = ...
        mean(mean(diff_im_1 .* mask_segment(:, :, i), 1), 2);
    diff_region_2(i, :) = ...
        mean(mean(diff_im_2 .* mask_segment(:, :, i), 1), 2);
    diff_region_3(i, :) = ...
        mean(mean(diff_im_3 .* mask_segment(:, :, i), 1), 2);
end

% background subtraction and normalization
A_1 = diff_region_1(:, 40);
a1_1 = mean(diff_region_1(:, 1:20), 2);
diff_1 = (diff_region_1(:, 40:end) - a1_1) ./ (A_1 - a1_1);

A_2 = diff_region_2(:, 40);
a1_2 = mean(diff_region_2(:, 1:20), 2);
diff_2 = (diff_region_2(:, 40:end) - a1_2) ./ (A_2 - a1_2);

A_3 = diff_region_3(:, 40);
a1_3 = mean(diff_region_3(:, 1:20), 2);
diff_3 = (diff_region_3(:, 40:end) - a1_3) ./ (A_3 - a1_3);

%% nonlinear fit to diffusion model

% upper and lower bounds of fitting parameters
lb = [0, -0.5, -0.5, -0.5, 0, 0];
ub = [inf, 1, 1, 1, 2, 4];
% r(1) = Diffusion Coefficient,

```

```

% r(2)-r(4) = recoverable fractions,
% r(5) = alpha parameter, r(6) = mu parameter

% initial arrays
diff_map = zeros(512, 512);
s_diff_map = zeros(512, 512);
rec_map = zeros(512, 512);
alpha_map = zeros(512, 512);
s_alpha_map = zeros(512, 512);
mu_map = zeros(512, 512);
s_mu_map = zeros(512, 512);

frap_1 = diff_1;
frap_2 = diff_2;
frap_3 = diff_3;

t = 4/17 * (0:(length(frap_1) - 1));% time in seconds

% perform fit on frap decay from each image segment
for i = 1:numel(mask_segment(1, 1, :))

    % function to minimize
    fun = @(r) cat(2, (1 - r(2)) * ml(-t.^(2 * r(5)/r(6))...
        * (2 * pi * ft_peak_1 / 512)^(r(6)) * r(1), r(5))...
        + r(2) - frap_1(i, :),...
        (1 - r(3)) * ml(-t.^(2 * r(5)/r(6))...
        * (2 * pi * ft_peak_2 / 512)^(r(6)) * r(1), r(5))...
        + r(3) - frap_2(i, :),...
        (1 - r(4)) * ml(-t.^(2 * r(5)/r(6))...
        * (2 * pi * ft_peak_3 / 512)^(r(6)) * r(1), r(5))...

```

```

    + r(4) - frap_3(i, :));

r0 = rand(1, 6);
[r, ~, residual, ~, ~, ~, jacobian] = lsqnonlin(fun, r0, lb, ub);
% r(1) = Diffusion Coefficient,
%r(2)-r(4) = recoverable fractions,
%r(5) = alpha parameter, r(6) = mu parameter

% uncertainty analysis
residual = reshape(residual, 1, []);
var_res = var(residual, [], 2);
J = full(jacobian);
J = J(:, 1:numel(r));
covar = inv(J' * J) * var_res;
if sum(diag(covar) >= 0) == numel(r0)
    [sigma, ~] = cov2corr(covar);

% store recovered diffusion parameters and uncertainties
diff_map = diff_map + r(1)...
* (microns)^2 / (vpix)^2 * mask_segment(:, :, i);
s_diff_map = s_diff_map + sigma(1)...
* (microns)^2 / (vpix)^2 * mask_segment(:, :, i);
rec_map = rec_map + r(2) * mask_segment(:, :, i);
alpha_map = alpha_map + r(5) * mask_segment(:, :, i);
s_alpha_map = s_alpha_map + sigma(5)...
* (microns)^2 / (vpix)^2 * mask_segment(:, :, i);
mu_map = mu_map + r(6) * mask_segment(:, :, i);
s_mu_map = s_mu_map + sigma(6)...
* (microns)^2 / (vpix)^2 * mask_segment(:, :, i);

```

```

% store best-fit curves
fit(:, 1, i) = (1 - r(2)) * ml(-t.^(2 * r(5)/r(6))...
* (2 * pi * ft_peak_1 / 512)^(r(6)) * r(1), r(5)) + r(2);
fit(:, 2, i) = (1 - r(3)) * ml(-t.^(2 * r(5)/r(6))...
* (2 * pi * ft_peak_2 / 512)^(r(6)) * r(1), r(5)) + r(3);
fit(:, 3, i) = (1 - r(4)) * ml(-t.^(2 * r(5)/r(6))...
* (2 * pi * ft_peak_3 / 512)^(r(6)) * r(1), r(5)) + r(4);

end

end

```

## VITA

The son of Philip Marc Geiger and Linda Su Johnson Geiger, Andreas Crispin Geiger was born a triplet in Cambridge, Massachusetts on April 3, 1994. Andreas was raised in the town of Londonderry, New Hampshire with his siblings Devereux, Mariah, Leanna, and Denis. In 2012, Andreas graduated from Londonderry High School and left his hometown to study chemistry at Wheaton College in Wheaton, IL. While at Wheaton, he performed biochemistry research with professors Daniel and Lisa Burden and competed on the cross country and track & field teams. Between his junior and senior years at Wheaton College, Andreas married Ytai Flores, also a Wheaton College student-athlete. After graduating in 2016, Andreas and Ytai moved to West Lafayette, Indiana for Andreas to pursue a Ph.D. in chemistry at Purdue University. While at Purdue, Andreas conducted analytical chemistry research under the mentorship of professor Garth Simpson and his thesis work consisted of the design and construction of a microscope and data analysis programs for measuring diffusion through spatial frequency analysis. While in West Lafayette, Andreas and Ytai had two sons, Josiah and Nathan, who were born in 2016 and 2018, respectively, and they are expecting a third son, David, in 2021.

## SELECTED PUBLICATIONS

1. Geiger, A. C., C. J. Smith, N. Takanti, D. M. Harmon, M. S. Carlsen, and G. J. Simpson. 2020. Anomalous Diffusion Characterization by Fourier Transform-FRAP with Patterned Illumination. *Biophysical Journal* 119(4):737-748. Article.
2. Geiger, A. C., Cao, Z., Song, Z., Ulcickas, J. R., and Simpson, G. J. 2020. Autonomous Science: Big Data Tools for Small Data Problems in Chemistry. *Machine Learning in Chemistry*, 17, 450. Book Chapter.
3. Sherman, A. M., Geiger, A. C., Smith, C. J., Taylor, L. S., Hinds, J., Stroud, P. A., and Simpson, G. J. 2019. Stochastic Differential Scanning Calorimetry by Nonlinear Optical Microscopy. *Analytical Chemistry*, 92(1), 1171-1178. Article.



## CHAPTER 18

# *Autonomous Science: Big Data Tools for Small Data Problems in Chemistry*

ANDREAS C. GEIGER, ZIYI CAO, ZHENGtian SONG,  
JAMES R. W. ULCICKAS AND GARTH J. SIMPSON\*

Purdue University, Department of Chemistry, 560 Oval Drive,  
West Lafayette, IN 47907, USA

\*Email: [gsimpson@purdue.edu](mailto:gsimpson@purdue.edu)

### 18.1 Introduction

Arguably, the greatest opportunities to capitalize on machine learning advances lie at the interface between data science and measurement science; algorithms can inform the choice of measurements, which in turn can serve as inputs to algorithms. In this framework, two general classes of data science challenges emerge. In the first, the ever-increasing volume of data produced by high throughput (HT) instrumentation generates databases that can subsequently be mined.<sup>1–5</sup> Alternatively, many chemical measurements are limited by instrumental, kinetic, or sample constraints, restricting the number of measurements that can be practically made to inform decisions. This latter case is the primary focus of the present work, in which “big data” tools are brought to bear to optimize the information content produced by the fewest possible experimental measurements.

In contrast, most machine learning methods have focused on analysis and training using large volumes of preexisting data, including those generated

*Autonomous Science: Big Data Tools for Small Data Problems in Chemistry*

by HT chemical instrumentation. HT screening has been applied to cell-based microfluidics,<sup>6–10</sup> protein engineering,<sup>11–15</sup> metabolomics,<sup>16–20</sup> proteomics,<sup>21–25</sup> pharmacotoxicology,<sup>26–28</sup> nanomaterials synthesis,<sup>29</sup> and efforts in small-molecule synthetic optimization.<sup>30,31</sup> Techniques like these have enabled researchers to collect “big data” in ever shorter periods of time, which can then be mined for pattern-analysis and data-driven decision-making.

In turn, machine learning methods have been applied extensively in mining of chemistry databases, spanning a range of applications. Algorithms have been demonstrated with the capability of predicting chemical reactivities,<sup>32,33</sup> predicting compound properties<sup>34–36</sup> and determining chemical structures.<sup>37</sup> Zhuo and coworkers developed a machine-learning model that accurately predicted the band gap of inorganic solids solely from composition.<sup>38</sup> The model used support vector classification to separate metals from nonmetals and support vector regression to predict the band gap. The results from this method were closer to experimentally reported values than density functional theory calculations. Coley and coworkers used a graph-convolutional neural network to predict the major product of a reaction.<sup>39</sup> The network accurately predicted the major product 85% of the time, a significant improvement from previous methods. Turcani and coworkers predicted shape persistence and cavity size in porous organic cages using a random forest algorithm.<sup>40</sup> Their model achieved a 93% accuracy for the prediction of shape persistence. Advances like these have made it possible for chemists to leverage their “big data” to make impactful discoveries.

One obvious limitation on “big data” tools is the requirement that the data must be big. Many time-consuming experiments are incommensurate with conventional machine learning methods because of the intrinsic sparsity of the available data. An illustrative example is the National Ignition Facility at Lawrence Livermore National Laboratory, which houses the world’s largest and most energetic laser.<sup>41–43</sup> The laser (formally a combination of 192 lasers) is only fired about 400 times per year ( $\sim 10^{-5}$  Hz repetition rate). The capacity for such experiments to benefit from machine learning tools lies in the ability to optimally select conditions for the next experiments based on the limited availability of preceding information. Such cases are arguably best described as “little data” problems, presenting both challenges and opportunities for integration into the emerging “big data” infrastructure.

These challenges are not new. Rather than random “shotgun” sampling, an experienced bench chemist working the laboratory with limited data availability will generally use the outcomes of the preceding set of measurements to inform the next selection of conditions (or more commonly, to know which conditions to avoid). Rationale for selection of the next experiment is typically made by combining the observations to date with the experience of the investigator in working with similar compounds in similar scenarios. Porting this decision-making process over to machine learning platforms

involves methods capable of both capturing the experience of the bench chemist from general knowledge of related molecular systems and approaches for optimally selecting the most informative next set of experiments.

When coupled with experimental automation, this algorithm-driven independent design of experiments enables autonomous science, in which machine learning or AI algorithms are trained to design experiments, interpret results, and execute additional measurements through hardware automation. In principle, such systems operate independently in all phases of the scientific method. As shown in Figure 18.1, hypothesis-making, experimental design, data collection, data analysis, and hypothesis-testing are performed iteratively with all previous experiments informing the design of future experiments until chemical space is sufficiently mapped to provide an answer.

Autonomous instrumentation should be distinguished from automated instrumentation. Many modern laboratories have increased experimental throughput by fully automating processes that were previously done by hand.<sup>44–48</sup> The emerging revolution in chemical measurement science is in automating the hypothesis-making and experimental design steps in the scientific method.<sup>49–51</sup> By delegating these tasks to algorithms, the loop can be closed to reduce human intervention in the scientific method.

The rest of this chapter will delve into topics that are relevant for the development of machine learning algorithms and autonomous

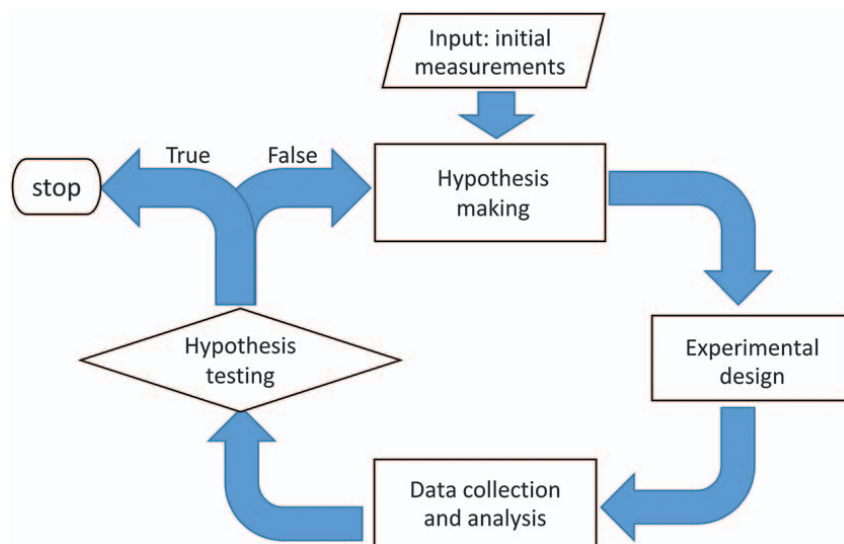


**Figure 18.1** Diagram of the scientific method. An autonomous laboratory can independently operate in all phases of the scientific method. Adapted from ref. 54, <https://doi.org/10.1107/s160057751601612x>, under the terms of the CC BY 4.0 licence, <https://creativecommons.org/licenses/by/4.0/>.

instrumentation for optimized collection in “little data” situations, in which the number of experiments is limited by time, sample, or expense. An overview of autonomous experimental design and execution will detail strategies for implementing experiments with algorithms producing autonomous scientific decisions. One architecture for autonomous chemistry will be reviewed in detail, building upon the concept of sparsely sampling chemical space, to dynamically sampling chemical space, and finally a supervised learning approach to dynamic sampling as applied to chemical imaging. Furthermore, a detailed discussion is presented on the potential for adversarial attacks against algorithms that are used in a chemical context. The discussion reveals that dimension reduction techniques are potentially susceptible to adversarial attacks and provides relevant context on the general robustness of machine-learning-based classifiers for autonomous science. Some suggestions and methods to improve general stability *versus* adversarial attacks and spurious misclassification are discussed.

## 18.2 Autonomous Design of Experiments

Autonomous science requires both the ability to act independently (automation) and to make independent decisions based upon evolving knowledge (intelligence). The focus of this chapter is squarely on the latter, as automation is a largely solved problem on many modern instruments supporting HT analyses. An autonomous system is an “expert” that can incorporate new information to revise a governing hypothesis and guide improvements. This definition can be broken down into two key constituent functions: the acquisition of new information, and the selection of future experiments. The focus here largely rests upon autonomous systems designed to reduce the experimental burden associated with mapping chemical space. Initial discussions will focus on a prerequisite capacity for functioning autonomous systems: the ability to extrapolate anticipated experimental outcomes from previously sampled data. Fixed pattern sparse sampling strategies will serve to illustrate some approaches that can be undertaken to achieve this goal. The discussion of sparse sampling will be followed by a survey of dynamic sampling approaches, which aim to reconstruct chemical space with the smallest number of measurements. These methods differ from fixed pattern sparse sampling strategies in that real-time experimental observations can be leveraged to inform future experiments on the fly. Various algorithms for dynamic sampling will be discussed, first in the intuitively simple context of chemical imaging, and later in the more abstract context of chemical space (*e.g.*, protein concentrations in live cell cultures). This section will conclude with a brief discussion of modularized autonomous laboratories with multiple autonomous instruments, which utilize advanced software that integrates various modules (*e.g.*, communication, databases, robotics, characterization, learning, and analysis) to map highly complex feature spaces.

### 18.2.1 Sparse Sampling Strategies for “Small Data” Challenges

In cases where single experiments can be relatively costly, building a map of observables as a function of experimental parameters can be accelerated by using sparse sampling strategies. Chemical measurements tend to be highly correlated, providing opportunities for sparse sampling. Using chemical imaging as an example, the composition in a given pixel is likely to be highly dependent on the composition in adjacent pixels. As such, reasonably good estimates of the composition distribution can be made from sampling a subset of the total number of pixels and “inpainting” the unsampled locations. The presence of correlations between measurements is a fundamental requirement of autonomous science; if every measurement were completely independent, no rationale would be available for selecting any particular set of conditions. Learning the underlying patterns connecting chemical measurements is a critical first step in developing methods for autonomous science.

Applications involving chemical imaging can leverage advances in image recognition to assist in predicting spatial correlations in chemical composition. Using these tools, architectures for generating complete representations of chemical space from a limited number of sampling events have had great success in novel sampling strategies to sparsely collect data from point-probe microscopes (*e.g.*, Raman microscopy,<sup>52</sup> scanning electron microscopy (SEM),<sup>53</sup> synchrotron X-ray diffraction<sup>54</sup>). In point-wise image acquisitions, sparse sampling offers the potential to dramatically reduce the number of measurements. Sparse sampling methods have been implemented to minimize sample damage for beam-sensitive materials, reducing total time for data acquisition and minimizing sample exposure to potential structural change from, *e.g.*, X-ray or electron dose.<sup>55,56</sup>

There are two main components of a sparse sampling strategy: the sparse sampling pattern and the “inpainting” algorithm. Figure 18.2 illustrates the general strategy in sparse sampling. The pattern used determines which experiments will be performed; in many cases, the most intuitive pattern is random, which generates a wide distribution of measurements to inform the “inpainting” algorithm and leaves minimal artifacts from the sampling pattern. However, random sampling can increase measurement time significantly compared to continuous sampling patterns. For example, in beam scanning fluorescence microscopy, the time required to re-position the laser beam at a random pixel (milliseconds) is far greater than the time required to measure a pixel (nanoseconds). In this case, a continuous sampling pattern (*e.g.* Lissajous trajectories) takes full advantage of the sampling speed while also sampling from a wide distribution of positions in the field of view. The optimal sampling pattern for a sparse sampling strategy will be specific to each technique and dependent on the slowest step in the measurement.

In previous studies, sparse sampling patterns such as random sampling, low-discrepancy sampling, and Lissajous trajectories were employed to accelerate data collection. Simpson and coworkers developed a beam-scanning

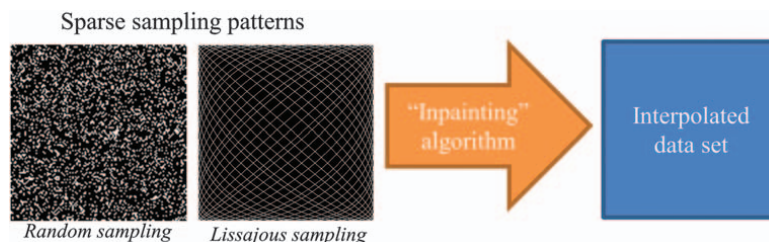


**Figure 18.2** Sparse sampling combines fixed or random sampling patterns with “inpainting” algorithms. This reduces total measurement time by “inpainting” unsampled conditions and locations with predictions rather than performing measurements at every condition and location. Sparse sampling strategies rely on correlations between proximal data points.

optical microscope based on Lissajous trajectory imaging, which achieved up to kHz frame-rate optical imaging on multiple simultaneous data acquisition channels.<sup>57,58</sup> They used two fast-scan resonant mirrors to direct the optical beam on a circuitous trajectory through the field of view and used an “inpainting” algorithm to interpolate unsampled pixels.

Once sparsely sampled data are collected, it is the job of the “inpainting” algorithm to predict the values of unsampled conditions and locations. If only local correlations between measurements are considered, a smoothing function can be used for interpolation. Garcia and coworkers developed an “inpainting” algorithm that performs a smoothing function to fill in missing data points from a data set of arbitrary dimensions.<sup>59,60</sup> The algorithm predicts missing values using a penalized least squares regression. The cost function to be minimized is shown in eqn (18.1), where  $\mathbf{y}$  is the sparsely sampled data set,  $\hat{\mathbf{y}}$  is the smoothed, interpolated data set,  $\| \cdot \|$  denotes the Euclidean norm,  $s$  is a parameter that controls the degree of smoothing, and  $\mathbf{P}$  is a penalty term that represents the degree of roughness in the smoothed data set, defined as  $\mathbf{P}(\hat{\mathbf{y}}) = \| \mathbf{D}\hat{\mathbf{y}} \|^2$  where  $\mathbf{D}$  is a tridiagonal matrix, which describes the distance between sampled pixels.

$$\mathbf{F}(\hat{\mathbf{y}}) = \| \hat{\mathbf{y}} - \mathbf{y} \|^2 + s\mathbf{P}(\hat{\mathbf{y}}) \quad (18.1)$$

The minimization of  $\mathbf{F}(\hat{\mathbf{y}})$  gives the linear system in eqn (18.2), where  $\mathbf{I}$  is the identity matrix.

$$(\mathbf{I} + s\mathbf{D}^T\mathbf{D})\hat{\mathbf{y}} = \mathbf{y} \quad (18.2)$$

To account for missing data points, a diagonal matrix  $\mathbf{W}$  is added to eqn (18.2) in the place of  $\mathbf{I}$ , where the diagonal elements  $W_{ii}$  are equal to 0 when  $y_i$  is missing and 1 when  $y_i$  is present.

$$(\mathbf{W} + s\mathbf{D}^T\mathbf{D})\hat{\mathbf{y}} = \mathbf{y} \quad (18.3)$$

Eqn (18.2) and (18.3) can be solved by left-matrix division. When sparsely sampled data are evenly spaced, a discrete cosine transform can be used to simplify and speed up the solution.



Other algorithms go beyond smoothing and look for non-local correlations in data sets. Bouman and coworkers have demonstrated model-based iterative reconstruction (MBIR) approaches for accurately performing inpainting.<sup>61</sup> In MBIR, forward models provide a mechanism for assigning the unsampled pixels, based in part on training using similar images.

Patterned sparse-sampling approaches provide a key step toward autonomous decision-making in imaging by enabling image reconstruction from subsampled measurement sets; however, these methods are limited in the sense that they do not necessarily sample the optimal pixels for an accurate reconstruction of the system. Reconstruction algorithms employed in fixed-pattern or random sparse sampling techniques provide a starting point for extension to autonomous laboratory systems, which aim to reconstruct descriptions of chemical space with maximal accuracy under the constraint of minimal sampling.<sup>59</sup> Such methods, referred to here as dynamic sampling methods, enable more rapid reconstruction of chemical space by deciding the optimal positions to sample within chemical space.<sup>62–64</sup>

### 18.2.2 Simplex Approaches for Autonomous Design of Experiments

Early work in autonomous experimental design focused on both chemical synthesis and optimizing chemical measurements through the simplex architecture of algorithm design. The simplex is a specific type of dynamic sampling strategy, where some probe of chemical space is mapped to a geometric representation with an arbitrary number of vertices and sides, a simplex. Beginning along one vertex of the polytope, which can be thought of as a discretized chemical space, a simplex algorithm is used to find the maximum value within the feasible region *via* walking along the edges of the shape in the direction of increasing values of the objective function.

The modified simplex algorithm was described in detail by Nelder and Mead as an algorithm for function minimization.<sup>65</sup> A function with  $n$  variables without constraints is minimized first by sampling  $n + 1$  points within the parameter space. Each sampled point is the vertex of the geometric simplex, giving rise to the method's name. To minimize the objective function, the output of each parameter set is first computed. The vertex with the highest valued objective function (*i.e.*, the worst performing set of parameters) is then reflected about the hyperplane of the remaining vertices, across the centroid of the hyperplane. Depending on whether the new point is an improvement over the previous vertex, the operations of expansion or contraction can be utilized, which shift the sampled position according to the local curvature of the objective function about the reflection. When iterated, this procedure will generate a simplex that converges about the minimum of the objective function, *i.e.*, the volume of the simplex will contract about the minimum point. Figure 18.3 illustrates the procedure for 2-dimensional optimization.

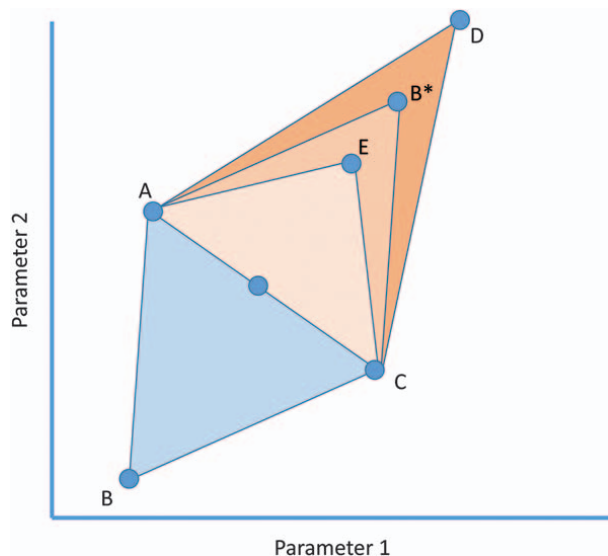


**Figure 18.3** A 2-dimensional simplex optimization step. The initial simplex is defined by the vertices ABC. The objective function is computed for each set of parameters, and B is found to be the worst input. The reflection  $B^*$  is generated about the centroid of the line segment AC. The algorithm can then either expand the simplex, accepting a new vertex D in place of  $B^*$ , or contract the simplex, accepting E in place of  $B^*$ , according to local curvature.

Beginning in the 1970s, simplex algorithms were applied to chemical automation, including the genesis of closed-loop automated synthetic platforms.<sup>64,66,67</sup> Other work utilized simplex algorithms to generate  $\text{H}_2\text{O}_2$  complexed with Ti(IV) in the presence of EDTA; automated injection of reagents was followed by measurement of the absorbance spectrum, with wait times added to assess the stability of the product.<sup>68</sup> The optimization of aerosol delivery in a flame spectrophotometer by Denton and coworkers serves as a simple example to illustrate how the simplex procedure can be utilized for automated analysis.<sup>66</sup> In that work, the physical position of the aerosol spray nozzle is the optimization space, with stepper motors controlling  $x$  and  $y$  position on orthogonal axes. The aim was to generate the maximum possible signal detected at the calcium emission line of 422.7 nm. Using Figure 18.3 as a template, consider the scenario where three unique sets of coordinates are used to measure calcium emission, represented by the vertices A, B, and C. Vertex B is found to result in the lowest amount of signal, so a new vertex is generated by reflecting across the line AC. The outcome of measurement at the new vertex  $B^*$  determines whether the simplex will be kept at this new location, expanded, or contracted. The mathematical details of this procedure are described fully in ref. 65. These initial simplex-based approaches to autonomous chemical experimentation use relatively simple algorithms, however they serve to illustrate the general architecture of dynamic sampling approaches to



autonomous experimentation, with one key difference. The simplex approach aims to optimize a single function, returning only the optimal value. In contrast, the dynamic sampling approaches described below reconstruct a full objective function using various interpolation and reconstruction algorithms. By mapping the full space of the objective function, dynamic sampling approaches can address more complex chemical problems, such as chemical classification.

### 18.2.3 Interpolation Algorithms for Dynamic Sampling

Dynamic sampling is a critical component in autonomous instruments, as it provides real-time feedback about the most beneficial experiment to be conducted with respect to the targeted goal. Dynamic sampling can enable instruments to advance in performance beyond automated, HT systems by increasing the value of each experiment.

Notingher and coworkers developed a dynamic sampling algorithm for Raman microscopy to determine the most informative sampling location by assigning a score to each unmeasured pixel in real time.<sup>69,70</sup> The score was calculated at each unsampled pixel as the difference between the values predicted by two different interpolation algorithms, a cubic spline, and a Kriging interpolation. The pixel location where the reconstruction algorithms differed the most was treated as the most informative pixel and then selected for subsequent measurement. Due to the integration of interpolation algorithms, this method showed an improvement in efficiency over random sampling. For biological tissue imaging, this method achieved up to 30 times reduction in the sampling time compared to raster-scanning, with sufficient spectral signal-to-noise ratio to identify individual tissue structures.

One strategy for further improving the performance of dynamic sampling is to use an algorithm that is trained prior to analysis. This approach, a supervised learning approach for dynamic sampling (SLADS) has been developed to improve the accuracy of dynamic sampling algorithms through training data that is specific to the sample under study.

### 18.2.4 A Supervised Learning Approach for Dynamic Sampling

The SLADS algorithm, developed by Bouman and coworkers, represents an illustrative case-study for understanding the general architecture of autonomous laboratory workflows.<sup>62–64</sup> SLADS uses a machine-learning-based algorithm to select the next most information-rich location to sample during real-time measurements. However, in contrast to other dynamic sampling algorithms, SLADS uses training data with a known ground truth to train the algorithm to calculate the expected reduction in distortion (ERD) for each sampling location. Leveraging this training, SLADS is capable of dramatically reducing the number of measurements required to obtain a

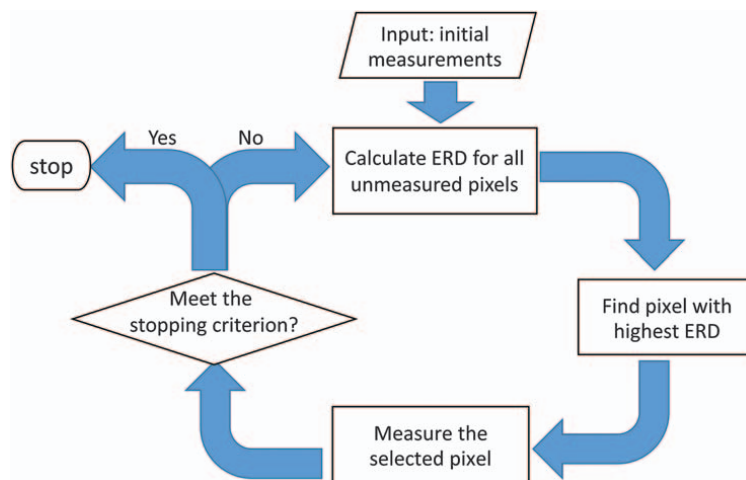


**Figure 18.4** The SLADS algorithm samples the unmeasured pixel with the highest ERD until the stopping criterion is met.

Adapted from ref. 54, <https://doi.org/10.1107/s160057751601612x>, under the terms of the CC BY 4.0 licence, <https://creativecommons.org/licenses/by/4.0/>.

reconstructed image without a significant loss in image quality. The theoretical framework of SLADS is demonstrated by the flow chart in Figure 18.4 and eqn (18.4)–(18.6).

The SLADS algorithm represents a 2D image as a matrix  $\mathbf{X}$ . In eqn (18.4),  $\mathbf{X}_r$  is a single pixel of the image at location  $r \in \Omega$ . The location of each of the  $k$  measured pixels are encoded within  $\mathbf{S} = \{s^{(1)}, s^{(2)}, \dots, s^{(k)}\}$ . Intuitively,  $\mathbf{Y}^{(k)}$  can be interpreted as storing all known measured information about the image.

$$\mathbf{Y}^{(k)} = \begin{pmatrix} s^{(1)}, X_{s^{(1)}} \\ \vdots \\ s^{(k)}, X_{s^{(k)}} \end{pmatrix}. \quad (18.4)$$

$\mathbf{Y}^{(k)}$ , as a  $k \times 2$  matrix of sampling location and measured values, can then be used to reconstruct an image  $\hat{\mathbf{X}}^{(k)}$  which is the best estimate of the ground truth image  $\mathbf{X}$ . SLADS is then employed to find the next sampling location, which maximizes the ERD,  $E[\mathbf{R}^{(k;s)} | \mathbf{Y}^{(k)}]$  given in eqn (18.5), where  $\mathbf{R}$  is the reduction in distortion. Maximizing the ERD results in reconstructing an image with the minimum amount of error relative to the true image.

$$s^{(k+1)} = \arg \max_{s \in \{\Omega \setminus \mathbf{S}\}} \left\{ E[\mathbf{R}^{(k;s)} | \mathbf{Y}^{(k)}] \right\} \quad (18.5)$$

Eqn (18.6) shows the calculation of  $\mathbf{R}$  resulting from measuring pixel  $s$ .  $\hat{\mathbf{X}}^{(k)}$  is the reconstruction result made by  $\mathbf{Y}^{(k)}$ , while  $\hat{\mathbf{X}}^{(k;s)}$  is the reconstruction made from  $\mathbf{Y}^{(k)}$  and  $X_s$ , the next sampled location.  $D(\mathbf{X}, \hat{\mathbf{X}}^{(k)})$  represents the

distortion between the ground truth image  $\mathbf{X}$  and the reconstructed image  $\hat{\mathbf{X}}^{(k)}$  with  $k$  measurements. In short, selection of an optimal new sampling location  $X_s$  will maximize  $\mathbf{R}$ , reproducing the true image with minimal distortion.

$$\mathbf{R}^{(k;s)} = D(\mathbf{X}, \hat{\mathbf{X}}^{(k)}) - D(\mathbf{X}, \hat{\mathbf{X}}^{(k;s)}). \quad (18.6)$$

As the ground truth image  $\mathbf{X}$  is not available during image acquisition, the ERD needs to be calculated from  $\mathbf{Y}^{(k)}$ . A function relating  $\mathbf{Y}^{(k)}$  to the ERD,  $f_0^s(\mathbf{Y})$ , is learned through supervised learning with a training set of known ground truth. The overall SLADS architecture thus updates the sampled locations stored in  $\mathbf{Y}^{(k)}$ , at each step, and the optimal next pixel location  $s^{(k+1)}$  is determined by a supervised learning algorithm trained to maximize the ERD.

### 18.2.5 SLADS for Raman Hyperspectral Imaging and X-Ray Diffraction Imaging

In recent studies, SLADS has shown broad application in point-wise imaging techniques such as confocal Raman microscopy, synchrotron X-ray diffraction imaging, and SEM. Simpson and coworkers implemented SLADS into confocal spontaneous Raman imaging, which was an early use of a machine learning approach for sparse sampling Raman imaging.<sup>52</sup> Integration of SLADS into the feedback for beam positioning enabled fully autonomous control over the selection of location and data acquisition. By using this approach, chemical images of pharmaceutical materials were acquired with >99.5% accuracy from 15.8% sampling, representing a ~6-fold reduction in measurement time compared to conventional raster scanning methods.

The SLADS algorithm was designed to select optimal sampling locations within images, while each pixel in a Raman image included a Raman spectrum with thousands of elements. As such, utilization of SLADS with Raman was enabled by preprocessing and classification of acquired Raman spectra to identify the chemical composition of the sample measured at specific locations. SLADS was then able to select the next pixel based on the greatest uncertainty in its predicted class. Classification was conducted by combining two supervised learning algorithms: linear discriminant analysis (LDA) and support vector machine (SVM).<sup>71,72</sup> LDA was performed for initial dimensional reduction, followed by SVM for classification by constructing optimal hyperplanes in data space to separate different clusters of data points. The SLADS algorithm was iterated until the maximum ERD of the reconstructed image converged below a threshold.

Simulated random sampling experiments were performed to compare the performance and efficiency of SLADS with other alternative sparse sampling methods. Figure 18.5D shows the image reconstruction error for random sampling and SLADS; the error achieved with random sampling was 4.65%

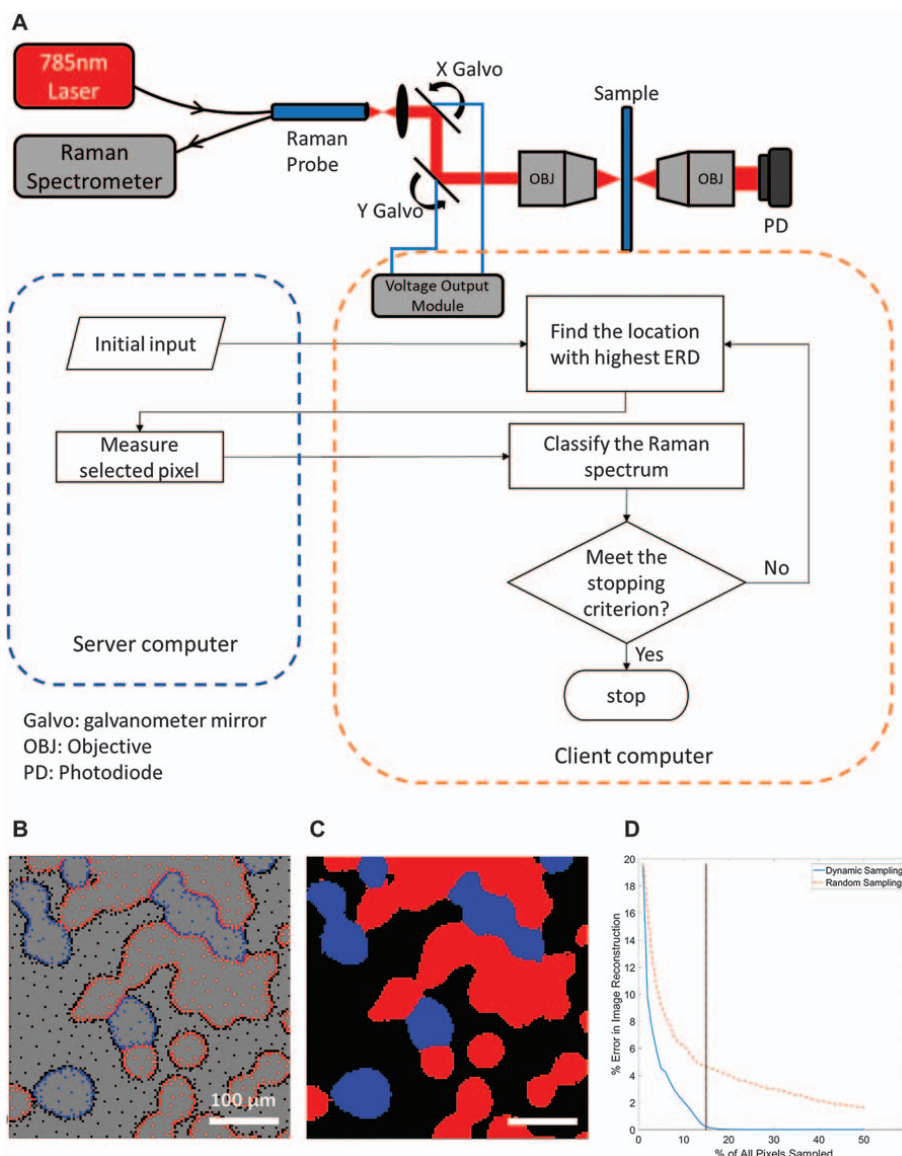


**Figure 18.5** Raman hyperspectral imaging with SLADS. (A) Instrument schematic showing a Raman microscope with a dual-galvo scan mirror pair. SLADS experiments were carried out through automated control of the mirror pair to position the laser beam at the pixel with the highest ERD. (B) Dynamically sampled image after classification at each sampled pixel. (C) Reconstructed image using trained SLADS algorithm. (D) Plot comparing reconstruction error between random sampling and dynamic sampling. Adapted from ref. 52 with permission from American Chemical Society, Copyright 2018.

with a 15% sampling rate, which was 20 times higher than the error with SLADS. Most incorrectly classified pixels obtained from random sampling were located at the boundaries of the sample particles in different classes. From an image analysis perspective, these boundaries can be considered to contain high spatial frequency information compared to other positions in the image, which means the boundaries are the most ambiguous and informative positions for the measurements. Random sampling does not adjust its measurement density according to the different spatial frequency at different positions, which significantly reduces its efficiency. SLADS adjusted the measurement density and selectively measured more pixels with higher spatial frequency information, enabling image reconstruction with a much lower error percentage than is achievable *via* random sampling with the same sampling rate.

Simpson and coworkers also implemented the SLADS algorithm with synchrotron X-ray diffraction experiments, which significantly reduced both dose and measurement time due to crystal positioning.<sup>54</sup> Crystal centering is required for macromolecular diffraction at synchrotron facilities, with X-ray diffraction mapping growing in popularity as a mechanism for localization. In X-ray raster scanning, diffraction is used to identify the crystal positions based on the detection of Bragg-like peaks in the scattering patterns. However, this additional X-ray exposure may result in detectable damage to the crystal prior to data collection. SLADS reconstructed the X-ray image with a 31% sampling of the total volume and only 9% of the interior of the crystal, greatly reducing the X-ray dosage on the crystal. When implemented into the beamline at Argonne National Laboratory an acceptable reconstruction was obtained with 3% of the image sampled corresponding to approximately 5% of the crystal. Dynamic sampling is well-matched to problems in which the cost of single-pixel acquisition limits the overall imaging time, consistent with diffraction imaging described herein. The cost here is not only in measurement time but also in sample integrity through X-ray induced damage.

SLADS is a powerful tool to accelerate 2D imaging, but extension to higher dimension remains to be demonstrated. Conceptually, dimensionality can be extended most trivially by incorporating time-domain information or a third spatial dimension. Adding in time-dependent changes in chemical composition adds another layer of complexity to these measurements. However, the curse of dimensionality makes higher dimensional reconstructions more difficult to solve. As dimensionality increases, the fast growth in the volume of measurement space also increases the data sparsity. To obtain a reliable statistical significance, the amount of data should increase exponentially with dimensionality. Furthermore, dimension reduction approaches also become increasingly challenging, either from a need for more training data to achieve the same resolution in projection onto a lower-dimensional space, or by covariance obfuscating dimension reduction. Therefore, a key step in facilitating extrapolation to higher dimensions is the ability to generate robust dimension reduction techniques

and classifiers capable of overcoming these challenges for autonomous decision-making. Consequently, understanding where and how these machine learning methods fail will facilitate the expansion of autonomous measurement methods to higher dimensions, as described in greater detail in Section 18.3 on adversarial attack strategies. However, before strategies for improving classifiers are considered, the following discussion surveys dynamic sampling methods used to map more complex chemical spaces in cellular biology and materials science.

### 18.2.6 Noniterative Dynamic Sampling for Autonomous Design of Experiments

One example of dynamic sampling applied to a complex chemical space was performed by King and coworkers who built a “Robot Scientist” named “Adam” that could generate and test hypotheses in functional genomics space.<sup>73</sup> Adam was designed to operate almost completely autonomously while measuring growth rates of microbial samples. In this work, the robot was applied to determine the genes that encoded some of the enzymes in a yeast organism, *S. cerevisiae*. Adam used prior knowledge about the functional genomics of *S. cerevisiae* from a database to select the most informative experiments to perform. Adam generated 20 hypotheses about the connections between 13 pairs of genes and enzymes (e.g. gene X encodes enzyme Y). After performing the experiments and analyzing the data, Adam confirmed 12 of the 20 hypotheses (with  $P < 0.05$  for the null hypothesis). Researchers confirmed some of Adam’s results by expressing the proteins from the genes that Adam concluded to be encoding the yeast enzymes. Manual enzyme assays with the expressed proteins confirmed three of the 12 conclusions, while review of the scientific literature provided strong evidence for six conclusions and revealed a possible error in one conclusion made by the robot.

The key innovation in the development of Adam was the integration of models, databases, and software to make this autonomous genomics experiment possible. A logical model, designed with metabolites as nodes and enzymes as connections between nodes, was used to encode knowledge about the metabolism of *S. cerevisiae*.<sup>74</sup> Information connecting genes with the proteins they encode was obtained from a bioinformatics database, which in turn informed the hypothesis generating software used by Adam. As shown in Figure 18.6, the software operated in the following stepwise fashion,: 1) find all reactions in the model of *S. cerevisiae* that are orphans (enzyme is not linked to a known gene), 2) determine which of these reactions would affect cell growth, 3) find the enzyme commission (EC) class of these reactions, 4) find the genes that express enzymes in the same EC class in other organisms, 5) find genes in *S. cerevisiae* with similar sequences to those in other organisms 6) make hypotheses linking genes with orphan enzymes. Additional software was used for experimental design, laboratory automation, and data analysis.



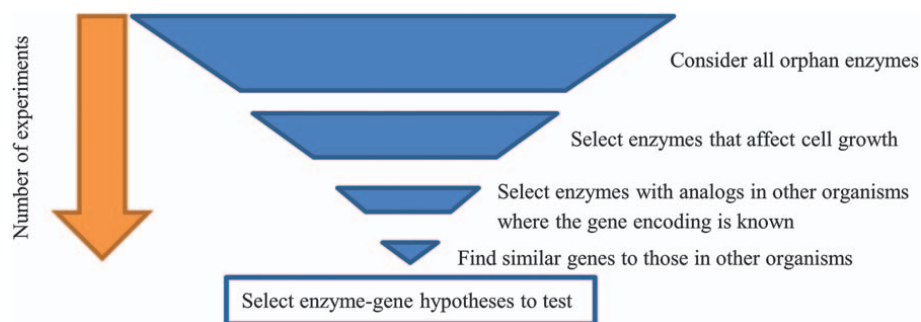


**Figure 18.6** Diagram of the dynamic sampling framework used in Adam. At first, all known orphan enzymes in a species are considered. Then, enzymes candidates are selectively eliminated based on a predetermined set of criteria (impact on cell growth, similarity to well-characterized enzymes in other organisms, *etc.*). The most critical experiments are selected based on the most probable hypotheses.

The experimental selection procedure that Adam used differs from other dynamic sampling methods in that it is noniterative. Adam is designed to synthesize knowledge from various databases and models to narrow down the set of possible experiments to the most informative hypotheses. In contrast, more recent work in dynamic sampling has explored the ability to generate *de novo* hypotheses from real-time experimental outcomes, as described elsewhere in this chapter (18.2.3–18.2.5, 18.2.7–18.2.9). The non-iterative framework of Adam is well-suited for the functional genomics questions at hand because of the large amount of information available in databases. Experiments in similar fields with high availability to databases could likewise benefit from a noniterative approach to dynamic sampling.

### 18.2.7 Active Machine Learning

Innovative work in autonomous biochemical research has been accomplished by Murphy and coworkers in their application of active machine learning to investigate the effects of active compounds on proteins within cells. Active machine learning is simply a strategy for experimental design based on observed data whereby the strategy adapts the experiment dynamically to account for real-time measurements.<sup>75–78</sup> Elsewhere in this chapter, we refer to active machine learning as dynamic sampling. In their first publication, Murphy and coworkers tested their active machine learning algorithms with simulations and experimental results of drug activity on gene expression.<sup>79</sup> The active machine learning process presented in this work is described in Figure 18.7. (A) The experiments are codified by target and condition. (B) Samples are clustered based on the phenotype revealed by experimental measurements. (C) Correlations between targets and conditions are identified based on the phenotypic distributions. (D) The next set of experiments is chosen based on gaps in a predictive model. Steps B–D are repeated until a stopping condition is met.

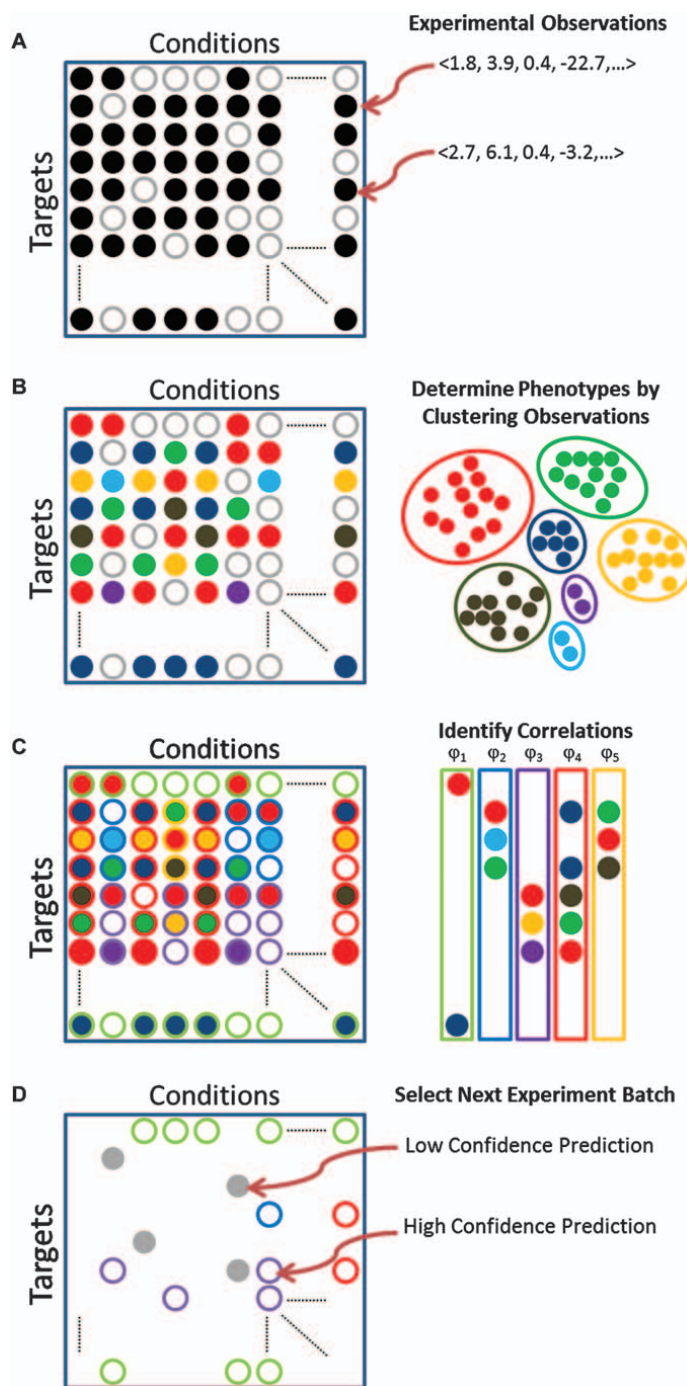


**Figure 18.7** The active machine learning process described by Murphy and coworkers. (A) Samples are codified by targets and conditions (B) Samples are clustered into phenotypes based on experimental observations. (C) Correlations are identified between target, condition, and phenotype. (D) The next set of experiments is chosen.

Reproduced from ref. 79, <https://doi.org/10.1371/journal.pone.0083996>, under the terms of the CC BY 4.0 licence, <https://creativecommons.org/licenses/by/4.0/>.



A key component of this method, and every dynamic sampling method, is the underlying predictive model that informs future measurements. In this work, the predictive model comprised a set of distributions that described the phenotypic dependence on targets and conditions. The model was constructed using clustering algorithms, which classified observations into phenotype groups. These algorithms also identified correlations between measurements and produced distributions, which described the correlations and collectively made up the predictive model. Greedy Merge and B-Clustering algorithms were used in this work. In this active machine learning method, the next experiment is chosen based on a score given to every unobserved experiment, based on the number of distinct predictions that can be made for each experiment. It is possible that one unobserved experiment could be described by more than one predicted distribution and therefore more than one predicted phenotype. The experiments for which the model had the most predicted phenotypes were assumed to be the most informative experiments to perform and were selected for subsequent analysis.

In their second publication, Murphy and coworkers integrated their active learning algorithm into an instrument to enable autonomous science in a real-time experiment.<sup>80</sup> They investigated the effect of 48 chemical compounds on the subcellular localization of 48 proteins. Experiments were performed with an automated fluorescence microscope, an automated liquid handling robot for transferring cell culture and chemical compounds, and automated image analysis software. 48 different clones expressing different EGFP-tagged proteins were generated and treated with one of 48 different compounds. The active machine learning algorithms guided the instrument in real-time to select the most informative protein-drug pair for the next experiment, based on prior results. Cells were imaged using the fluorescence microscope six hours after the selected drug was added to the culture media. Subcellular localization of the EGFP-tagged protein was determined using an image analysis method which produced a vector representation for each cell describing the positions of protein and DNA stains relative to each other.<sup>81–84</sup> A predictive model was updated on the fly during data collection until a stopping criterion was met. At the end of the experiment, the autonomous instrument achieved a 92% accuracy with only 29% sampling of all possible experiments.

### 18.2.8 Dynamic Sampling for Materials Synthesis

Research in materials synthesis has also leveraged autonomous chemical measurement, as demonstrated by Maruyama and coworkers from the Air Force Research Laboratory, who developed an Autonomous Research System (ARES).<sup>85</sup> ARES optimized the growth rate of single-walled carbon nanotubes (CNTs) through the combination of an automated growth reactor, rapid *in situ* characterization, and an AI system. The system utilized an AI planner to iteratively propose new experiments in order to optimize CNT growth rate

without *a priori* knowledge of the underlying physical processes. CNTs were synthesized in each experiment by a chemical vapor deposition process in which the growth conditions were varied (temperature, pressure, and partial pressures of ethylene, hydrogen, and water vapor). A laser was used to simultaneously heat the sample and as the excitation source for Raman spectroscopy.<sup>86,87</sup> The change in intensity of a characteristic Raman band was used as the readout for CNT growth rate and the experimentally determined growth rate was used as the feedback mechanism for the ARES system in its objective to optimize CNT growth.

The ARES system used a random forest model to make predictions about the CNT growth rate for untested conditions. A random forest is a machine learning method related to a decision tree.<sup>88–91</sup> A decision tree is an algorithm designed to perform a classification or regression on a data set through a branching series of decision nodes, where the most discriminate feature is used to divide the data set into two subsets.<sup>92–94</sup> A random forest is simply a set of decision trees in which each decision tree is trained using a random subset of the training data and a random set of features to divide the data. The averaged response of all the decision trees in the random forest is used as the output of the algorithm. In this case, an initial set of 84 user-designed experiments was provided to the random forest model as a training set to enable operation in autonomous mode. The random forest model then predicted experimental conditions that would achieve the user-specified target growth rate. After each experiment, the random forest model was updated to account for the most recent results and the experiment with the closest predicted growth rate to the target was performed. This process was iterated until the difference between the predictions and the experimental measurements of the growth rate converged within the noise floor of the experimental results. Figure 18.8 shows SEM images of CNTs produced by the ARES system. The images show samples with CNT growth rates of a)  $500 \text{ s}^{-1}$ , b)  $3000 \text{ s}^{-1}$ , and c)  $16\,000 \text{ s}^{-1}$ . ARES was shown to design, execute, and analyze its own experiments 100 times faster than conventional experiments and represents an early demonstration of an autonomous research system in materials science.

### 18.2.9 Modular Architectures for Autonomous Design of Experiments

The preceding sections have focused on autonomous design of experiments where often only a single autonomous agent governs the process. In each case, a single measurement was conducted, which then provided feedback for the selection of the next best parameter set to sample. If multiple instruments are required to probe the chemical problem of interest, a central hub is needed to control communication between instruments, execution of experiments, evaluation of the objective function, and selection of the next experiments. Figure 18.9 illustrates one possible architecture that could be utilized for an autonomous laboratory.

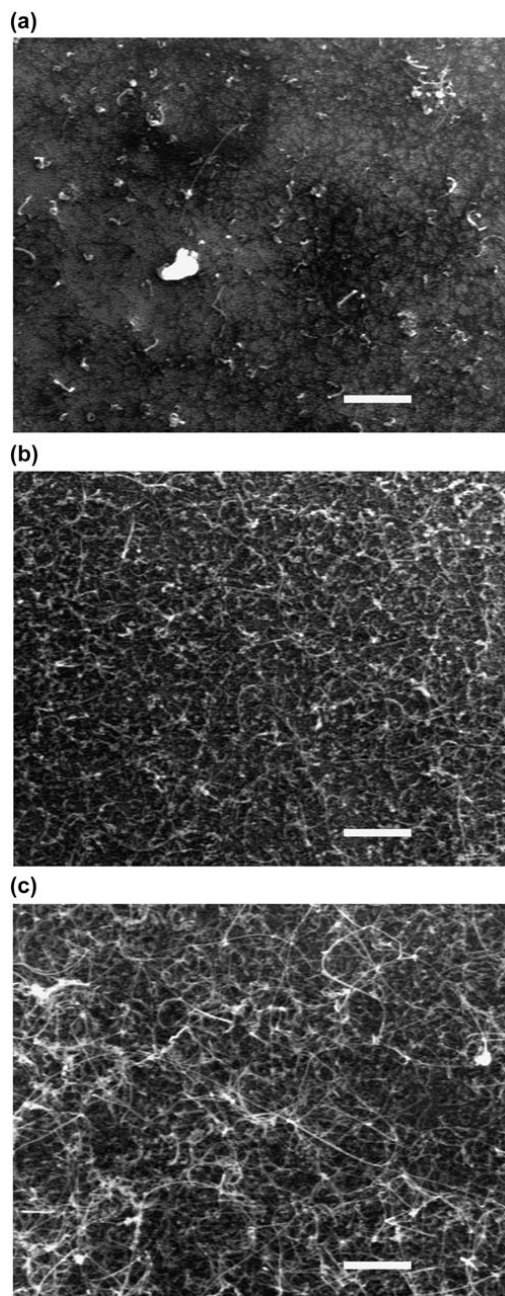


**Figure 18.8** SEM images of CNTs produced by the ARES system. Images show CNT growth rates of (a) 500, (b) 3000, and (c) 16 000 ( $\text{s}^{-1}$ ). Scale bar is 500 nm.

Reproduced from ref. 85, <https://doi.org/10.1038/npjcompumats.2016.31>, under the terms of the CC BY 4.0 licence, <https://creativecommons.org/licenses/by/4.0/>.

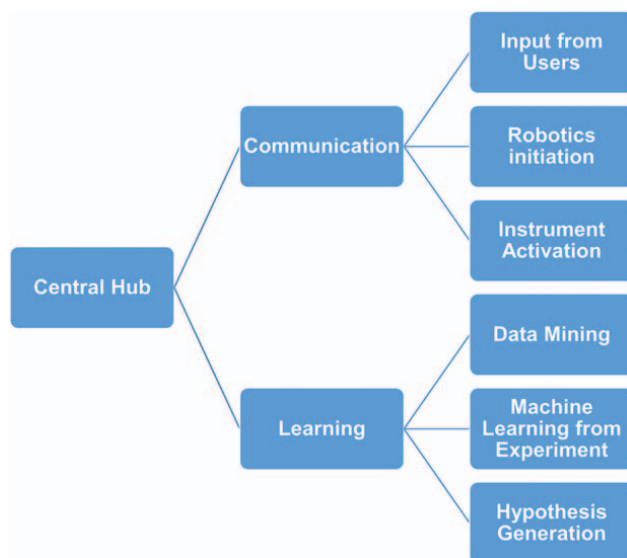


**Figure 18.9** Sample modular layout for the autonomous laboratory. Data handling is delineated into two general protocols: communication, where data are transferred from one module to another, and learning, where the hub utilizes available data to generate models. Each module on the far right is considered as a distinct element of the whole architecture, enabling the addition of new modules as necessary to add to existing capabilities.

To illustrate how the central hub might interface with the individual modules, consider a hypothetical scenario where the aim is to cook the most delightful omelet. In the described scenario, each module has both an input and output flow of information. First, the hub might access the internet with its data mining module, providing the input of targeted databases. The data mining module has been outfitted with several different data mining approaches, including an image and video analysis tool, which extracts cooking tutorials in video form, as well as text-learning modules that mine recipes from the internet. These modules individually access and learn key features of the data. The learned features are then passed back to the central hub, which relates the learned features to the “machine learning from experiment” module. This module can be used to generate a regression model predicting key input variables, such as the number of eggs, the temperature of the cooking vessel, amount of salt to add, time of cooking, *etc.* This module is distinct from the data mining module, as it can follow an active learning/dynamic sampling architecture where subsequent information gathered from experiment is incorporated. The regression model is fed back to the hub, and the hypothesis generation module is then called in to predict the set of parameters for the optimal omelet. With the predicted set of parameters, the hub must then

communicate to activate the robotics that control the cracking of eggs, the beating of eggs, the addition of other ingredients, *etc.* Each robotic action is accompanied with an activation of the module, initiating the task, and successful execution of the programmed motion will return completion back to the hub to initiate each subsequent robotic motion. In this example, the beginning of the cooking process corresponds to the activation of the instrument. Once cooking has been completed, the hub receives a completion command. As the deliciousness of an omelet requires human testing, the hub can then prompt the user that the output is ready. Various factors relating to the quality of the omelet such as taste, temperature, mouthfeel, smell *etc.* can be requested as feedback from the user. This feedback, in turn, can be cycled from the communication module through the hub and back to the machine learning module to improve upon the model.

Recent progress on the front of multi-instrument integration in autonomous science has been made by Aspuru-Guzik and coworkers who have developed ChemOS, a software designed for operating autonomous laboratories.<sup>95,96</sup> ChemOS is composed of a set of modules or functions: (i) communication, (ii) databases, (iii) robotics, (iv) characterization, (v) learning, and (vi) analysis. The communication module enables interaction between ChemOS and researchers, while the learning module is designed to propose parameters for new experiments based on previous results. The module provides real-time feedback to suggest more informative experiments to efficiently investigate an application space. ChemOS has been applied to a diverse set of experiments, demonstrating the versatility of the software to solve problems in disparate fields.<sup>95,96</sup> Aspuru-Guzik and coworkers showed that ChemOS can map “color space” by experimenting with mixing dye solutions, learn “Tequila Sunrise space” to optimize cocktail taste based on feedback from researchers, and calibrate a robotic sampling sequence for direct-inject HPLC analysis. The flexibility of this modular framework for directing autonomous science suggests that it could be applied in a variety of research contexts.

Modular architectures to achieve the autonomous laboratory allow the integration of new experimental probes and models in a dynamic fashion. This is particularly powerful in the regime of “little data”, where individual measurements are costly or time-consuming. In scenarios where database information can be leveraged, the modular framework can enable model generation from previous experiments with continuous optimization afforded by dynamic sampling methods. Considering this, it is critical to note that for many chemical questions there is little existing data to build from, and consequently, machine learning methods can be limited in scope and application. The subsequent section will discuss existing methods in machine learning that have been leveraged to solve similar problems in image analysis, with emphasis on generative adversarial networks (GAN) and an illustrative linear analog.

## 18.3 Generative Adversarial Methods for Data-limited Training

The preceding section highlights the benefits of integrating pre-trained machine learning tools to aid in optimally reducing the number of samples required to inform a chemical decision and support autonomous design of experiments. In contrast, the central focus of this section moves back one level in the pipeline, focusing on methods to optimally train machine learning and conventional chemical classification tools for these tasks and others when confronted with limited or expensive training data. As one example, the dynamic sampling method described in Section 18.2.5 used Raman spectral analysis to determine composition at each spatial location in an image. The algorithm used LDA for dimension reduction and SVM for identification of classification boundaries, both of which required relatively large training sets to optimize. Similarly, the large number of parameters available for optimization in an artificial neural network (ANN) generally cannot be stably trained with “small data” inputs, exacerbating further the challenges in leveraging machine learning tools in data-sparse scenarios.

Generative adversarial strategies have had great success in addressing many of the most insidious training challenges in data-limited scenarios. Adversarial approaches support the generation of additional training data that are ideally randomly produced from a similar underlying probability density function (pdf) as the raw inputs. If the data were truly from an identical pdf, they would be indistinguishable from the results obtained from additional experimental measurements. In practice, the utility of the generated inputs hinges on the degree to which the small data inputs capture the underlying features of the pdf and how well those can be extracted algorithmically. The goals of this section are threefold: i) review previous successes using adversarial attacks and general adversarial networks in nonlinear problems (*e.g.*, image and speech recognition) as a foundation for extension to chemical applications, ii) improve the understanding of operations “under the hood” in adversarial attacks by devising analogous effects in more intuitive models based on simpler linear spectral analysis, and iii) lay the foundation for integration of generative adversarial attacks in linear spectroscopic analysis to improve chemical classifiers.

### 18.3.1 Review of Generative Adversarial Networks in Image Recognition Applications

ANNs are designed for optimal performance when trained with large input databases. The numerous weights within each hidden layer in an ANN collectively comprise a large number of free adjustable parameters, which in turn generally requires large volumes of training data to reliably train. In the absence of sufficient training data, the disparity between dimensionality in



parameters and inputs generally results in poor statistical confidence in the assignment of an ANN output from undertraining. In brief, limited data sizes do not provide sufficient constraints to prevent underdetermination in the neural network architecture. In such situations, neural networks trained with limited training data can be prone to erroneous results and/or low confidence in classification of testing data.

Even when training with relatively large data sets, residual noise contributions manifested within the ANN weights invariably remain. In such cases, dimension reduction followed by classification is susceptible to hidden “traps” in classification. The susceptibility of machine learning methods (e.g., convolutional neural networks) to spurious changes in input data has been reported in multitude.<sup>97–101</sup>

Generative adversarial strategies work by first identifying potential weak points in an ANN through targeted attacks, and then fortifying the ANN by training it to recognize these attacks. This process is iterated, with the generated “attack” data serving to further refine and train the ANN as a surrogate for large volumes of genuine experimental input data. This iterative two-step process is arguably most well established in neural networks for image recognition, the first step of which is identifying weak points by producing attacks designed to induce image misclassification.

Prior to considering attack strategies in machine learning methods, it is useful to consider how human perception can be influenced by the way image data are portrayed to examine the interplay between a presented set of data and subsequent interpretation. Figure 18.10 shows an example of an optical illusion (Adelson’s checker-shadow), designed specifically to attack human neural networks.<sup>102,103</sup> In Adelson’s shadow, a checkerboard pattern is overlaid with a cylinder that appears to cast a shadow across the checkerboard. The shadow itself is used to selectively darken several squares in the checkerboard; inspection of the left image yields a perception that the squares A and B are of distinctly different brightness, when in reality A is precisely the same shade as square B. Optical illusions demonstrate how a designed pattern can attack decisions derived from a human neural network; subtle perturbations to the input image can result in interpretation of the image with incorrect conclusions.

Adversarial attacks operate in a qualitatively similar manner, but with dramatically different quantitative outcomes in selecting the optimal attacks. Specifically, residual noise within the neural network weightings arising from finite training dataset sizes often serves as a “handle” for launching attacks in neural network classifiers. As such, the malicious perturbation is often engineered to be challenging to identify by naïve human inspection, but with profound impacts on classification by a machine learning algorithm.<sup>104</sup> Figure 18.11 demonstrates an example of adversarial attack in handwriting recognition, in which the effect of the attack can be easily rationalized in hindsight.<sup>105</sup> Changing a few spots in the handwriting input can cause the number 1 to be identified as the number 4. Close examination of this example reveals that the added dots to the image

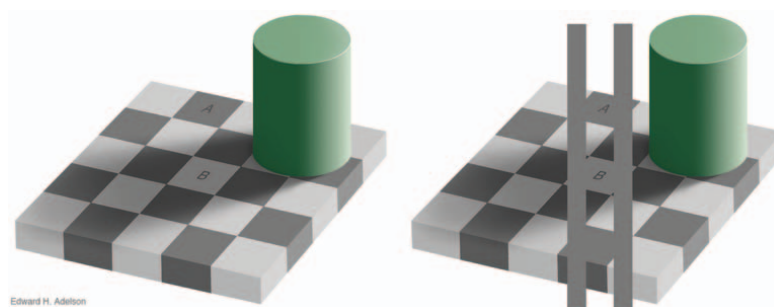


**Figure 18.10** An example of visual illusion: Adelson's checker-shadow. In the left image, area B looks brighter than area A. In the right image, two gray bars were added as a reference revealing that area A and area B have the same brightness.

Reproduced with permission from E. H. Adelson, In *On seeing stuff: The perception of materials by humans and machines*, Conference on Human Vision and Electronic Imaging VI, San Jose, Ca, Jan 22–25; Spie-Int Soc Optical Engineering: San Jose, Ca, 2001; pp. 1–12.

	Input	Model Activations	Output
Legitimate			1
Adversarial			4

**Figure 18.11** Adversarial attack on handwriting recognition. An adversarial sample (bottom row) is produced by slightly altering a legitimate sample (top row) in a way that forces the model to make a wrong prediction, whereas a human would likely correctly classify the sample.

Reproduced with permission from N. Papernot, P. McDaniel and I. Goodfellow, Transferability in machine learning: from phenomena to black-box attacks using adversarial samples. *arXiv preprint arXiv:1605.07277* 2016.

could, in fact, be connected with lines to form a shape of a 4 – the neural network here is weighting those particular pixels with enough importance to outweigh the lack of true connections, generating the full shape of a 4. However, as the dimensionality of the image increases, retrospective rationalization of the perturbations can be increasingly challenging to intuit.

When discussing adversarial attacks, it is useful to distinguish between attacks on models where the architecture and weights of the trained classifier are known prior to the design of an attack *versus* cases in which they are unknown. Attacks on networks where the attacker has full knowledge of the classification structure and weights are known as white box attacks, in



which cases the optimal perturbations can typically be calculated analytically to efficiently fool classifiers for given inputs and targets. The strategies for attack can vary widely, targeting different image aspects. In one of the most common implementations, back-propagation of the neural network allows determination of the steepest gradient toward a classification boundary, corresponding to the smallest perturbation required to induce a given misclassification. In contrast, attacks, where only the classification outcome is accessible to the attacker, are known as black box attacks – such methods rely on optimization approaches to generate a perturbation to the input data to produce the desired classification outcome.

Illustration of a white box attack is shown in Figure 18.12, in which an optimized, subtle perturbation added to an image of a panda bear resulted in the GoogLeNet image classifier confidently misclassifying the image as a gibbon.<sup>106,107</sup> In this attack, the elements of the perturbation are equal to the sign of the elements of the gradient of the cost function with respect to the input, a method dubbed the fast gradient sign method. Intuitively this approach can be interpreted as identifying the direction of highest classification uncertainty and adding the minimal push to the input data  $x$ . The scaling factor  $\epsilon = 0.007$  is the magnitude of the smallest bit of an 8-bit image encoder after conversion to real numbers. Notably, this approach does not point the classifier to a specific outcome, but rather utilizes the full knowledge of the training cost function to minimally push the classifier to an incorrect conclusion.

In many cases, the analytical solution for optimizing an attack pattern is not known, for which the outcomes of the neural network for given inputs alone serve to inform the optimization of an attack. Such black box attacks add small perturbations to input data, test the classifier, and then iteratively optimize perturbations numerically to achieve a classification confidence subject to a cost function. Kevin Eykholt and coauthors illustrate an example of a black-box attack, in which perturbations were determined to induce misinterpretation of traffic sign images by image recognition algorithms.<sup>108</sup>

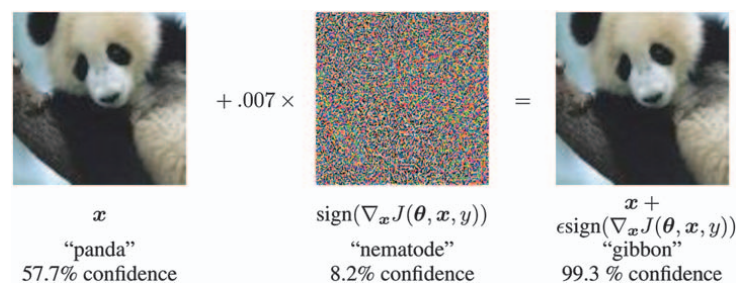


**Figure 18.12** A demonstration of fast adversarial example generation applied to GoogLeNet on ImageNet. By adding an imperceptibly small perturbation, GoogLeNet’s classification of the image is significantly altered. Reproduced with permission from I. J. Goodfellow, J. Shlens, and C. Szegedy, Explaining and Harnessing Adversarial Examples. *arXiv e-prints* (2014).

In this black-box attack, they were able to induce misclassification of a stop sign as a 45 mph speed limit sign through perturbations difficult to rationalize upon human inspection. Without knowing the neural network behind the traffic sign classification, the attack pattern sampled from a distribution that modeled physical dynamics (in this case, varying distances and angles), and used a mask to project computed perturbations to a shape that resembled graffiti. This attack fooled two convolutional neural networks, LISA and GTSRB-CNN with over 85% confidence.

Despite the success of these adversarial attack strategies in ANNs, the inherent nonlinear nature of many ANN architectures complicates intuitive rationalization of both the intrinsic susceptibilities to attack and origins of the optimized attack patterns. The greatest strengths in ANNs arguably lie in their abilities to exploit underlying patterns through coupled but highly nonlinear transformations. However, the intrinsic nonlinearities associated with the pattern-matching in ANNs greatly complicate meaningful mapping onto more intuitive and tractable linear frameworks more commonly used in spectral analyses. It is challenging enough to intuit the strengths and weaknesses of an ANN in general, while it is more challenging to interpret a numerically generated adversarial attack thereof.

### 18.3.2 Illustrative Linear Example of Adversarial Attacks: Adversarial Spectroscopy

Many of these training challenges in ANNs under data-limited conditions have direct analogs in classical, linear dimension reduction methods, providing a significantly more intuitive and tractable context for interpreting the origins of these potential numerical instabilities. When used for classification of images, sounds, or spectra, neural networks can be viewed as dimension reduction methods, in which high-dimensional objects in image or spectral space result in low-dimensional classified outputs. As such, linear methods for dimension reduction such as principal component analysis (PCA) and LDA can potentially serve as simple ANN surrogates for interpreting the design and execution of adversarial attacks, which is the primary subject of this section.

As an illustrative example, it is useful to compare dimension reduction/classification by ANNs with conventional LDA for spectral classification. In LDA, supervised inputs are used to identify a new lower-dimensional space designed to maximize the resolution between the classified inputs. Maximizing the resolution is mathematically analogous to maximizing the Fischer linear discriminant. For a given projection in spectral space  $\mathbf{w}$ , the corresponding value of the Fisher discriminant  $J$  is given by the eqn (18.7), in which the matrices  $\mathbf{S}_w$  and  $\mathbf{S}_B$  correspond to the within-class and between-class variance/covariance matrices, respectively.

$$J = \frac{\mathbf{w}^T \mathbf{S}_B \mathbf{w}}{\mathbf{w}^T \mathbf{S}_w \mathbf{w}} \quad (18.7)$$

Mathematically, the direction in spectral space that maximizes the value for  $J$  can be found by solving the eigenvector/eigenvalue problem in eqn (18.8).

$$J\mathbf{w} = \mathbf{S}_w^{-1} \mathbf{S}_B \mathbf{w} \quad (18.8)$$

Upon extension to multiple classes, the vector  $\mathbf{w}$  can be replaced by a matrix  $\mathbf{W}$  to produce sets of eigenvectors corresponding to the reduced dimensional coordinates generated by LDA.

The matrix inversion step in eqn (18.8) provides a source of potential instability in data-limited applications, directly analogous to data-limited training of ANNs. Specifically, the  $\mathbf{S}_w$  matrix is only nonsingular and formally invertible when the number of training spectra is greater than the length of a given spectrum. When training data are limited and this criterion is not met, direct application of LDA with numerical methods to estimate the matrix inversion operation results in poorly constrained selection of dimensions highly prone to “overfitting”, in which noise contributions within the data contribute significantly or dominate the selection of dimensions to maximally resolve the classified data. Even when the number of training data exceed the dimensionality of the spectral space, the matrix  $\mathbf{S}_w$  is generally still not sufficiently overdetermined to remove significant contributions from noise in the loading vectors used for dimension reduction. As such, spurious noise contributions can potentially result in misclassification or classification with low statistical confidence. In LDA, this noise-susceptibility is apparent upon inspection of the “loading plots”, which correspond to the directions in spectral space that each spectrum is projected onto in order to generate the corresponding position in LDA-space. Representative loading plots shown for a simulated training set of Raman spectra just large enough (1424 spectra) to satisfy the nonsingularity requirement are shown in Figure 18.13, clearly indicating significant contributions of residual noise to the classifiers designed to maximize the resolution between classes. As expected, increasing the number of simulated Raman spectra in the training set by about two orders of magnitude (160884 spectra) significantly reduced the noise in the LDA loading plots.

The benefits of generative adversarial approaches to enable chemical analyses with limited data hinge on the success of the adversarial attacks in identifying points of vulnerability in classifiers. In this illustration of adversarial spectroscopy, a perturbation to the initial spectrum  $\delta$  is added to the initial sample spectrum  $\mathbf{x}_s$  to produce the perturbed spectrum  $\mathbf{x}' = \mathbf{x}_s + \delta$ . The cost function to optimize the attack is given in eqn (18.9) as the sum of two terms. The first term,  $\|\mathbf{D}(\mathbf{x}_s + \delta - \mu_t)\|^2$ , minimizes the squared deviation of the perturbed spectra  $\mathbf{x}_s + \delta$  and the target spectrum  $\mu_t$  in LDA space. The transform matrix  $\mathbf{D}$  maps the difference in spectral space  $\mathbf{x}_s + \delta - \mu_t$  to LDA space, driving the input data to the location of the target class mean and inducing misclassification. The second term minimizes the overall magnitude of the perturbation  $\|\delta\|^2$ , constraining the overall perturbation to a small magnitude and reducing the visual difference between the initial and

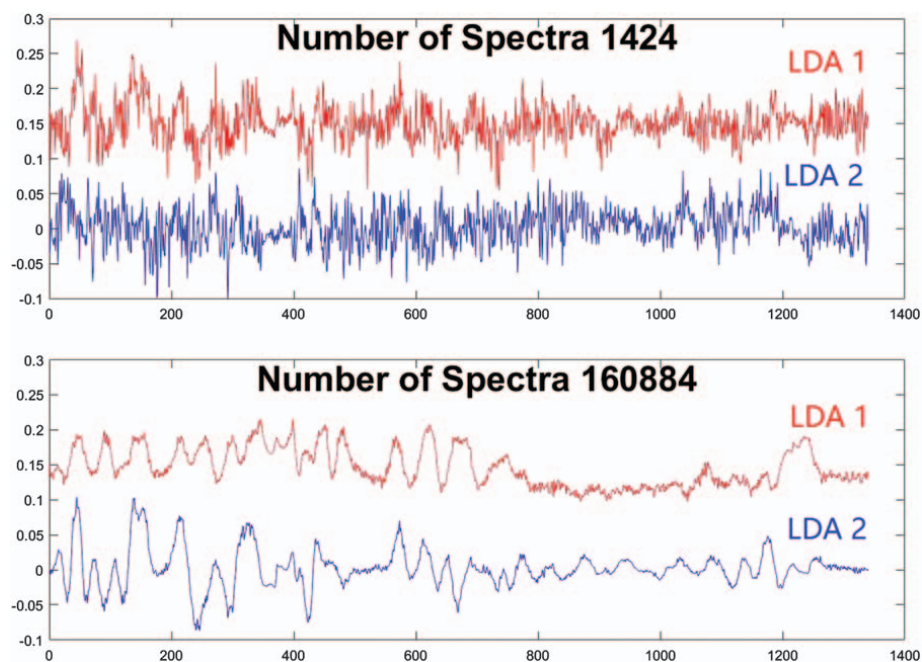


**Figure 18.13** Comparison of LDA loading plots with different amounts of simulated training spectra. An original set of 267 experimental Raman spectra are supplemented with simulated spectra from the same statistical distribution. As expected, noise is significantly reduced when performing LDA with a greater number of training spectra.

attacked spectrum. In other words, the first term fools the classifier, while the second term fools the human. The scaling parameter  $\beta$  allows for empirical adjustment of the importance of subtlety;  $\beta=1$  was used for this study.

$$\hat{\delta} = \arg \min_{\delta} [\|D(\mathbf{x}_s + \delta - \mu_t)\|^2 + \beta \|\delta\|^2] \quad (18.9)$$

The large apparent contributions of noise to the loading plots in LDA-based dimension reduction suggests that a significant contribution to the chemical classification includes contributions from spurious noise in the training data, creating potential susceptibilities for adversarial attacks. Incorporation of spurious noise within the dimension reduction operation in LDA is directly analogous to “overfitting” in ANNs, in which classification becomes overly dependent upon random features (including spurious noise) within the training data that serve as toeholds for adversarial perturbations. While in principle, this intrinsic susceptibility to attack could be minimized through increases in the size of the training set, practical limitations can complicate such approaches, particularly when data are relatively expensive or time-consuming to obtain.

An example in Figure 18.14 illustrates the vulnerability of a Raman spectral classification informed by LDA. An initial spectrum (top trace in **A**) clearly corresponds to Class I (middle right of **B**), both by its visual similarity to the Class I mean spectrum and by its corresponding position in LDA-space. Addition of a perturbation to the spectrum according to the cost function in eqn (18.9) results in minor visual changes in the spectrum (middle trace in **A**), but quite dramatic reclassification to Class II (bottom of **B**), with >95% confidence based on the position in LDA-space.

This susceptibility to adversarial perturbation is an intrinsic consequence of the dimension reduction by projection onto the LDA coordinates; there is an infinite set of possible spectra that correspond to the same position in LDA-space. Correspondingly, innumerable perturbations to any initial spectrum can shift its position to the target location in LDA-space. The definition of the cost function selects the one spectrum among this set that corresponds to the optimal perturbation (in this case, the perturbation with the smallest squared magnitude). For this cost function, the presence of residual noise within the LDA-coordinates preferentially selects many small “nudges” over more obvious large perturbations at a small number of wavelengths. Most significantly, the perturbations generally do NOT result in spectra with peaks similar to those expected in the target class.

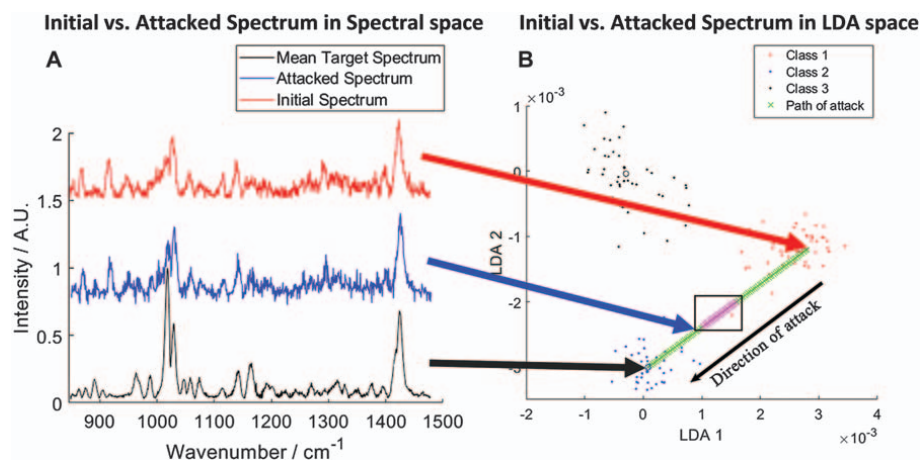


**Figure 18.14** Illustration of an adversarial spectroscopic attack (**A**) An initially unperturbed spectrum (top) is attacked, generating the attacked spectrum (middle). The attacked trace is then classified as the target spectrum (bottom). Note the attacked spectrum (middle) does not bear a significant spectral resemblance to the target class (bottom). The classifier is fooled while human inspection will not detect the perturbation. (**B**) Demonstration of an adversarial attack in LDA space. The attack spectrum is moved from class 1 (middle right) to class 2 (bottom left) by adding small amounts of noise to the original spectrum. The boxed region denotes the area of greatest uncertainty for classification.



The optimized perturbations shown in panel A of Figure 18.14 retained major spectral features of the original class while misclassifying with  $\geq 95\%$  confidence.

The vulnerability to adversarial attack inherent in many spectral classifiers illustrated in this section also presents opportunities for exploiting adversarial strategies to improve chemical classification algorithms. Potential benefits of defensive strategies for improving chemical classification algorithms are the primary subject of the next section.

### 18.3.3 Illustrative Example of Data Generation: Generative Adversarial Linear Analysis

The primary utility of adversarial spectroscopy is arguably in its potential for improving the general reliability of chemical classifiers. Training data for creating classifiers are necessarily finite resources, with any practical data set potentially susceptible to spurious or malignant misclassification. One promising avenue to address this vulnerability is through generative adversarial strategies in spectrochemical analysis, inspired by parallel successful implementation of GANs in image processing.<sup>109</sup>

A GAN is specifically designed to identify and shore-up potential weak-points in a given classifier through the generation of “fake” inputs (*e.g.*, images), followed by discrimination between real and fake inputs. GANs are typically deep neural networks comprised of two key components: a generator and a discriminator. Random arrays serve as inputs to the generator, which produces an output of fake inputs (*e.g.*, images) for the discriminator. Knowledge of the discriminator is used in training the generator to produce fake inputs through adversarial attacks that will be classified into target categories. Next, a new discriminator is produced capable of additionally distinguishing between real and fake inputs. This new discriminator is then used to train a new generator, and this adversarial back-and-forth is iterated until some convergence criterion is met. Through this process, the final discriminator exhibits substantial improvements against adversarial or spurious perturbations.

The success of GANs can be interpreted within the context of signal averaging. If we could devise a perfect generator, the output would produce spectra or images statistically identical to genuine measurements, which in turn, could be used for noise suppression in the discriminator as illustrated in Figure 18.15. Stated differently, the perfect generator captures all the complex and generally nonlinear relationships associated with the underlying pdf describing the experimental measurements. Just as a Gaussian pdf describing the generation of many thousands of measured inputs can be described by just two parameters (mean and variance), the generated inputs to a discriminating neural network can be fundamentally described by lower-dimensional latent-space parameters. In neural networks, the functional form for the pdf and the nature of the underlying latent parameter-space are

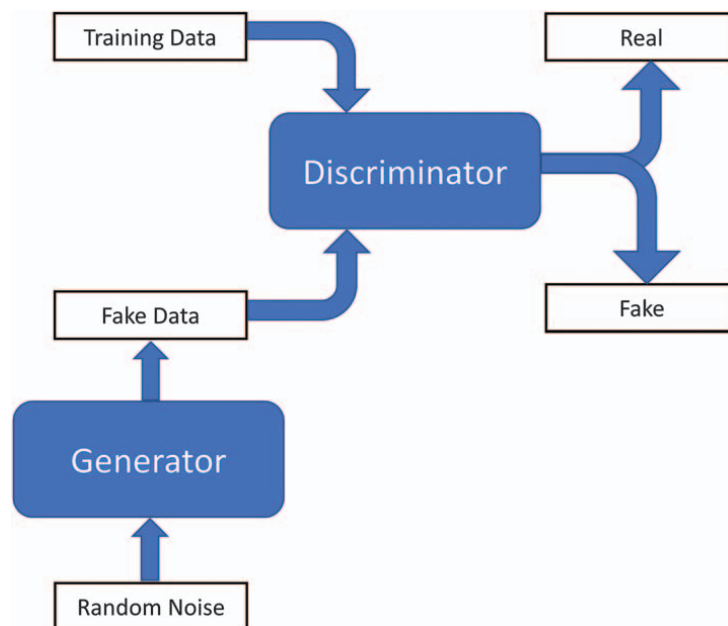


**Figure 18.15** Workflow of a GAN. The generator is trained to produce fake data that will “fool” the discriminator while the discriminator is trained to distinguish fake data from real data. By forcing the generator and discriminator to compete, the discriminator will become more robust.

generally not known or even analytically derivable, but rather are learned through training of the generator.

The authors expect adversarial spectroscopic approaches to ultimately result in analogous improvements in chemical classification upon integration into future generative adversarial architectures. A conceptual overview of how such an approach could be implemented is envisioned in Figure 18.16. Using the results described in Figure 18.14 as an example, measured spectral data first undergo dimension reduction for noise suppression and to aid in the definition of classification boundaries (indicated by the ellipses in the left-most plot). Randomly generated initial spectra (*e.g.*, Gaussian distributed random values) can serve as starting points for launching adversarial attacks targeting one of the chemical classes. Projection of these random initial spectra onto the reduced dimensional space is illustrated by the large ellipse in the middle plot. Using the cost function given in eqn (18.9), the attack minimizes the distance to the target in the reduced dimensional space, while simultaneously reducing the overall magnitude of the perturbation in the higher-dimensional spectral space. Next, a new set of loading plots for dimension reduction is determined that includes discrimination between the initial genuine data and the fake spectra generated by performing attacks on random initial inputs. Iteration

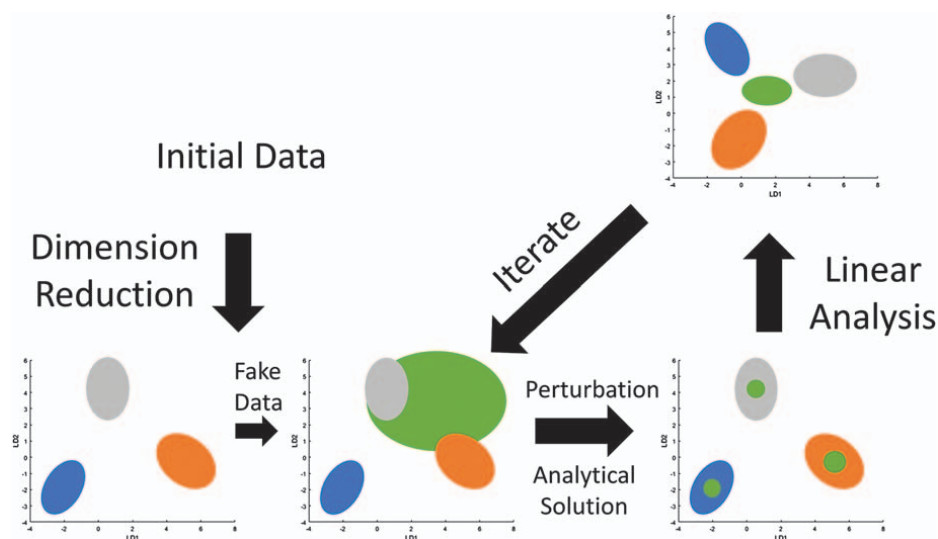


**Figure 18.16** The workflow of generative adversarial approaches in spectral classification involves the following conceptual steps: (i) initial data are analyzed by dimension reduction, (ii) “fake” data are generated in spectral space using random inputs and projected into this lower-dimensional space, (iii) each of the fake spectra is perturbed by an adversarial attack to induce classification into one of the target classes, (iv) a new dimension reduction operation is performed to separate the real and fake spectra. Steps ii–iv are then iterated to a desired level of convergence.

of this procedure has the potential to suppress noise contributions within the loading plots through mechanisms qualitatively similar to those arising from signal averaging. Furthermore, no explicit assumptions are necessary regarding the underlying pdfs describing the signal or noise in the measurements.

## 18.4 Conclusion

Recent advances in machine learning have opened exciting avenues for leveraging big data tools in small data applications. Individual chemical measurements can be time-consuming and practically difficult, or otherwise costly. To meet these challenges, several strategies were explored for minimizing the total number of measurements required to inform decision-making. In chemical imaging, sparse sampling strategies were shown to leverage intrinsic image compressibility to reliably “inpaint” composition within unsampled pixel locations. Coupling sparse sampling methods with models for predicting the most informative experiments enables dynamic sampling, in which the previous set of measurements dynamically informs the next sampling locations. Finally, recent advances in GANs for neural network training in data-limited scenarios were mapped to analogous



operations in linear classifiers, providing a route for understanding the mechanism of operation underpinning GANs and enabling extension of those concepts to more traditional linear algorithms for chemical classification.

## Acknowledgements

The authors gratefully acknowledge funding for the present work from the National Science Foundation through an NSF-GOALI award (No. CHE-1710475) and an NSF-CIF award (No. 1763896).

## References

1. X. W. Chen and X. T. Lin, *IEEE Access*, 2014, **2**, 514–525.
2. Q. C. Zhang, L. T. Yang, Z. K. Chen and P. Li, *Inform. Fusion*, 2018, **42**, 146–157.
3. L. Xu, J. S. J. Ren, C. Liu and J. Y. Jia, *Advances in Neural Information Processing Systems 27 (Nips 2014)*, **vol. 27**, 2014, p. 9.
4. F. Seide, G. Li, D. Yu and A. Int Speech Commun, *12th Annual Conference of the International Speech Communication Association 2011 (Inter-speech 2011)*, **vol. 1–5**, 2011, p. 444.
5. M. M. Najafabadi, F. Villanustre, T. M. Khoshgoftaar, N. Seliya, R. Wald and E. Muharemagic, *J. Big Data*, 2015, **2**, 1.
6. A. Khademhosseini, J. Yeh, G. Eng, J. Karp, H. Kaji, J. Borenstein, O. C. Farokhzad and R. Langer, *Lab Chip*, 2005, **5**, 1380–1386.
7. Y. Gao, P. Li and D. Pappas, *Biomed. Microdevices*, 2013, **15**, 907–915.
8. E. S. Park, A. C. Brown, M. A. DiFeo, T. H. Barker and H. Lu, *Lab Chip*, 2010, **10**, 571–580.
9. J. Kim, D. Taylor, N. Agrawal, H. Wang, H. Kim, A. Han, K. Rege and A. Jayaraman, *Lab Chip*, 2012, **12**, 1813–1822.
10. N. N. Ye, J. H. Qin, W. W. Shi, X. Liu and B. C. Lin, *Lab Chip*, 2007, **7**, 1696–1704.
11. A. Aharoni, K. Thieme, C. P. C. Chiu, S. Buchini, L. L. Lairson, H. M. Chen, N. C. J. Strynadka, W. W. Wakarchuk and S. G. Withers, *Nat. Methods*, 2006, **3**, 609–614.
12. J. C. Baret, O. J. Miller, V. Taly, M. Ryckelynck, A. El-Harrak, L. Frenz, C. Rick, M. L. Samuels, J. B. Hutchison, J. J. Agresti, D. R. Link, D. A. Weitz and A. D. Griffiths, *Lab Chip*, 2009, **9**, 1850–1858.
13. J. J. Agresti, E. Antipov, A. R. Abate, K. Ahn, A. C. Rowat, J. C. Baret, M. Marquez, A. M. Klibanov, A. D. Griffiths and D. A. Weitz, *Proc. Natl. Acad. Sci. U. S. A.*, 2010, **107**, 4004–4009.
14. A. Fallah-Araghi, J. C. Baret, M. Ryckelynck and A. D. Griffiths, *Lab Chip*, 2012, **12**, 882–891.
15. P. Y. Colin, B. Kintsjes, F. Gielen, C. M. Miton, G. Fischer, M. F. Mohamed, M. Hyvonen, D. P. Morgavi, D. B. Janssen and F. Hollfelder, *Nat. Commun.*, 2015, **6**, 1–12.

## Autonomous Science: Big Data Tools for Small Data Problems in Chemistry

16. J. Draper, A. J. Lloyd, R. Goodacre and M. Beckmann, *Metabolomics*, 2013, **9**, S4–S29.
17. T. Fuhrer, D. Heer, B. Begemann and N. Zamboni, *Anal. Chem.*, 2011, **83**, 7074–7080.
18. J. M. Buescher, S. Moco, U. Sauer and N. Zamboni, *Anal. Chem.*, 2010, **82**, 4403–4412.
19. W. Jian, M. V. Romm, R. W. Edom, V. P. Miller, W. A. LaMarr and N. Weng, *Anal. Chem.*, 2011, **83**, 8259–8266.
20. G. Madalinski, E. Godat, S. Alves, D. Lesage, E. Genin, P. Levi, J. Labarre, J.-C. Tabet, E. Ezan and C. Junot, *Anal. Chem.*, 2008, **80**, 3291–3303.
21. R. D. Smith, G. A. Anderson, M. S. Lipton, L. Pasa-Tolic, Y. F. Shen, T. P. Conrads, T. D. Veenstra and H. R. Udseth, *Proteomics*, 2002, **2**, 513–523.
22. H. Weissner, S. Nahnsen, J. Grossmann, L. Nilse, A. Quandt, H. Brauer, M. Sturm, E. Kenar, O. Kohlbacher, R. Aebersold and L. Malinstroemt, *J. Proteome Res.*, 2013, **12**, 1628–1644.
23. E. S. Baker, E. A. Livesay, D. J. Orton, R. J. Moore, W. F. Danielson, III, D. C. Prior, Y. M. Ibrahim, B. L. LaMarche, A. M. Mayampurath, A. A. Schepmoes, D. F. Hopkins, K. Tang, R. D. Smith and M. E. Belov, *J. Proteome Res.*, 2010, **9**, 997–1006.
24. H.-K. Min, S.-W. Hyung, J.-W. Shin, H.-S. Nam, S.-H. Ahn, H. J. Jung and S.-W. Lee, *Electrophoresis*, 2007, **28**, 1012–1021.
25. L. Pasa-Tolic, P. K. Jensen, G. A. Anderson, M. S. Lipton, K. K. Peden, S. Martinovic, N. Tolic, J. E. Bruce and R. D. Smith, *J. Am. Chem. Soc.*, 1999, **121**, 7949–7950.
26. N. Castle, D. Printzenhoff, S. Zellmer, B. Antonio, A. Wickenden and C. Silvia, *Comb. Chem. High Throughput Screening*, 2009, **12**, 107–122.
27. C. Farre, A. Haythornthwaite, C. Haarmann, S. Stoelzle, M. Kreir, M. George, A. Brueggemann and N. Fertig, *Comb. Chem. High Throughput Screening*, 2009, **12**, 24–37.
28. W. M. Tang, J. S. Kang, X. Y. Wu, D. Rampe, L. Wang, H. Shen, Z. Y. Li, D. Dunnington and T. Garyantes, *J. Biomol. Screening*, 2001, **6**, 325–331.
29. E. M. Chan, C. Xu, A. W. Mao, G. Han, J. S. Owen, B. E. Cohen and D. J. Milliron, *Nano Lett.*, 2010, **10**, 1874–1885.
30. D. Perera, J. W. Tucker, S. Brahmabhatt, C. J. Helal, A. Chong, W. Farrell, P. Richardson and N. W. Sach, *Science*, 2018, **359**, 429.
31. M. Wleklinski, B. P. Loren, C. R. Ferreira, Z. Jaman, L. Avramova, T. J. P. Sobreira, D. H. Thompson and R. G. Cooks, *Chem. Sci.*, 2018, **9**, 1647–1653.
32. S.-D. Huang, C. Shang, P.-L. Kang and Z.-P. Liu, *Chem. Sci.*, 2018, **9**, 8644–8655.
33. B. Maryasin, P. Marquetand and N. Maulide, *Angew. Chem., Int. Ed.*, 2018, **57**, 6978–6980.
34. S. Lotfi and J. Brgoch, *Comput. Mater. Sci.*, 2019, **158**, 124–129.

35. L. Wilbraham, R. S. Sprick, K. E. Jelfs and M. A. Zwijnenburg, *Chem. Sci.*, 2019, DOI: 10.1039/C8SC05710A.
36. M. Tsubaki and T. Mizoguchi, *J Phys Chem Lett*, 2018, **9**, 5733–5741.
37. J. Staker, K. Marshall, R. Abel and C. M. McQuaw, *J. Chem. Inf. Model.*, 2019, **59**, 1017–1029.
38. Y. Zhuo, A. Mansouri Tehrani and J. Brgoch, *J. Phys. Chem. Lett.*, 2018, **9**, 1668–1673.
39. C. W. Coley, W. Jin, L. Rogers, T. F. Jamison, T. S. Jaakkola, W. H. Green, R. Barzilay and K. F. Jensen, *Chem. Sci.*, 2019, **10**, 370–377.
40. L. Turcani, R. L. Greenaway and K. E. Jelfs, *Chem. Mater.*, 2018, **31**, 714–727.
41. J. M. Di Nicola, T. Bond, M. Bowers, L. Chang, M. Hermann, R. House, T. Lewis, K. Manes, G. Mennerat, B. MacGowan, R. Negres, B. Olejniczak, C. Orth, T. Parham, S. Rana, B. Raymond, M. Rever, S. Schrauth, M. Shaw, M. Spaeth, B. Van Wonterghem, W. Williams, C. Widmayer, S. Yang, P. Whitman and P. Wegner, *Nucl. Fusion*, 2019, **59**, 12.
42. C. Haynam, P. Wegner, J. Auerbach, M. Bowers, S. Dixit, G. Erbert, G. Heestand, M. Henesian, M. Hermann and K. Jancaitis, *Appl. opt.*, 2007, **46**, 3276–3303.
43. E. I. Moses and C. R. Wuest, *Fusion Sci. Technol.*, 2005, **47**, 314–322.
44. G. MacBeath and S. L. Schreiber, *Science*, 2000, **289**, 1760–1763.
45. E. Brouzes, M. Medkova, N. Savenelli, D. Marran, M. Twardowski, J. B. Hutchison, J. M. Rothberg, D. R. Link, N. Perrimon and M. L. Samuels, *Proc. Natl. Acad. Sci. U. S. A.*, 2009, **106**, 14195–14200.
46. D. C. Pregibon, M. Toner and P. S. Doyle, *Science*, 2007, **315**, 1393–1396.
47. J. G. Caporaso, C. L. Lauber, W. A. Walters, D. Berg-Lyons, J. Huntley, N. Fierer, S. M. Owens, J. Betley, L. Fraser, M. Bauer, N. Gormley, J. A. Gilbert, G. Smith and R. Knight, *Isme Journal*, 2012, **6**, 1621–1624.
48. M. M. Young, N. Tang, J. C. Hempel, C. M. Oshiro, E. W. Taylor, I. D. Kuntz, B. W. Gibson and G. Dollinger, *Proc. Natl. Acad. Sci. U. S. A.*, 2000, **97**, 5802–5806.
49. A. M. L. Liekens, J. De Knijf, W. Daelemans, B. Goethals, P. De Rijk and J. Del-Favero, *Genome Biol.*, 2011, **12**, 12.
50. R. D. King, K. E. Whelan, F. M. Jones, P. G. K. Reiser, C. H. Bryant, S. H. Muggleton, D. B. Kell and S. G. Oliver, *Nature*, 2004, **427**, 247–252.
51. R. Lorenz, R. P. Monti, I. R. Violante, C. Anagnostopoulos, A. A. Faisal, G. Montana and R. Leech, *arXiv preprint arXiv:1506.02088*, 2015.
52. S. J. Zhang, Z. T. Song, G. Godaliyadda, D. H. Ye, A. U. Chowdhury, A. Sengupta, G. T. Buzzard, C. A. Bouman and G. J. Simpson, *Anal. Chem.*, 2018, **90**, 4461–4469.
53. Y. Zhang, G. M. D. Godaliyadda, N. Ferrier, E. B. Gulsoy, C. A. Bouman and C. Phatak, *Ultramicroscopy*, 2018, **184**, 90–97.

## Autonomous Science: Big Data Tools for Small Data Problems in Chemistry

54. N. M. Scarborough, G. Godaliyadda, D. H. Ye, D. J. Kissick, S. J. Zhang, J. A. Newman, M. J. Sheedlo, A. U. Chowdhury, R. F. Fischetti, C. Das, G. T. Buzzard, C. A. Bouman and G. J. Simpson, *J. Synchrotron Radiat.*, 2017, **24**, 188–195.
55. P. Binev, W. Dahmen, R. DeVore, P. Lamby, D. Savu and R. Sharpley, in *Modeling Nanoscale Imaging in Electron Microscopy*, Springer, 2012, pp. 73–126.
56. J. Greenberg, K. Krishnamurthy and D. Brady, *Opt. Lett.*, 2014, **39**, 111–114.
57. A. C. Geiger, J. A. Newman, S. Sreehari, S. Z. Sullivan, C. A. Bouman and G. J. Simpson, in *High-Speed Biomedical Imaging and Spectroscopy: Toward Big Data Instrumentation and Management II*, International Society for Optics and Photonics, 2017, vol. 10076, p. 1007606.
58. S. Z. Sullivan, R. D. Muir, J. A. Newman, M. S. Carlsen, S. Sreehari, C. Doerge, N. J. Begue, R. M. Everly, C. A. Bouman and G. J. Simpson, *Opt. Express*, 2014, **22**, 24224–24234.
59. D. Garcia, *Comput. Stat. Data Anal.*, 2010, **54**, 1167–1178.
60. G. J. Wang, D. Garcia, Y. Liu, R. de Jeu and A. J. Dolman, *Environ. Modell. Softw.*, 2012, **30**, 139–142.
61. Z. Yu, J. B. Thibault, C. A. Bouman, K. D. Sauer and J. Hsieh, in *2008 15th IEEE International Conference on Image Processing*, IEEE, 2008, pp. 2600–2603.
62. G. Godaliyadda, D. H. Ye, M. D. Uchic, M. A. Groeber, G. T. Buzzard and C. A. Bouman, *Electron. Imaging*, 2016, **2016**, 1–8.
63. G. Godaliyadda, D. H. Ye, M. D. Uchic, M. A. Groeber, G. T. Buzzard and C. A. Bouman, *IEEE Trans. Comput. Imaging*, 2018, **4**, 1–16.
64. Y. Zhang, G. Godaliyadda, N. Ferrier, E. B. Gulsoy, C. A. Bouman and C. Phatak, *Electron. Imaging*, 2018, **2018**, 131–131-1316.
65. J. A. Nelder and R. Mead, *Comput. J.*, 1965, **7**, 308–313.
66. M. W. Routh, P. A. Swartz and M. B. Denton, *Anal. Chem.*, 1977, **49**, 1422–1428.
67. H. Winicov, J. Schainbaum, J. Buckley, G. Longino, J. Hill and C. E. Berkoff, *Anal. Chim. Acta*, 1978, **103**, 469–476.
68. G. E. Mielsing, R. W. Taylor, L. G. Hargis, J. English and H. L. Pardue, *Anal. Chem.*, 1976, **48**, 1686–1693.
69. K. Kong, C. J. Rowlands, H. Elsheikha and I. Notingher, *Analyst*, 2012, **137**, 4119–4122.
70. C. J. Rowlands, S. Varma, W. Perkins, I. Leach, H. Williams and I. Notingher, *J. Biophotonics*, 2012, **5**, 220–229.
71. C. Cortes and V. Vapnik, *Mach. Learn.*, 1995, **20**, 273–297.
72. C. R. Rao, *J. R. Stat. Soc. B*, 1948, **10**, 159–203.
73. R. D. King, J. Rowland, S. G. Oliver, M. Young, W. Aubrey, E. Byrne, M. Liakata, M. Markham, P. Pir and L. N. Soldatova, *Science*, 2009, **324**, 85–89.
74. K. E. Whelan and R. D. King, *Bmc Bioinformatics*, 2008, **9**, 16.
75. R. F. Murphy, *Nat. Chem. Biol.*, 2011, **7**, 327–330.

76. D. A. Cohn, Z. Ghahramani and M. I. Jordan, *J. Artif. Intell. Res.*, 1996, **4**, 129–145.
77. M.-F. Balcan, A. Beygelzimer and J. Langford, *J. Comput. Syst. Sci.*, 2009, **75**, 78–89.
78. M. Saar-Tsechansky and F. Provost, *Mach. Learn.*, 2004, **54**, 153–178.
79. A. W. Naik, J. D. Kangas, C. J. Langmead and R. F. Murphy, *PLoS One*, 2013, **8**, e83996.
80. A. W. Naik, J. D. Kangas, D. P. Sullivan and R. F. Murphy, *Elife*, 2016, **5**, e10047.
81. L. P. Coelho, A. Ahmed, A. Arnold, J. Kangas, A.-S. Sheikh, E. P. Xing, W. W. Cohen and R. F. Murphy, in *Linking Literature, Information, and Knowledge for Biology*, Springer, 2010, pp. 23–32.
82. L. P. Coelho, J. D. Kangas, A. W. Naik, E. Osuna-Highley, E. Glory-Afshar, M. Fuhrman, R. Simha, P. B. Berget, J. W. Jarvik and R. F. Murphy, *Bioinformatics*, 2013, **29**, 2343–2349.
83. M. V. Boland, M. K. Markey and R. F. Murphy, *Cytometry*, 1998, **33**, 366–375.
84. X. Chen and R. F. Murphy, *J. Biomed. Biotechnol.*, 2005, 87–95.
85. P. Nikolaev, D. Hooper, F. Webber, R. Rao, K. Decker, M. Krein, J. Poleski, R. Barto and B. Maruyama, *Npj Comput. Mater.*, 2016, **2**, 16031.
86. P. Nikolaev, D. Hooper, N. Perea-Lopez, M. Terrones and B. Maruyama, *Acs Nano*, 2014, **8**, 10214–10222.
87. R. Rao, N. Pierce, D. Liptak, D. Hooper, G. Sargent, S. L. Semiatin, S. Curtarolo, A. R. Harutyunyan and B. Maruyama, *Acs Nano*, 2013, **7**, 1100–1107.
88. A. Liaw and M. Wiener, *R News*, 2002, **2**, 18–22.
89. R. Diaz-Uriarte and S. A. de Andres, *BMC Bioinf.*, 2006, **7**, 13.
90. C. Strobl, A. L. Boulesteix, A. Zeileis and T. Hothorn, *BMC Bioinf.*, 2007, **8**, 21.
91. V. Svetnik, A. Liaw, C. Tong, J. C. Culberson, R. P. Sheridan and B. P. Feuston, *J. Chem. Inf. Comput. Sci.*, 2003, **43**, 1947–1958.
92. J. R. Quinlan, *Mach. Learn.*, 1986, **1**, 81–106.
93. J. R. Quinlan, *Int. J. Human-Comput. Stud.*, 1999, **51**, 497–510.
94. L. Màrquez and H. Rodríguez, in *European Conference on Machine Learning*, Springer, Berlin, Heidelberg, 1998, pp. 25–36.
95. L. M. Roch, F. Häse, C. Kreisbeck, T. Tamayo-Mendoza, L. P. Yunker, J. E. Hein and A. Aspuru-Guzik, *PLoS One*, 2020, **4**, e0229862.
96. L. M. Roch, F. Häse, C. Kreisbeck, T. Tamayo-Mendoza, L. P. E. Yunker, J. E. Hein and A. Aspuru-Guzik, *Sci. Robot.*, 2018, **3**, 2.
97. A. Madry, A. Makelov, L. Schmidt, D. Tsipras and A. Vladu, *arXiv preprint arXiv:1706.06083*, 2017.
98. A. Kurakin, I. Goodfellow and S. Bengio, *arXiv preprint arXiv:1611.01236*, 2016.
99. N. Papernot, P. McDaniel, I. Goodfellow, S. Jha, Z. B. Celik and A. Swami, 2017.

*Autonomous Science: Big Data Tools for Small Data Problems in Chemistry*

100. L. Huang, A. D. Joseph, B. Nelson, B. I. Rubinstein and J. D. Tygar, 2011.
101. B. Biggio and F. Roli, *Pattern Recognit.*, 2018, **84**, 317–331.
102. W. Y. Ma and S. Osher, *Inverse Problems and Imaging*, vol. 6, 2012, pp. 697–708.
103. E. H. Adelson, in *Human Vision and Electronic Imaging VI*, International Society for Optics and Photonics, 2001, vol. 4299, pp. 1–12.
104. V. Zantedeschi, M.-I. Nicolae and A. Rawat, presented in part at the Proceedings of the 10th ACM Workshop on Artificial Intelligence and Security, Dallas, Texas, USA, 2017.
105. N. Papernot, P. McDaniel and I. Goodfellow, *arXiv preprint arXiv:1605.07277*, 2016.
106. I. J. Goodfellow, J. Shlens and C. Szegedy, *arXiv preprint arXiv:1412.6572*, 2014.
107. C. Szegedy, W. Liu, Y. Jia, P. Sermanet, S. Reed, D. Anguelov, D. Erhan, V. Vanhoucke and A. Rabinovich, in *Proceedings of the IEEE Conference on Computer Vision and Pattern Recognition*, 2015, pp. 1–9.
108. K. a. E. Eykholt, Ivan and Fernandes, Earlence and Li, Bo and Rahmati, Amir and Xiao, Chaowei and Prakash, Atul and Kohno, Tadayoshi and Song, Dawn, *The IEEE Conference on Computer Vision and Pattern Recognition (CVPR)*, 2018, June.
109. I. Goodfellow, J. Pouget-Abadie, M. Mirza, B. Xu, D. Warde-Farley, S. Ozair, A. Courville and Y. Bengio, in *Advances in Neural Information Processing Systems*, 2014, pp. 2672–2680.